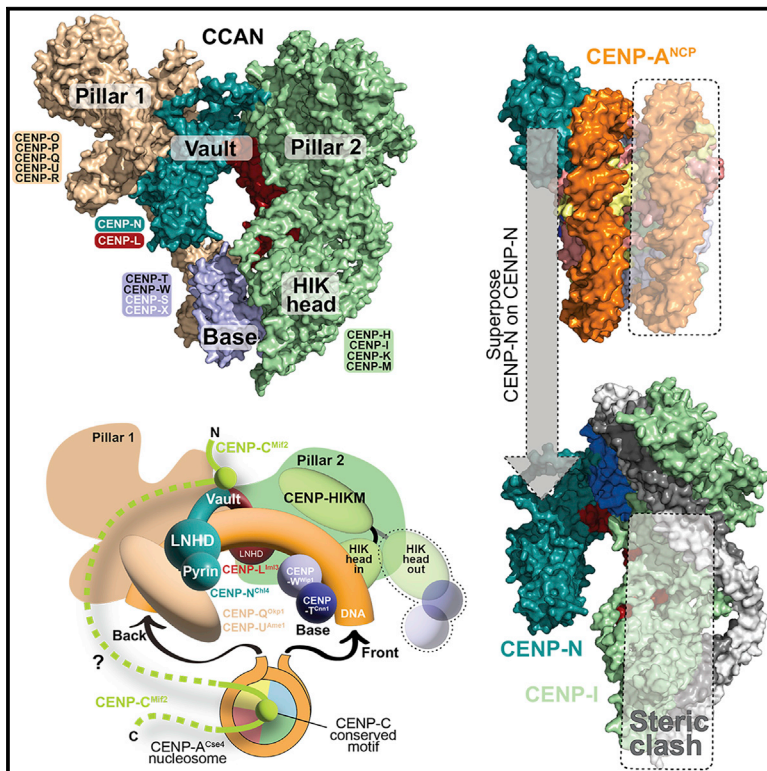


Molecular Cell

Structure of the human inner kinetochore CCAN complex and its significance for human centromere organization

Graphical abstract



Authors

Marion E. Pesenti, Tobias Raisch, Duccio Conti, ..., Ingrid R. Vetter, Stefan Raunser, Andrea Musacchio

Correspondence

ingrid.vetter@mpi-dortmund.mpg.de (I.R.V.),
stefan.raunser@mpi-dortmund.mpg.de (S.R.),
andrea.musacchio@mpi-dortmund.mpg.de (A.M.)

In brief

The centromere is a specialized chromosome locus that seeds the kinetochore, a macromolecular complex that promotes chromosome segregation. Pesenti, Raisch et al. report the structure of the constitutive centromere-associated network (CCAN), a multi-subunit assembly that surrounds CENP-A/CenH3, the centromere's epigenetic marker. The structure raises fundamental new questions on centromere organization.

Highlights

- A cryo-EM structure of the CCAN is reported
- The structure rationalizes relative positions and roles of the 16 CCAN subunits
- The CCAN core is shown to prefer naked DNA to CENP-A nucleosomes
- Several possible models of organization of centromeric chromatin are discussed



Article

Structure of the human inner kinetochore CCAN complex and its significance for human centromere organization

Marion E. Pesenti,^{1,4} Tobias Raisch,^{2,4} Duccio Conti,^{1,5} Kai Walstein,^{1,5} Ingrid Hoffmann,¹ Dorothee Vogt,¹ Daniel Prumbaum,² Ingrid R. Vetter,^{1,*} Stefan Raunser,^{2,*} and Andrea Musacchio^{1,3,6,*}

¹Department of Mechanistic Cell Biology, Max-Planck Institute of Molecular Physiology, Otto-Hahn-Straße 11, 44227 Dortmund, Germany

²Department of Structural Biochemistry, Max-Planck Institute of Molecular Physiology, Otto-Hahn-Straße 11, 44227 Dortmund, Germany

³Centre for Medical Biotechnology, Faculty of Biology, University Duisburg-Essen, Universitätsstrasse, 45141 Essen, Germany

⁴These authors contributed equally

⁵These authors contributed equally

⁶Lead contact

*Correspondence: ingrid.vetter@mpi-dortmund.mpg.de (I.R.V.), stefan.raunser@mpi-dortmund.mpg.de (S.R.), andrea.musacchio@mpi-dortmund.mpg.de (A.M.)

<https://doi.org/10.1016/j.molcel.2022.04.027>

SUMMARY

Centromeres are specialized chromosome loci that seed the kinetochore, a large protein complex that effects chromosome segregation. A 16-subunit complex, the constitutive centromere associated network (CCAN), connects between the specialized centromeric chromatin, marked by the histone H3 variant CENP-A, and the spindle-binding moiety of the kinetochore. Here, we report a cryo-electron microscopy structure of human CCAN. We highlight unique features such as the pseudo GTPase CENP-M and report how a crucial CENP-C motif binds the CENP-LN complex. The CCAN structure has implications for the mechanism of specific recognition of the CENP-A nucleosome. A model consistent with our structure depicts the CENP-C-bound nucleosome as connected to the CCAN through extended, flexible regions of CENP-C. An alternative model identifies both CENP-C and CENP-N as specificity determinants but requires CENP-N to bind CENP-A in a mode distinct from the classical nucleosome octamer.

INTRODUCTION

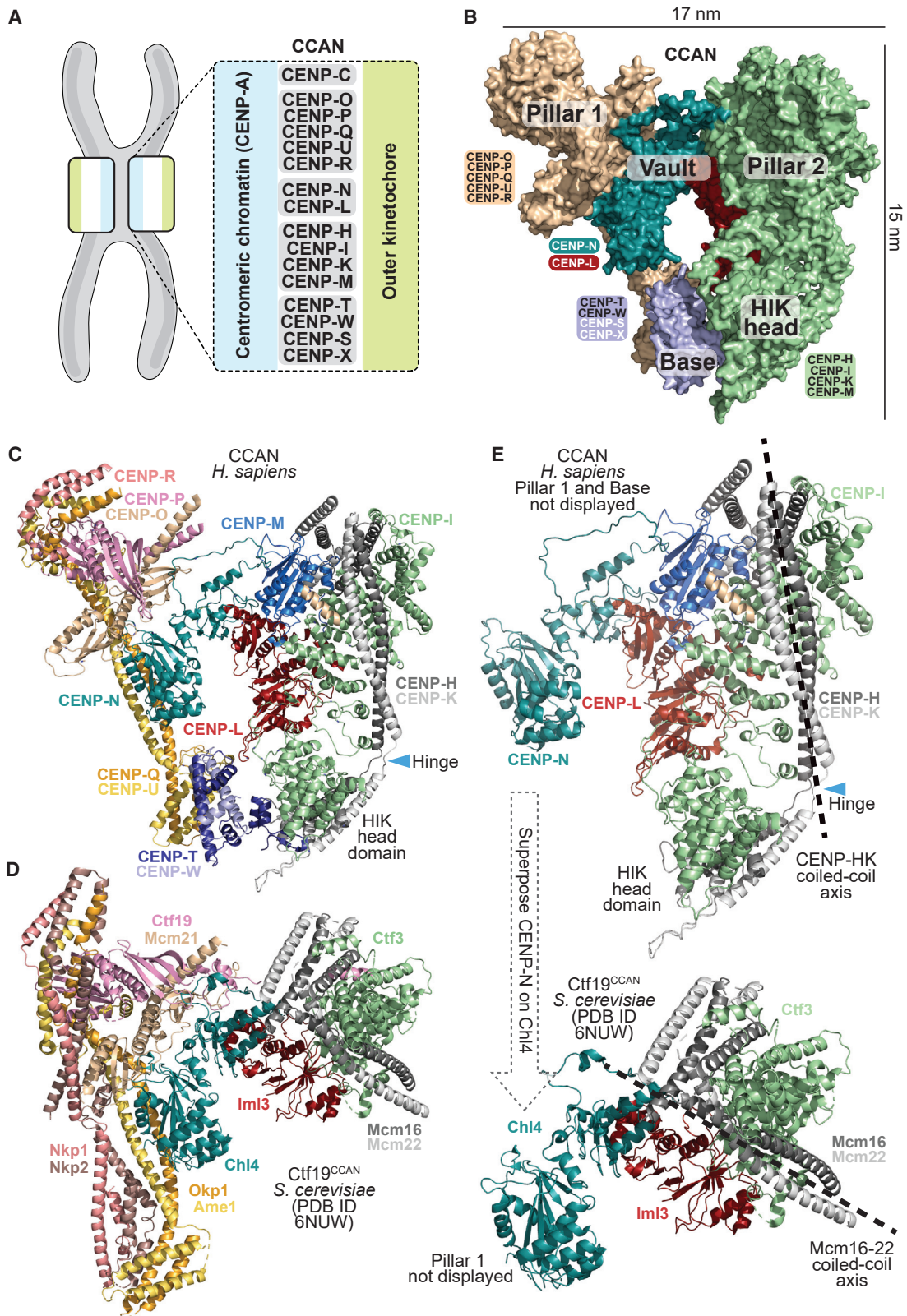
The distribution of chromosomes from a mother cell to its daughters is of paramount importance for the stability of intra- and inter-generational genetic inheritance. Essential for this process is a specialized protein complex, the “kinetochore,” which mediates the interaction of chromosomes and spindle microtubules. Kinetochores are complex macromolecular machines, consisting of approximately 30 core subunits, and are regulated at multiple levels to ensure errorless chromosome segregation (McKinley and Cheeseman, 2016; Musacchio and Desai, 2017).

Kinetochores assemble on a specialized chromosome segment, the centromere. The histone H3 variant centromeric protein A (CENP-A) is the hallmark of centromeres (McKinley and Cheeseman, 2016; Mellone and Fachinetti, 2021; Talbert and Henikoff, 2020). It seeds kinetochores by recruiting the 16-subunit constitutive centromere-associated network (CCAN) complex (Foltz et al., 2006; Izuta et al., 2006; Obuse et al., 2004; Okada et al., 2006) (Figure 1A). Two CCAN proteins, CENP-C and CENP-N, have emerged for specific recognition of CENP-A. CENP-C binds CENP-A nucleosomes through two

related motifs, the central region and the CENP-C motif. CENP-N recognizes the L1 loop of CENP-A (also referred to as Arg-Gly or RG loop), where the sequences of CENP-A and H3 diverge (Ali-Ahmad et al., 2019; Allu et al., 2019; Ariyoshi et al., 2021; Carroll et al., 2009, 2010; Chittori et al., 2018; Fang et al., 2015; Guo et al., 2017; Kato et al., 2013; Pentakota et al., 2017; Tian et al., 2018; Walstein et al., 2021).

The CCAN is the heart of the inner (centromere-proximal) kinetochore and plays several crucial functions in kinetochore assembly and centromere maintenance. First, it provides docking sites for the Knl1-Mis12-Ndc80 (KMN) network, a protein assembly of the outer (centromere-distal) kinetochore that mediates microtubule attachment and feedback control of the cell cycle (Musacchio and Desai, 2017). Second, it contributes to the inheritance of centromeres through cell division, which implies replenishment of CENP-A to compensate for its reduction during DNA replication (Jansen et al., 2007; Schuh et al., 2007). A basic organization comprising a CENP-A-based centromere and a CCAN-based inner kinetochore has undergone considerable evolutionary variation but remains recognizable in the vast majority of eukaryotes, including humans (Drinneberg and Akiyoshi, 2017; Tromer et al., 2019; van Hooff et al., 2017).





(legend on next page)

In *Saccharomyces cerevisiae* and related yeasts, centromeres are built on a conserved \sim 125-base-pair (bp) segment of DNA. These centromeres are limited to a single specialized nucleosome defined by the presence of Cse4^{CENP-A} and are thus defined as “point centromeres” (Bloom and Carbon, 1982; Fitzgerald-Hayes et al., 1982; Pluta et al., 1995). Most CCAN subunits are also identified in these organisms, where they are collectively referred to as the Ctf19 complex (henceforth Ctf19^{CCAN}). Recent high-resolution cryo-electron microscopy structures of the *S. cerevisiae*’s Ctf19^{CCAN} complex revealed the reciprocal organization of subunits and a possible mode of interaction with a Cse4^{CENP-A} nucleosome (Hinshaw and Harrison, 2019, 2020; Yan et al., 2019; Zhang et al., 2020).

Contrary to the point centromere of *S. cerevisiae*, most eukaryotes have regional centromeres that extend over tens of thousands to even millions of DNA bases. These more complex centromeres often feature repetitive DNA sequences, such as the AT-rich, \sim 171-bp α -satellite DNA repeats of human kinetochores (McKinley and Cheeseman, 2016; Musacchio and Desai, 2017; Talbert and Henikoff, 2020). Regional centromere assembly and inheritance, however, may be largely independent of DNA sequence. Rather, CENP-A and associated CCAN proteins promote the propagation of centromeres through the cell-cycle-regulated recruitment of specialized CENP-A loading machinery (Gambogi and Black, 2019; Mellone and Fachinetti, 2021).

The conservation of CCAN subunits suggests that regional centromeres are modular and assembled from the repetition of a basic point centromere “unit module” similar to Ctf19^{CCAN}. Reconstitution of a discrete human CCAN complex with purified components has provided strong support for this idea (McKinley et al., 2015; Pesenti et al., 2018; Walstein et al., 2021; Weir et al., 2016). Furthermore, negative-stain electron microscopy provided a first low-resolution reconstruction of human CCAN, revealing a structure reminiscent of that in *S. cerevisiae* and related yeasts (Hamilton et al., 2019; Kixmoeller et al., 2020; Pesenti et al., 2018).

Here, we report cryo-electron microscopy (cryo-EM) structures of human CCAN assemblies comprising 16 subunits, designated CENP-16, including the N-terminal region of CENP-C residues 1–544 (CENP-C^{1–544}) and the subcomplexes CENP-O/CENP-P/CENP-Q/CENP-U/CENP-R (CENP-OPQR complex), CENP-N/CENP-L (CENP-LN), CENP-H/CENP-I/CENP-K/CENP-M (CENP-HIKM), and CENP-T/CENP-W/CENP-S/CENP-X (CENP-TWSX). We show that the human CCAN structure, although similar to the yeast Ctf19^{CCAN} structure in its outline, diverges from it in crucial aspects that have important implications for nucleosome binding. Furthermore, we report that previous structures of the CENP-N N-terminal region bound to an octameric CENP-A nucleosome (Allu et al., 2019; Chittori et al.,

2018; Pentakota et al., 2017; Tian et al., 2018) seem incompatible with the environment of CENP-N in human CCAN. We discuss various models of centromere organization that might reconcile these observations.

RESULTS

An overview of CCAN

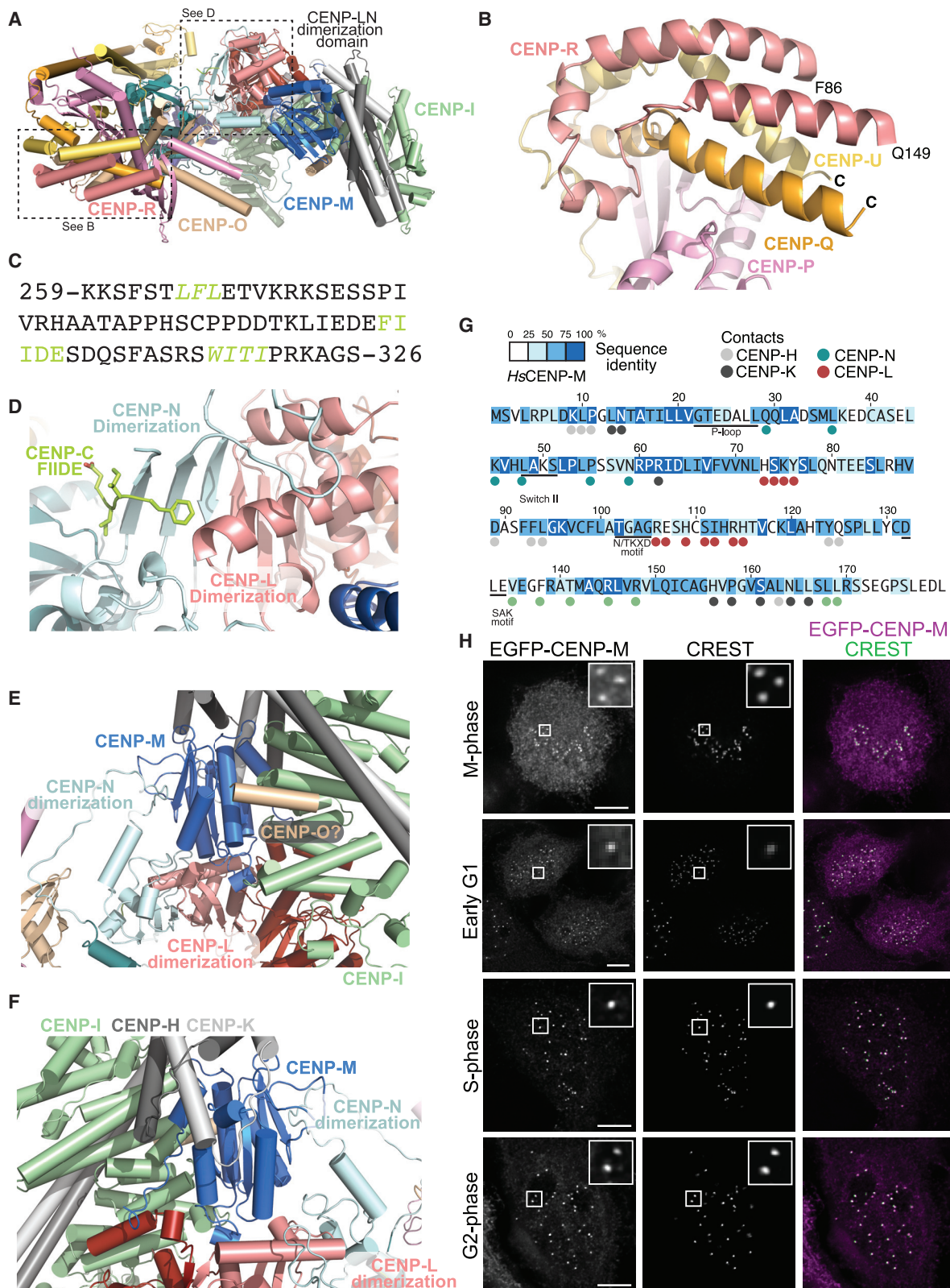
We generated CENP-16 from stable individual subcomplexes in preparation for cryo-EM data collection (Figures S1 and S2). Two datasets, including one of pure CENP-16 (dataset I) and one of CENP-14 (lacking CENP-SX) with 145-bp DNA and CENP-A:H4 (dataset II), were processed independently (Figures S3 and S4; see also Table S1 and STAR Methods). We obtained reconstructions for both datasets, but only dataset I yielded a resolution range (3.7 Å in the center with lower resolution in peripheral regions) compatible with reliable model building (Figures S3–S5).

Molecular models of CCAN subunits were either available from previous structural work (CENP-M, CENP-N), or were generated by homology modeling based on structures of yeast CCAN (Hinshaw and Harrison, 2019, 2020; Yan et al., 2019; Zhang et al., 2020), and in later phases by AlphaFold2 in the variants ColabFold and AlphaFold-Multimer (Evans et al., 2021; Jumper et al., 2021; Mirdita et al., 2021). Structure-based alignments of yeast and human CCAN^{Ctf19} subunits are in Figures S6–S9. Models were fitted in the density using a combination of manual and automated fitting (see STAR Methods). The final model of CENP-16 has a molecular mass of \sim 450 kDa and consists of \sim 25,000 atoms, encompassing 14 of the 16 subunits. CENP-S and CENP-X (CENP-SX), which require CENP-TW for incorporation into CENP-16 (Figures S1E and S1F), were not modeled as we could not identify a density for these subunits, suggesting they are disordered or absent from the particles.

CENP-16 can be rationalized as consisting of two “pillars” connected by a “vault” and a “base” (Figure 1B). Pillars 1 and 2 consist of CENP-OPQR and CENP-HIKM, respectively. The vault consists of CENP-LN. The base consists of CENP-TW, whose position is more clearly defined in the lower-resolution map from dataset II, possibly a stabilizing effect from presence of DNA and/or CENP-A:H4 in the sample (neither of which, however, had clearly recognizable density). Despite their overall similarity (Figures 1C and 1D), human and yeast CCAN^{Ctf19} differ significantly due to two distinct and large rigid-body rotations (Figures S10A–S10E) (Vevers and Hayward, 2019). The first rotation describes the degree of opening of the vault, whose curvature is higher in the human complex (deep, closed vault) relative to yeast (shallow, open vault) (Figures S10C–S10D). The second rotation is roughly parallel to the axis of the long CENP-HK coiled-coil and describes the relative

Figure 1. General organization of human CCAN

- (A) Scheme of kinetochore organization with CCAN subcomplexes.
 (B) Surface model of CENP-16 complex colored to identify distinct sub-modules discussed in the text.
 (C) Cartoon model of human CCAN with differently colored chains.
 (D) Cartoon model of the *S. cerevisiae* Ctf19^{CCAN} with same coloring scheme as for human subunits, as applicable (Hinshaw and Harrison, 2019; Yan et al., 2019).
 (E) Cartoon models of human CCAN and yeast Ctf19^{CCAN} were superposed through CENP-N^{Ch4}, and the resulting orientation of pillar 2 (CENP-HIKM) was compared. Pillar 2 adopts different orientations in human and yeast CCAN^{Ctf19}; more divergent in yeast and more parallel to pillar 1 (CENP-OPQR) in humans. Pillar 1 and the base were removed to enhance clarity. See Figure S10 for further details on structural differences of human CCAN and yeast Ctf19^{CCAN}.



(legend on next page)

orientation of CENP-L and pillar 2 (Figure S10E). It causes the angle between pillar 1 and pillar 2 to be much wider in the yeast structure than in the human structure (Figure 1E and Figures S10F and S10G). These structural differences have important implications, as discussed below.

Map resolution is highest where the vault interacts with pillars 1 and 2 and decreases in more peripheral regions (Figures S3 and S4). Nevertheless, there is significant density, especially in maps from dataset II, for the complex of the CENP-I N-terminal domain with the CENP-HK C-terminal domain, which together form a “HIK head domain” connected to the rest of pillar 2 by a short hinge (Figure 1C). The HIK head domain associates with the histone-fold domains (HFDs) of CENP-T and CENP-W (the “base”). These were modeled with AF2 and also with reference to crystal structures of the Cnn1^{CENP-T}-Wap1^{CENP-W} complex bound to the *S. cerevisiae* HIK head (PDB: 6WUC and 6YPC) (Hinshaw and Harrison, 2020; Zhang et al., 2020) (Figure 1C).

CENP-R, CENP-C, and CENP-M

CENP-R caps the “northern” globular head of pillar 1 (Figures 1C and 2A). Density is limited to a CENP-R region comprising residues Phe86-Gln149 (as assigned by AF2), consisting of two α helices and a short helical connector (Figure 2B). The rest of the structure is predicted intrinsically disordered. The CENP-R helices pack against a short pair of helices at the C terminus of the CENP-QU subcomplex. Their position is roughly equivalent to that of α helices of Nkp1 and Nkp2 in the related structure of the *S. cerevisiae* Ctf19^{CCAN} complex (Hinshaw and Harrison, 2019; Yan et al., 2019) (Figure 1D), possibly suggesting a distant evolutionary relationship. However, Nkp1 and Nkp2 accompany the entire length of pillar 1 in Ctf19^{CCAN}, tightly interacting with Okp1^{CENP-U} and Ame1^{CENP-O}, whereas CENP-R does not extend beyond the head of pillar 1. As a result, pillar 1 is thinner in human CCAN (Figures 1C and 1D).

Most of the 943-residue protein CENP-C is predicted intrinsically disordered. Previous work rationalized CENP-C as a blueprint for kinetochore assembly, with an N- to C-terminal succession of binding motifs aligned along the outer to inner kinetochore axis (Klare et al., 2015; Walstein et al., 2021). These begin at the N terminus with an interaction motif for the outer-kinetochore MIS12 complex (Gascoigne et al., 2011; Screpanti et al., 2011), followed by motifs for the CCAN subunits CENP-LN and CENP-HIKM (comprised between residues 259 and 326 and highlighted in green in Figure 2C) (Klare et al., 2015; Pentakota et al., 2017), and further down for the CENP-A nucleo-

some. In humans, two related CENP-A binding motifs are found, the central region (residues 515–535) and the CENP-C motif (735–755) (Ariyoshi et al., 2021; Guo et al., 2017; Kato et al., 2013; Walstein et al., 2021). Finally, CENP-C dimerizes through its only sizable folded region, the C-terminal cupin domain (Chik et al., 2019; Cohen et al., 2008; Medina-Pritchard et al., 2020; Walstein et al., 2021).

CENP-C^{1–544} is part of CENP-16, but there is no discernible CENP-C density except for a Phe-Ile-Ile-Asp-Glu (303-FIIDE-307) fragment. This fragment binds near the CENP-LN dimerization domain (Figure 2D) and has previously been shown to promote CENP-LN recruitment to human kinetochores (Nagpal et al., 2015; Pentakota et al., 2017). Supported by AF2 predictions, we also tentatively assigned a predicted single α helix at the N terminus of CENP-O to an unaccounted density at the interface of CENP-HK, CENP-I, and CENP-M (Figure 2E and Figure S5E).

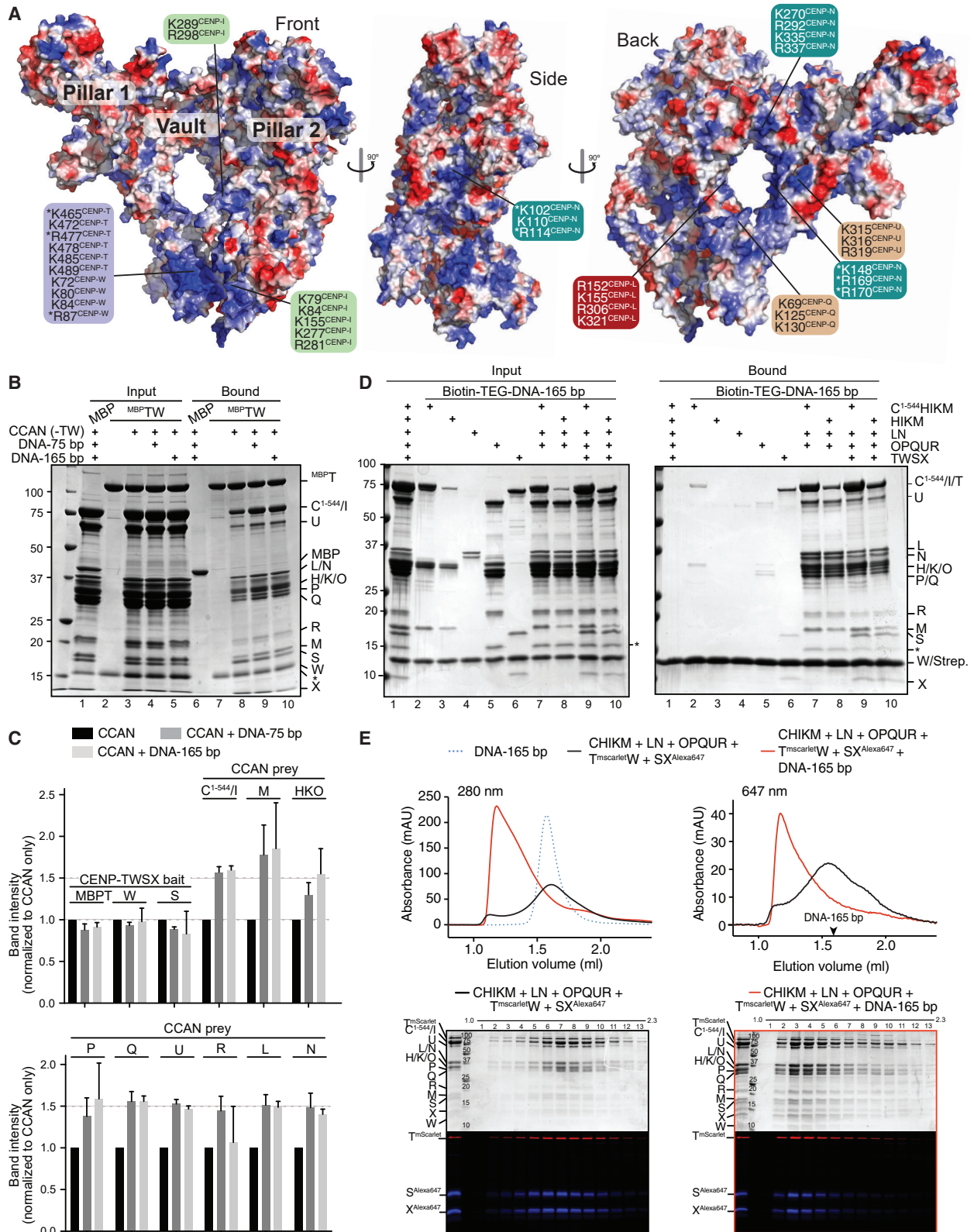
The pseudo GTPase CENP-M, unable to bind and hydrolyze GTP (Basilico et al., 2014), binds near the CENP-LN dimerization domains at the vault’s apex (Figure 1C). Using conserved interfaces, CENP-M also wedges against CENP-I and CENP-HK, generating a robust network of interactions that bury collectively more than 3,300 Å² (Figures 2E–2G and Figure S10F). As CENP-M resides at kinetochores throughout the cell cycle (Figure 2H and Figure S11), its stabilizing function may be constitutive and unregulated. In summary, pillar 2 is considerably better connected to the CENP-LN vault in human CCAN than in yeast Ctf19^{CCAN}, where the Ctf3^{CENP-I}-Mcm16^{CENP-H}-Mcm22^{CENP-K} trimer connects to Ctf19^{CCAN} exclusively through a small interface (~550 Å²) between Ctf3^{CENP-I} and Iml3^{CENP-L} (Figure S10F).

CENP-16 binds DNA

The CENP-TW base and CENP-LN vault domains surround a central tunnel further extended by pillar 2 on the front and pillar 1 on the back of CCAN (Figure 1B). Lined with several positively charged residues from CENP-L and CENP-N, and with an internal diameter of ~27 Å, the vault seems ideally suited to surround the negatively charged backbone of a double-stranded (ds) DNA filament (diameter of ~20 Å). CENP-TW in the CCAN base also expose the DNA-binding interface of the HFDs, which flank positive patches on CENP-I in the HIK head domain in the front (Figure 3A, left) and on CENP-QU in the back (Figure 3A, right). Another positive patch on CENP-N’s $\alpha 6$ helix, including K102, K110, and R114 (Figure 3A, middle), has been recently implicated in CENP-A nucleosome stacking by the CENP-N N-terminal domain (Zhou et al., 2021).

Figure 2. CENP-C, CENP-M, and CENP-R

- Cartoon of human CCAN viewed from above (relative to Figure 1C), with the “knob” domain of pillar 1, the dimerization domain of the CENP-LN vault, and the upper domain of pillar 2 with CENP-M.
- Close-up view of the two helices of CENP-R, with visible residues and connecting helical segment.
- Sequence of HsCENP-C within the CCAN-binding region. Two sequences (green and italics) identify motifs shown to interact with CENP-LN and CENP-HIKM (Klare et al., 2015). The FIIDE motif interacts with the CENP-LN dimerization domain.
- Cartoon model of the CENP-LN dimerization domain with bound CENP-C FIIDE motif in sticks. See Figure S5F for corresponding density.
- Embedding of CENP-M in a network of interactions between pillar 2 and the vault.
- A rotated view showing additional CENP-M interactions.
- Sequence of CENP-M with conservation in 12 distant CENP-M orthologs and contacts with neighboring subunits (adapted from Basilico et al., 2014). CENP-M residues contacting other CCAN subunits are identified with the color of the interacting subunit.
- Localization of EGFP-CENP-M in HeLa cells during the cell cycle demonstrates continuity of localization. With the exception of the early G1 condition, the displayed cells are also displayed in Figure S11. Scale bars, 5 μ m.



(legend on next page)

To gather evidence for DNA binding by CENP-16, we immobilized a maltose-binding protein (MBP)-CENP-T fusion protein complexed with CENP-W and monitored binding of the remaining CCAN subunits in the absence or presence of 75-bp DNA (to ensure extensive coverage of the predicted DNA-binding interface, which we estimate may form contiguous contacts for at least 65–70 bp of DNA) or 165-bp DNA (a length compatible with speculative higher-order organization of CCAN, such as dimerization). Both DNAs caused an ~ 1.5 -fold increase of all CCAN preys on the ^{MBP}CENP-TW bait (Figures 3B and 3C). Next, we immobilized a 165-bp DNA-biotin conjugate on streptavidin beads and assessed binding by individual CCAN substructures or their combination (Figure 3D). In isolation, CENP-TW and CENP-C^{1–544}HIKM showed strong and moderate DNA binding, respectively, whereas CENP-HIKM, CENP-LN, and CENP-OPQUR showed minimal or negligible DNA binding (Figure 3D, lanes 2–6). Strong DNA binding was instead observed with various combinations of these species, indicating that DNA binding requires simultaneous interactions of the various CCAN subcomplexes. Importantly, the CENP-11 complex (CENP-HIKM, CENP-LN, and CENP-OPQUR), consisting of the vault and surrounding pillars, bound DNA tightly even without CENP-C^{1–544} or CENP-TW (Figure 3D, lane 8).

In size-exclusion chromatography (SEC), where the elution volume is inversely related to a macromolecule's size and elongation, CENP-TW bound DNA strongly (Figure S12A). CENP-C^{1–544}HIKM and CENP-OPQUR bound DNA, but weakly (Figures S12B and S12C), whereas neither CENP-LN nor CENP-HIKM co-eluted with DNA (Figures S12D and S12E). Our previous report of DNA binding by CENP-HIKM in an electrophoretic mobility shift assay (EMSA) (Weir et al., 2016) may reflect the low ionic strength of EMSA in comparison with 300 mM NaCl in our SEC assays. Both CENP-12 (CENP-LN, CENP-C^{1–544}HIKM, and CENP-OPQUR) and CENP-16 (CENP-LN, CENP-C^{1–544}HIKM, CENP-OPQUR, and CENP-TWSX) demonstrated strong DNA binding (Figure S12F and Figure 3E, respectively), as revealed by a reduced elution volume and a sharper elution profile. These results collectively agree with the solid-phase assays and with previous studies (Carroll et al., 2009, 2010; Nishino et al., 2012; Takeuchi et al., 2014; Weir et al., 2016).

Nucleosome binding by human CCAN

CENP-L and CENP-N are paralogs that share a ~ 130 -residue CENP-LN homology domain (LNHD) and that interact through a distinct C-terminal dimerization domain (Hinshaw and Harri-

son, 2013; Pentakota et al., 2017) (Figure 4A). Previous structures of a CENP-A nucleosome in complex with an N-terminal construct of CENP-N (approximately residues 1–210 of CENP-N; PDB: 6C0W) demonstrated extensive interactions of CENP-N^{LNHD} with the nucleosome's DNA and no major contacts with the nucleosome core (Figure 4B, top two panels) (Allu et al., 2019; Chittori et al., 2018; Pentakota et al., 2017; Tian et al., 2018). Conversely, an 80-residue CENP-N pyrin domain preceding the CENP-N^{LNHD} recognizes the exposed CENP-A L1 loop (Allu et al., 2019; Chittori et al., 2018; Pentakota et al., 2017; Tian et al., 2018) (Figures 4A and 4B), whose divergence from H3 has been implicated in epigenetic centromere inheritance (Black et al., 2004, 2007). Validating the interaction, mutation of CENP-N residues involved in L1 loop recognition prevented CENP-N kinetochore recruitment (Carroll et al., 2009; Chittori et al., 2018; Pentakota et al., 2017).

As we have seen, CENP-N^{LNHD} and CENP-L^{LNHD}, which lean rigidly against pillars 1 and 2, respectively (Figure 1C), form a clamp in a deep vault that seems ideally suited to surround a single dsDNA filament rather than two adjacent filaments as in a nucleosome. Thus, the CENP-A nucleosome-binding mode of the CENP-N N-terminal region (pyrin domain and LNHD; Figure 4B) is unlikely to predict how CCAN binds CENP-A nucleosomes. Indeed, superposition of the CENP-N N-terminal regions in CCAN and in the CENP-N:CENP-A nucleosome complex (6COW) predicts a dramatic steric clash of the nucleosome's second DNA gyre (i.e., the one distal from CENP-N) and of the underlying histone core with CENP-L and with the HIK head of CCAN (Figure 4B, bottom panel). Thus, CENP-N in human CCAN may be unable to bind CENP-A through the same mechanism demonstrated by structures obtained with the sole CENP-N N-terminal region (Allu et al., 2019; Chittori et al., 2018; Pentakota et al., 2017; Tian et al., 2018). For this to happen, a single turn of DNA, instead of two adjacent turns, would have to be presented to CCAN. Indeed, a single dsDNA filament is predicted to fit snugly into the deep, closed CENP-LN vault (Figure S13A). Whether this binding mode could be accompanied by CENP-A binding by CENP-N is discussed below.

Alternative nucleosome-binding modes

A recent structure of an *S. cerevisiae* Ctf19^{CCAN} subcomplex (with composition equivalent to that of human CENP-11) bound to a classical octameric Cse4^{CENP-A} nucleosome (PDB: 6QLD; Figure 5A and Figure S13B) (Yan et al., 2019) suggested an

Figure 3. Human CCAN binds DNA

(A) Surface electrostatics (red, negative; blue, positive; potential display levels were between -80 and 80 kT/e) on human CCAN complex. Positively charged residues contributing to potential DNA-binding interfaces are indicated. Asterisks mark residues previously shown to affect DNA binding (Chittori et al., 2018; Nishino et al., 2012; Takeuchi et al., 2014; Zhou et al., 2021).

(B) Left: Binding assay on amylose beads with MBP (negative control) and ^{MBP}CENP-TW as baits. CCAN subunits were added in solution, with or without DNA. Beads were recovered by centrifugation, washed, and analyzed by SDS-PAGE. The asterisk here and in other panels with SDS-PAGE gels marks a proteolytic product of CENP-R (probably its folded core).

(C) Quantified band intensities of indicated subunits or group of subunits (when co-migrating) normalized to their intensity in the absence of DNA. The quantification reflects three technical replicates. Error bars indicate SD.

(D) Biotin-TEG (triethyleneglycol) DNA (165 bp) immobilized on streptavidin beads was incubated with the indicated CCAN subcomplexes. Inputs and bound proteins were visualized by SDS-PAGE and Coomassie staining.

(E) Size-exclusion chromatography of the indicated complexes with or without 165-bp dsDNA. Proteins separated by SDS-PAGE were visualized with Coomassie (top) or fluorescence (bottom). Profiles report absorbance at the indicated wavelengths.

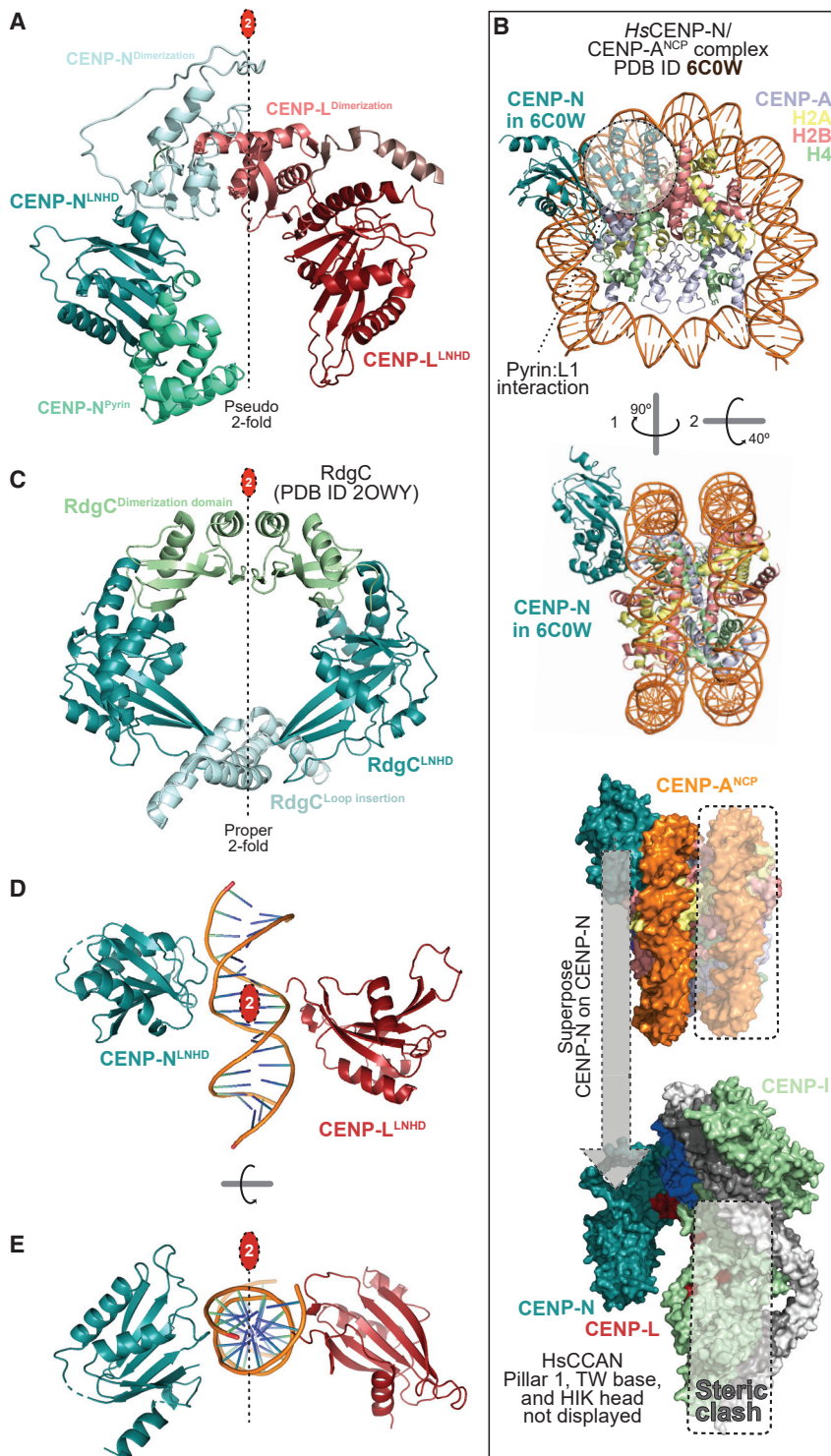


Figure 4. Properties of the CENP-LN vault

(A) The isolated CENP-LN vault with highlighted CENP-N pyrin domain (~80 residues, greencyan), CENP-N LNHD (LN homology domain), dimerization domains of CENP-N and CENP-L, and CENP-L LNHD. A 2-fold pseudosymmetry axis (interrupted line with red oval) relates the LNHDs.

(B) Top: Rotated cartoon model of the CENP-N-terminal region bound to a CENP-A nucleosome (PDB: 6C0W) in two orthogonal orientations (Pentakota et al., 2017). The pyrin domain binds the L1 loop of CENP-A (light blue) and the LNHD to DNA. H2A C-terminal tails were removed for clarity. Bottom: Superposition of CENP-N in 6C0W to CENP-N in human CCAN predicts a steric clash of the second DNA gyre (boxed) onto pillar 2. The vault can only accept one gyre of DNA.

(C) Cartoon model of the RdgC homodimer highlighting the LNHDs and other structural elements. (D) The LNHDs of CENP-LN displayed in absence of other domains (dimerization, pyrin) and modeled with 15-bp DNA from the 6C0W structure (B) positioned identically relative to CENP-N. The 2-fold pseudosymmetry axis between LNHDs coincides with the 2-fold pseudosymmetry axis of DNA. (E) A 90°-rotated view of the same object.

making essentially no contacts with Im13^{CENP-L} or more generally with pillar 2 (Figures 5C and 5D and Figures S13C and S13D). The position of Chl4^{CENP-N} and of CENP-N relative to the nucleosome core in the structures of the yeast Ctf19^{CCAN}:Cse4^{CENP-A} nucleosome complex (PDB: 6QLD) and of the human CENP-N:CENP-A nucleosome complex (PDB: 6C0W) are therefore entirely unrelated, to the point that in the yeast structure Chl4^{CENP-N} does not face the L1 loop of Cse4^{CENP-A}, contrary to the human CENP-N:CENP-A nucleosome structure, where CENP-N directly faces the L1 loop (Figure 5B). In fact, there are almost no visible contacts between Ctf19^{CCAN} and the core of the Cse4^{CENP-A} nucleosome in the 6QLD structure, with the exception of the interaction involving an intrinsically disordered segment of (otherwise largely invisible) Mif2^{CENP-C} (Yan et al., 2019).

To assess whether the Ctf19^{CCAN}:Cse4^{CENP-A} nucleosome complex (6QLD) is a plausible model for a human CCAN-nucleosome complex, we superposed Chl4^{CENP-N} in 6QLD with CENP-N in our structure of human CENP-16 and evaluated the fit of the 6QLD nucleosome on human CCAN. The superposition predicted a dramatic clash of the modeled nucleosome with the HIK head of human CCAN (Figure 5D, bottom) and a less dramatic overlap of the

alternative binding mode in which Chl4^{CENP-N} interacts with a loose end of dsDNA unwrapped from the core of the Cse4^{CENP-A} nucleosome, rather than with the Cse4^{CENP-A} L1 loop (Figures S13C and S13D). The unwrapped DNA docks in the Chl4^{CENP-N}-Im13^{CENP-L} vault, leaning against Chl4 and

H2A:H2B dimer with CENP-L. In principle, the major clash could be resolved if the HIK head swung out of its observed position through rotation about the hinge (blue arrowhead, Figures 1C and 1E and Figures 5C and 5D, bottom), ending in a position similar to that of yeast Ctf19^{CCAN}, where the HIK head undergoes a $\sim 90^\circ$ rotation upon binding to the Cse4^{CENP-A} nucleosome (Yan et al., 2019). However, this would result in fundamentally different complexes due to the different orientation of pillar 2 relative to pillar 1 and CENP-N in the yeast and human complexes (Figure 1E and Figures S10E–S10G). In the Ctf19^{CCAN}:Cse4^{CENP-A} complex (6QLD), pillar 2 does not contact the Cse4^{CENP-A} nucleosome (Figures 5C and 5E), whereas after hinge rotation, pillar 2 in the predicted human complex would make multiple contacts with the nucleosome (Figures 5E and 5F).

If human CENP-A nucleosomes and CENP-11 interacted as predicted by this binding mode, CENP-A nucleosomes should compete with DNA binding in the vault (which is tight; Figure 3C). Contrary to this expectation, CENP-A nucleosomes competed the binding of CENP-11 to immobilized DNA much more weakly than free DNA (Figures 5G and 5H and Figure S13E). Thus, CENP-11 seems incapable of high-affinity binding to CENP-A nucleosomes. We also conclude that the structure of the Ctf19^{CCAN}:Cse4^{CENP-A} nucleosome complex (6QLD), even after considering possible conformational changes of the human complex, is unlikely to predict the interaction of human CCAN with CENP-A.

Open and closed vaults in point and regional centromeres

A consequence of the large-scale rotations described in Figures S10A–S10D is that the CENP-LN vault is deep (closed) in human CCAN and rather shallow (open) in yeast CCAN^{Ctf19} (Figure S10C). The closed vault of human CCAN seems ideally suited to embrace DNA, and CENP-L and CENP-N are related to the bacterial protein RdgC, a DNA-binding homodimer that forms a full, closed circle for DNA binding (Ha et al., 2007; Tromer et al., 2019) (Figure 4C). The distant relationship with RdgC seems to imply that CENP-LN originated from the duplication of a DNA-binding homodimeric singleton (Tromer et al., 2019). Further supporting this, the CENP-L^{LNHD} and CENP-N^{LNHD} in CENP-16 are related by 2-fold pseudosymmetry (Figures 4D and 4E). With DNA from the proximal gyre of the CENP-N:CENP-A nucleosome complex modeled in the vault after superposition of CENP-N, the DNA's own 2-fold pseudosymmetry axis aligns with the 2-fold pseudosymmetry axis of the LNHDs of

CENP-L and CENP-N (Figures 4D and 4E). Due to the shallower vault, this alignment is broken in the yeast Ctf19^{CCAN}:Cse4^{CENP-A} nucleosome complex (PDB: 6QLD; Figure S13F), even with DNA in the vault (Yan et al., 2019).

AF2 predicted closed vaults in essentially every organism we tested except for a small group of budding yeasts related to *S. cerevisiae* (Figures S14A and S14B). Even close relatives of these yeasts were predicted to have closed vaults instead. Because *S. cerevisiae*'s Ctf19^{CCAN} contains the only experimentally determined structure of a CENP-LN vault in the Protein Data Bank, prediction by AF2 of closed vaults in humans and most other organisms is unlikely to reflect a bias from existing structures and, rather, likely reflects intrinsic sequence features, although so far we have been unable to identify obvious predictive hallmarks besides the general sequence identities. We also note that a closed vault does not correlate with presence of CENP-M, as the latter cannot be identified in organisms, such as *Saccharomyces pombe* or *N. crassa* (Navarro-Mendoza et al., 2019; Tromer et al., 2019), where CENP-LN are predicted by our AF2 analyses to form a closed vault. Future work will have to address whether the presence of open or closed vaults correlates with fundamental features of centromeres, such as being point or regional, a possibility our analysis hints to.

CENP-C promotes CENP-A nucleosome binding

As already mentioned, the central region and conserved motif of CENP-C bind specifically to CENP-A nucleosomes. We asked therefore if CENP-C^{1–544}, when added to DNA-immobilized CENP-11 or CENP-15 (CENP-11 with CENP-TWSX), promoted binding of CENP-A nucleosomes (built with 145- or 199-bp DNA). Indeed, addition of CENP-C^{1–544} to either sample (to generate CENP-12 or CENP-16) resulted in robust CENP-A nucleosome binding (Figure 5I and Figure S13G, compare lanes 6 and 7 to lanes 8 and 9).

Thus, collectively, our observations indicate that CENP-C establishes the only robust connection of CCAN with an octameric CENP-A nucleosome. In addition to this link, CCAN may be additionally interacting with CENP-A through CENP-N, but in this case CENP-A must be embedded in a chromatin structure distinct from an octameric nucleosome, as the latter does not show significant binding affinity to CENP-11, a complex that contains CENP-N and that binds robustly to dsDNA.

Centromere stability of CCAN depends on CENP-A

We reasoned that if CENP-C established the only connection between CCAN and CENP-A, its depletion would be expected to

(C) Top: Rotated view of the yeast complex (6QLD) already shown in (A). Pillar 1 was removed for clarity. Chl4^{CENP-N} was used to superpose Ctf19^{CCAN} on human CCAN (bottom, pillar 1 and the base were also removed for clarity, only vault and pillar 2 are shown). The HIK head domain is boxed (dashed line).

(D) Objects in (C) are shown as surfaces. Superposition of CENP-N^{Chl4} predicts a dramatic steric clash of the nucleosome with the HIK head domain.

(E) 6QLD is displayed as in (C) but rotated approximately 180° . There are no contacts of pillar 2 with the Cse4 nucleosome core.

(F) Human CCAN (same orientation to the yeast complex in E) was modeled onto 6QLD by aligning CENP-N on Chl4^{CENP-N}. The predicted steric clash of HIK head with the Cse4^{CENP-A} nucleosome (demonstrated in D) can be solved by a swinging-out rotation about the hinge. There are residual predicted clashes of CENP-L with H2A:H2B. Effects of the different relative position of pillar 2 relative to CENP-N^{Chl4} in yeast and human are evident.

(G) CENP-11 was first immobilized by allowing its binding to biotinylated DNA on streptavidin beads. Free DNA or CENP-A nucleosomes at 1× or 3× ratio to protein were then added as indicated. Beads were washed and analyzed by SDS-PAGE.

(H) Three technical replicates of the experiment in (G) were quantified.

(I) The indicated CCAN species were immobilized on streptavidin beads coated with biotinylated DNA. Presence of CENP-C^{1–544} distinguished the CENP-11 and CENP-12 complexes. Retention of 145- or 199-bp CENP-A nucleosomes was only observed in presence of CENP-C. Three technical repeats were performed.

cause dissociation of CCAN subunits from the centromere at a rate comparable to that occurring after co-depletion of CENP-C and CENP-A. Conversely, if CENP-A contributed to additional interactions with CCAN subunits, dissociation of the CCAN subunits might be expected to be faster if CENP-A was removed in addition to CENP-C. CENP-C and CENP-A tagged endogenously with genetically encoded fluorescent proteins and an inducible degron (Fachinetti et al., 2015; Hoffmann et al., 2020) were rapidly depleted by addition of auxin. When only CENP-C was depleted, CENP-A was robustly retained at centromeres (Figure 6A–6C and Figure S15). Conversely, CENP-A disappeared rapidly when its destruction was induced together with that of CENP-C. Importantly, we observed significantly more rapid dissociation kinetics of CENP-HK and CENP-T when CENP-C and CENP-A were depleted simultaneously than when only CENP-C was depleted (kinetics of CENP-LN and CENP-OPQUR dissociation could not be examined due to lack of suitable antibodies). Although we cannot exclude that the depletion of CENP-A causes additional changes in centromeric chromatin that affect dissociation of CCAN subunits only indirectly, these initial experiments imply that CENP-A contributes to the retention of CCAN subunits even after depletion of CENP-C, suggesting that interactions of CCAN with CENP-A may not be limited to CENP-C.

DISCUSSION

The structure of human CCAN is a milestone in the study of centromeric chromatin. It builds on early proteomic studies that identified most vertebrate CCAN subunits (Foltz et al., 2006; Izuta et al., 2006; Obuse et al., 2004; Okada et al., 2006) and on subsequent biochemical reconstitutions and structural analyses (Ali-Ahmad et al., 2019; Allu et al., 2019; Ariyoshi et al., 2021; Carroll et al., 2009, 2010; Guo et al., 2017; Kato et al., 2013; McKinley et al., 2015; Nishino et al., 2012; Pentakota et al., 2017; Pesenti et al., 2018; Walstein et al., 2021; Weir et al., 2016; Xiao et al., 2017). The structure demonstrates the overall organization of human CCAN, with insights on unique subunits, including CENP-M and CENP-R, and insightful differences with the *S. cerevisiae* complex. Our results support the concept that regional centromeres are assembled from the repetition of an individual structural module that the point centromere of *S. cerevisiae* exemplifies (Hinshaw and Harrison, 2019, 2020; Yan et al., 2019; Zhang et al., 2020).

Figure 7 presents various models for the interaction of human and yeast CCAN^{Ctf19} with CENP-A^{Cse4}. The essence of the models in Figure 7A is that CCAN binds linker DNA and that CENP-C establishes the only specific contacts with CENP-A, with the latter embedded in canonical octameric nucleosomes (possibly in a dinucleosome [Walstein et al., 2021]). The linker DNA occupies the vault of CCAN, entering from the front (like in the yeast Ctf19^{CCAN}:Cse4^{CENP-A} nucleosome structure; PDB: 6QLD) (Yan et al., 2019) or from the back, as in the complex of human CCAN with a CENP-A nucleosome (Yatskevich et al., 2022). As discussed in the results, a CENP-A nucleosome entering from the front and positioned like the Cse4^{CENP-A} nucleosome in 6QLD (Yan et al., 2019) is an unsatisfactory model for human CCAN. CENP-11 shows a clear preference for DNA rela-

tive to nucleosomes. Our structure and recently published structures of human CCAN with DNA in the vault (Yatskevich et al., 2022) demonstrate a “swung-in” conformation of the HIK head-TW complex, where CENP-TW stabilizes the dsDNA filament as the “base,” joining the vault to fully encircle the DNA. With a nucleosome positioned as in 6QLD, this conformation predicts a dramatic steric clash.

While perplexing, differences in the relative positions of the nucleosome and CCAN in the Ctf19^{CCAN}:Cse4^{CENP-A} nucleosome complex (PDB: 6QLD) and in the recently described complex of human CCAN with a CENP-A nucleosome (Yan et al., 2019; Yatskevich et al., 2022) may simply indicate that the intrinsic disorder of CENP-C^{Mif2} allows substantial flexibility and conformational freedom in the way CCAN^{Ctf19} and the CENP-A^{Cse4} nucleosome connect (Figure 7A). In both models, sequence-related motifs of CENP-C (the “central region,” not present in all CENP-C orthologs, and the “conserved motif”) bind the acidic patch of H2A:H2B and the Cse4^{CENP-A} C-terminal tail (Ariyoshi et al., 2021; Kato et al., 2013; Yan et al., 2019). CENP-C^{Mif2} further interacts with CCAN^{Ctf19} subunits, including CENP-L^{Imi3}:CENP-N^{Chl4} and CENP-H^{Mcm16}:Ctf3^K:Mcm22^M, with motifs that may not be fully conserved (Hinshaw and Harrison, 2013; Hornung et al., 2014; Klare et al., 2015; McKinley et al., 2015; Nagpal et al., 2015; Pentakota et al., 2017). For example, the 303-FIIDE-307 CENP-C motif, shown to be instrumental for the recruitment of CENP-LN to the kinetochore (Pentakota et al., 2017), is not recognizable in Mif2^{CENP-C}.

The models in Figure 7A imply that CENP-C is the only generator of specificity in the interaction of CCAN^{Ctf19} with CENP-A^{Cse4}. Indeed, CENP-C is essential for kinetochore assembly and viability. In line with extensive previous evidence, we show here that CENP-C is necessary for an interaction of CCAN with the CENP-A nucleosome. These observations, however, do not exclude the existence of other direct contacts between CCAN and CENP-A. Our CENP-A/CENP-C co-depletion experiments in Figure 6 suggest that such contacts might exist. Depletion of CENP-C has been shown to be compatible with short-term retention of very significant levels of CCAN subunits in DT40 cells (Hori et al., 2008). Furthermore, CENP-C displays slow but significant turnover at interphase kinetochores in DT40 chicken cells, contrary to CCAN subunits CENP-H and CENP-T, which are essentially immobile (Watanabe et al., 2022). Thus, CCAN may depend on CENP-A for its localization in addition to CENP-C, and previous work points to CENP-N as a plausible mediator of these additional interactions (Carroll et al., 2009, 2010). Within the CENP-N N-terminal region, the pyrin domain binds the CENP-A L1 loop *in vitro*, and mutations at this interface, including mutations of CENP-N^{Glu3}, CENP-N^{Glu7}, and CENP-N^{Arg11}, ablate CENP-A binding *in vitro* and CENP-N localization *in vivo* (Allu et al., 2019; Carroll et al., 2009, 2010; Chittori et al., 2018; Pentakota et al., 2017; Tian et al., 2018). The structure of the yeast Ctf19^{CCAN}:Cse4^{CENP-A} nucleosome complex did not confirm Chl4^{CENP-N} as L1 loop decoder, but, as we have seen, this structure is an unlikely model for human CCAN.

What requirements should be met for the CENP-N pyrin domain to recognize the L1 loop? Two crucial conditions emerge. First, CENP-A:H4 ought to be presented to CENP-LN

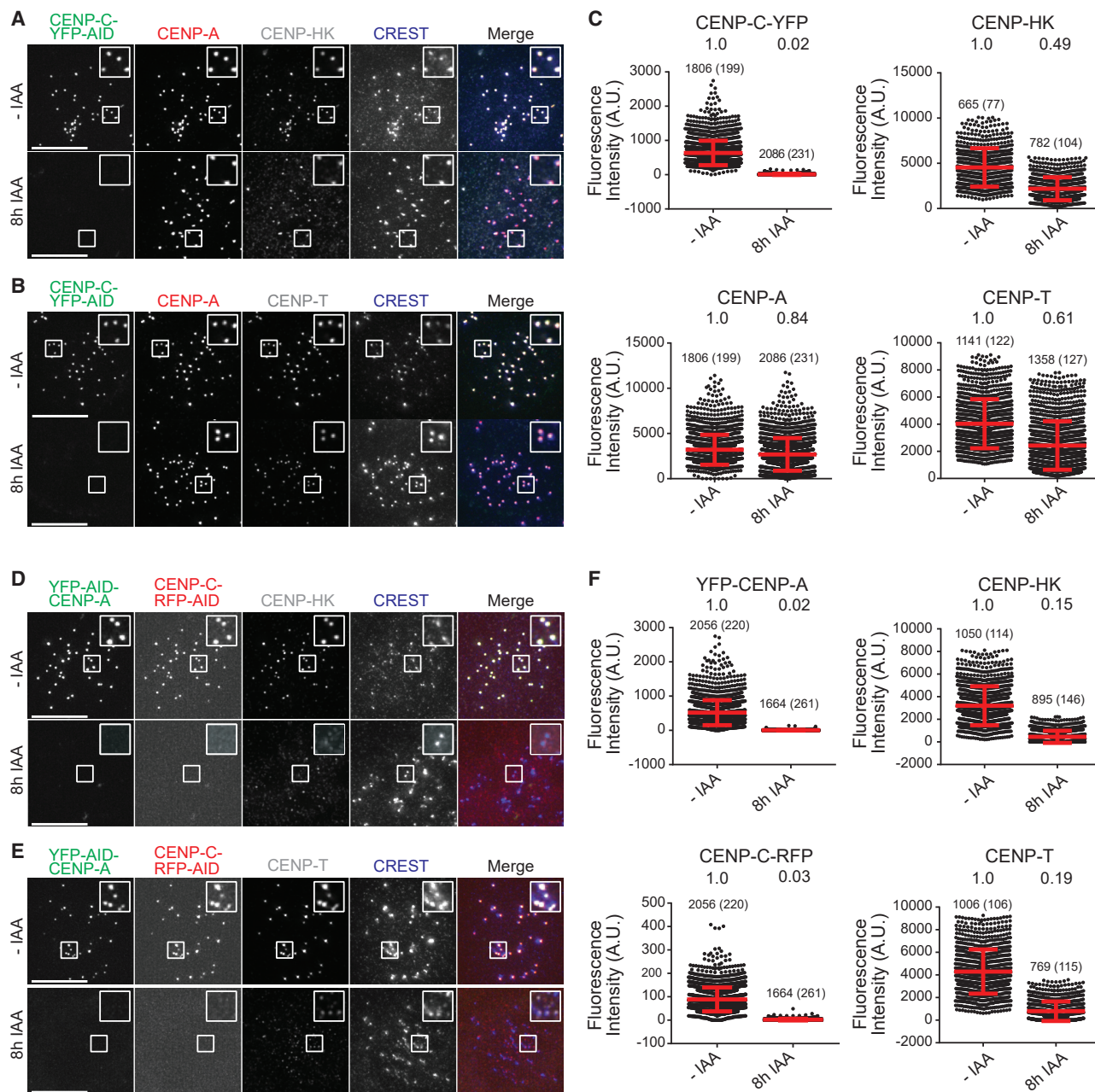


Figure 6. Comparison of CCAN disassembly rates

(A) Degradation of CENP-C endogenously tagged with a EYFP-AID cassette (Fachinetti et al., 2015) was induced by addition of indole acetic acid (IAA, auxin). A complete time course is shown in Figure S15. Shown here is the 8-h time point. Levels of CENP-A, CENP-HK, and CREST were also monitored. Scale bar, 10 μ m.

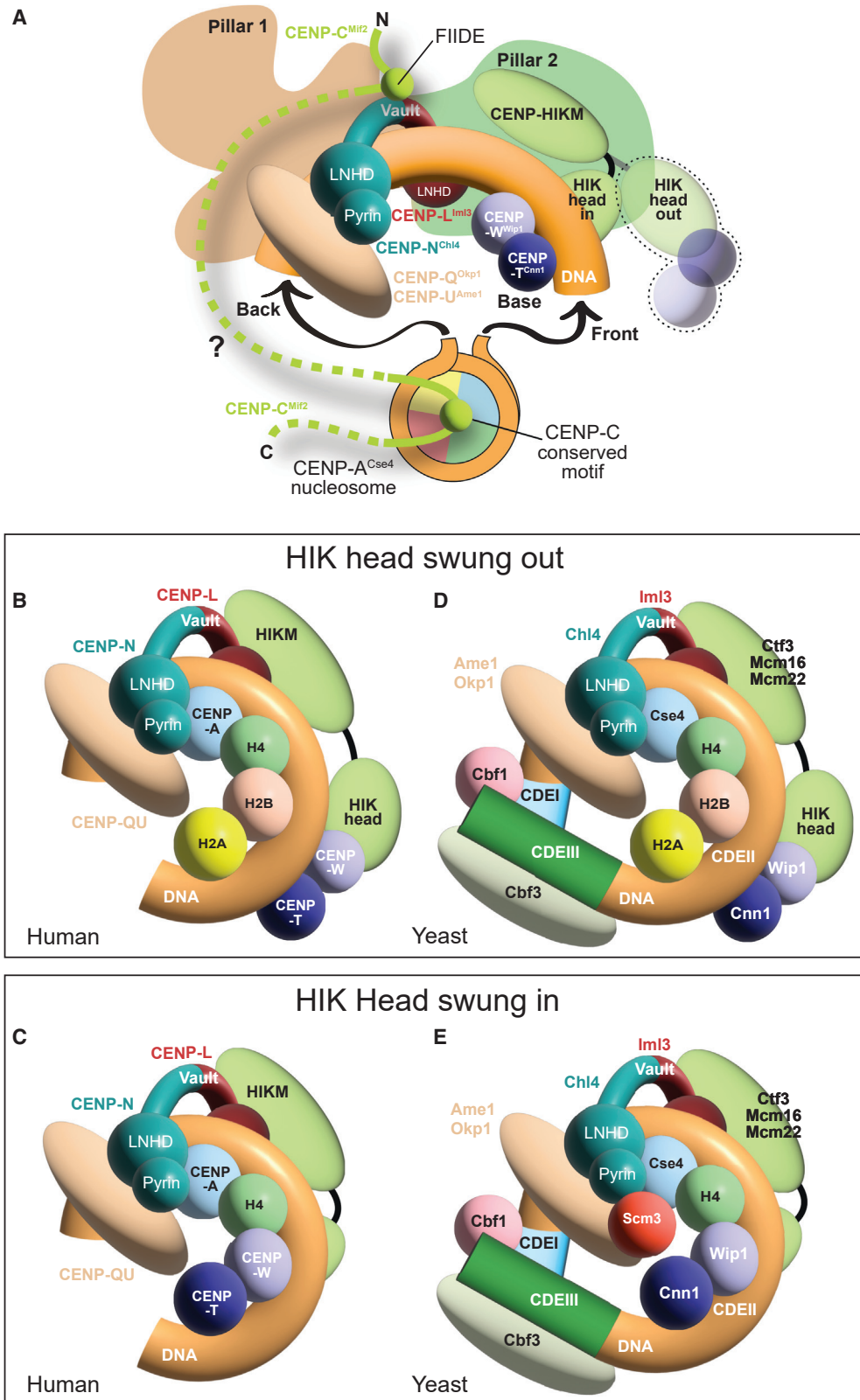
(B) As in (A), but with levels of CENP-T monitored instead of CENP-HK. Scale bar, 10 μ m.

(C) Quantification of the experiments in (A) and (B). Residual levels (expressed as fractions of control), number of kinetochores, and number of cells (in parentheses) are indicated. Levels of CENP-A and CENP-C^{YFP-AID} from both experiments were quantified. Levels of CENP-T and CENP-HK were quantified from the individual experiments in (A) and (B). Red bars represent average fluorescence intensities and SD of quantified centromere foci from two technical repeats.

(D) Degradation of CENP-A endogenously tagged with a EYFP-AID cassette and of CENP-C endogenously tagged with an RFP-AID cassette (Hoffmann et al., 2020) at the 8-h time point after addition of IAA (see Figure S15). Levels of CENP-HK and CREST were also monitored. Scale bar, 10 μ m.

(E) As in (D), but with levels of CENP-T monitored. Scale bar, 10 μ m.

(F) Quantification of the experiments in (D) and (E) was performed and displayed precisely as described for (C).



(legend on next page)

in a structure different from a classical nucleosome with 2 gyres of DNA, as only the CENP-N-proximal filament of dsDNA, with an associated CENP-A:H4, would be allowed in the CENP-LN vault without major steric clashes. Second, homodimerization of CENP-A would likely have to be prevented (Black et al., 2004; Tachiwana et al., 2011) to avoid a predicted steric clash with the CENP-QU N-terminal domain, contiguous to the CCAN base at the back of the CENP-LN tunnel. A structure that satisfies these two conditions is the so-called hemisome, a half-nucleosome sequence of histones with the order CENP-A:H4:H2B:H2A (Figure 7B). Hemisome models for centromeric chromatin have been invoked before (summarized in Black and Cleveland, 2011; Dunleavy et al., 2013; Talbert and Henikoff, 2020) but remain speculative. CENP-A assembles into stable octameric mononucleosomes *in vitro* and has been isolated in octamers also from nuclease-treated chromatin (Hasson et al., 2013; Nechemia-Arbely et al., 2017; Tachiwana et al., 2011). However, native centromeres may disassemble when chromatin is trimmed to mononucleosomes (Ando et al., 2002), raising the question of whether a handful of CENP-A embedded in a different chromatin structure, possibly collectively larger than a mononucleosome, might have been neglected.

Exposing CCAN^{Ctf19} to a pre-assembled, stable octameric CENP-A nucleosome, possibly with additional DNA extruding from the core, will with some likelihood promote assembly of complexes like those in Figure 7A (Yan et al., 2019; Yatskevich et al., 2022). Although sufficiently stable for structural analysis, these structures will also need to be evaluated for their physiological relevance. The same approach would not be helpful toward testing speculative hemisome models, as the stabilization of non-canonical and classical nucleosomes is expected to involve different mechanisms. Two crucial stabilizing factors of octameric nucleosomes are the dimerization of CENP-A (or H3) and the stabilization of the left-handed helical staircase of histone octamers by the H2A C-terminal docking domain (Eickbush et al., 1988; Shukla et al., 2011). Neither would be present in the hemisome structure postulated in Figure 7B. Furthermore, in CCAN, H2A:H2B could be part of the hemisome only if the HIK head and CENP-TW base adopted a swung-out conformation. In the swung-in conformation (this study; Yatskevich et al., 2022), H2A:H2B would have to be replaced with CENP-TW to

avoid a dramatic steric clash (Figure 7C). The C-terminal extension of CENP-T is buried at the interface with HIK (this study; Hinshaw and Harrison, 2020; Zhang et al., 2020) and could not possibly contribute to nucleosome stabilization.

Thus, alternative nucleosome structures may have much-reduced stability compared to octameric nucleosomes. *Ad hoc* procedures for their incorporation in, and stabilization by, CCAN may be necessary for successful reconstitution. Enzymes overcoming kinetic barriers large enough to slow down spontaneous assembly may be required. Be that as it may, our attempts at reconstituting a CCAN:chromatin structure with DNA, CENP-TW (with or without H2A:H2B), and CENP-A:H4 bound to the CENP-LN vault were hitherto unsuccessful (unpublished data). Furthermore, we find that at least the hemisome model in Figure 7C is not supported by predictions of AF2 and related programs (unpublished data). Thus, we cannot yet claim own experimental evidence supporting models like those in Figures 7B and 7C.

In *S. cerevisiae*, Cse4^{CENP-A} resides on a central DNA core of 78–86 bp named CDEII (Camahort et al., 2009; Cole et al., 2011; Furuyama and Biggins, 2007; Henikoff et al., 2014; Keith and Fitzgerald-Hayes, 2000; Krassovsky et al., 2012; Meluh et al., 1998). Flanking CDEII, two additional regions of 8 and ~25 bp, known respectively as CDEI and CDEIII, bind the additional factors Cbf1 and Cbf3 complex. Research into how the Ctf19^{CCAN} complex binds the centromeric DNA of *S. cerevisiae* should take into account these fundamental specificities, but work so far has only addressed a complex with an octameric nucleosome on a 147-bp Widom 601 DNA sequence (PDB: 6QLD) (Yan et al., 2019). Due to the small size of CDEII, a centromeric nucleosome with two full turns seems unlikely. An alternative hypothesis is that the nucleosome core of *S. cerevisiae* is an octamer, as possibly implied by fluorescence counts of Cse4^{CENP-A} (Wisniewski et al., 2014), but surrounded by a single turn of DNA. Yet another alternative is the Cse4^{CENP-A}:H4:H2B:H2A hemisome (Figure 7D) (Dalal et al., 2007; Furuyama et al., 2013; Henikoff et al., 2014; Talbert and Henikoff, 2020). It remains conjectural but was shown to neatly explain the pattern of H4 S47C-anchored cleavage mapping at *S. cerevisiae* centromeres (Henikoff et al., 2014). The hemisome model in Figure 7D is closely reminiscent of the speculative

Figure 7. Models of centromere:chromatin interaction

(A) Common features of the CCAN^{Ctf19}:CENP-A^{Cse4} interaction in yeast and humans. The CENP-L^{Imi3N^{Chl4}} vault is occupied by dsDNA that emerges from a CENP-A^{Cse4} nucleosome that is otherwise not directly integrated in CCAN^{Ctf19} and only connected to it through CENP-C^{Mif2}, which acts as the crucial link between the nucleosome and the CCAN^{Ctf19}. CENP-C^{Mif2} is flexible (dotted line), enabling multiple binding modes observed or predicted in yeast and humans. The conserved motif (and presumably the central region if present) binds the CENP-A^{Cse4} nucleosome. The FIIDE motif is only detected in human CENP-C, but an equivalent region of Mif2^{CENP-C} binds to Imi3^{CENP-L}:Chl4^{CENP-N} in *S. cerevisiae* (Hinshaw and Harrison, 2013). In the “swung-in” conformation, the HIK head positions the attached CENP-T^{Cnn1W^{Vip1}} in the observed “base” position (this conformation would not be available to the yeast complex due to the divergence of pillar 2). A putative “swung-out” conformation is also shown.

(B) In this model CENP-A:H4 faces the pyrin domain of CENP-N. A single filament of dsDNA is allowed inside the CENP-LN vault. The CENP-TW base connected to the HIK head is in a swung-out conformation that permits an interaction of CENP-A:H4 with H2A:H2B, with which CENP-TW would otherwise clash. CENP-QU may contribute, alone or in complex with other proteins, to prevent CENP-A dimerization, generating a hemisome.

(C) The same hemisome complex, but with H2A:H2B replaced by CENP-TW as expected for the swung-in conformation observed in our structures.

(D) The CDEII core of the yeast point centromere is ~85 bp long, and Cse4^{CENP-A} is precisely positioned on it (Cole et al., 2011; Furuyama and Biggins, 2007). The CDEII core is flanked by CDEI and CDEIII motifs that associate with Cbf1 and Cbf3. A hemisome model has been proposed for this organism (see main text). As shown, the wrap of the DNA in the model is left-handed, but there is evidence for right-handedness (Diaz-Ingelmo et al., 2015; Furuyama and Henikoff, 2009; Huang et al., 2011).

(E) Another hemisome model may explain depletion of H2A:H2B at yeast centromeres as well as a function of Scm3 in preventing Cse4^{CENP-A} dimerization. This swung-in conformation of the HIK arm would require a large-scale conformational change of pillar 2, making it resemble the human complex.

model of human CCAN discussed in Figure 7B, which we developed to satisfy the requirement that CENP-N decodes the L1 loop of CENP-A.

Further complicating the picture, histone H2A and H2B are depleted from centromeres both in *S. cerevisiae* and *S. pombe* (Mizuguchi et al., 2007; Rossi et al., 2021; Williams et al., 2009; Xiao et al., 2011), opposing observations notwithstanding (Krasovskiy et al., 2012; Pinto and Winston, 2000; Westermann et al., 2003). At yeast centromeres, depletion of H2A:H2B had been discussed in the context of evidence supporting the existence of a hexasome of Cse4^{CENP-A}:H4 with Scm3. Scm3 is a Cse4 chaperone and a stable centromere resident at all cell-cycle stages in *S. cerevisiae* (Mizuguchi et al., 2007; Xiao et al., 2011). Subsequent structural work indicated that Scm3 binds the Cse4^{CENP-A} dimerization interface and competes with dimerization (Cho and Harrison, 2011; Dechassa et al., 2011), questioning the hexasome model, which assumed the dimerization of Cse4^{CENP-A}:H4 in a tetrasome. A speculative alternative explanation is that Scm3, in addition to depositing Cse4^{CENP-A}, stably suppresses Cse4^{CENP-A} dimerization, an expected and potentially beneficial function if the basic structure of yeast centromeres were a hemisome. How could the depletion of H2A:H2B be accounted for, however? Our speculative model in Figure 7C, where H2A:H2B are replaced with CENP-TW, may serve as inspiration to answer this question. H2A:H2B may be replaced with Cnn1^{CENP-T}:Wip1^{CENP-W} in a hypothetical “swung-in” conformation of the yeast complex similar to that observed in humans (Figure 7E). We predict, however, that this would require a more complex restructuring of pillar 2 in yeast toward the conformation of human CCAN.

The two classes of models for centromeric chromatin we have discussed are not incompatible. The class in Figure 7A is supported by current experimental evidence and proposes that a regular octameric CENP-A^{Cse4} nucleosome flanks CCAN and interacts with it through CENP-C^{Mif2} (Hinshaw and Harrison, 2013; Klare et al., 2015; McKinley et al., 2015; Nagpal et al., 2015; Walstein et al., 2021). The second class (exemplified by Figures 7B–7E) predicts that linker DNA emanating from the neighboring CENP-A^{Cse4} nucleosome enters a CCAN particle where CENP-N^{Chl4} decodes the L1 loop of CENP-A^{Cse4}. If this configuration exists, the CENP-A chromatin interacting with CCAN cannot be in the form of a regular octameric nucleosome. Reconstitution of this chromatin may be considerably more challenging in view of different, and currently unknown, stabilization requirements. Future work will have to address systematically the implications and value of these models *in vitro* and *in vivo*, testing them with a combination of biochemical reconstitution, structural analysis, and mutational validation.

Limitations of the study

The medium resolution of our CCAN maps limits accuracy of molecular models, but we regard this as a minor limitation, as we focus on implications of the CCAN architecture that are well supported by the structure at this resolution. The main limitation is that we examined different models of CENP-A recognition by CCAN but did not provide conclusive evidence for any of them. We present *in vivo* evidence that the interactions of CCAN and CENP-A are not limited to CENP-C. These additional interactions

are unlikely to involve an octameric CENP-A nucleosome, but until now we have been unable to reconstitute the alternative binding modes we discuss or others that we might have not considered.

STAR★METHODS

Detailed methods are provided in the online version of this paper and include the following:

- KEY RESOURCES TABLE
- RESOURCE AVAILABILITY
 - Lead Contact
 - Materials availability
 - Data and code availability
- EXPERIMENTAL MODEL AND SUBJECT DETAILS
 - Cell lines and culture
 - Bacterial and insect cell lines
 - Plasmids and cloning
- METHOD DETAILS
 - Generation of biotinylated DNA
 - Protein expression and purification
 - Fluorescence labeling of recombinant proteins
 - Analytical SEC
 - Pull-down assays
 - *In vitro* assembly of CCAN
 - Sample preparation for electron microscopy
 - Negative stain electron microscopy
 - Cryo-EM grid preparation and data acquisition
 - Cryo-EM data processing
 - Model building and structure refinement
 - Cell culture and immunofluorescence
- QUANTIFICATION AND STATISTICAL ANALYSIS
 - Quantification of centromere signals
 - Quantification of SDS-PAGEs

SUPPLEMENTAL INFORMATION

Supplemental information can be found online at <https://doi.org/10.1016/j.molcel.2022.04.027>.

ACKNOWLEDGMENTS

We are grateful to Oliver Hofnagel for help with data collection, to Julia Schweighofer and Sabine Wohlgenuth for help with production of CENP-LN and CENP-TW, and to Stephen C. Harrison, Karolin Luger, Keda Zhou, and the Musacchio and Raunser laboratories for helpful discussions and sharing unpublished results. We are especially indebted to Don Cleveland and Daniele Fachinetti for sharing degron-tagged cell lines. This work was supported by the Max Planck Society (to A.M. and S.R.). D.C. acknowledges funding by the European Molecular Biology Organization (EMBO) through an EMBO Long-Term Fellowship (ALTF 439–2019). A.M. acknowledges funding by the Marie-Curie Training Network DiVIDE (project number 675737) and by the European Research Council (ERC) through Synergy Grant 951430 (BIOMECHANET) and Advanced Grant 669686 (RECIPIANCE).

AUTHOR CONTRIBUTIONS

Conceptualization: A.M.; Investigation: M.E.P. (sample preparation, biochemistry, *in vitro* experiments), D.P., T.R., I.R.V. (data collection and processing), I.R.V. (structure determination and model building), D.C., K.W. (cell biology assays); Funding acquisition: A.M., S.R.; Project Administration: A.M., S.R.;

Resources: I.H., D.V.; Supervision: A.M., S.R., I.R.V.; Validation: A.M., S.R., I.R.V.; Visualization: D.C., M.E.P., T.R., I.R.V.; Writing – original draft: A.M.; Writing – review & editing: all authors.

DECLARATION OF INTERESTS

The authors have no interest to declare.

Received: January 14, 2022

Revised: April 1, 2022

Accepted: April 22, 2022

Published: May 5, 2022

REFERENCES

- Adams, P.D., Afonine, P.V., Bunkoczi, G., Chen, V.B., Davis, I.W., Echols, N., Headd, J.J., Hung, L.W., Kapral, G.J., Grosse-Kunstleve, R.W., et al. (2010). PHENIX: a comprehensive Python-based system for macromolecular structure solution. *Acta Crystallogr. D Biol. Crystallogr.* 66, 213–221. <https://doi.org/10.1107/s0907444909052925>.
- Ali-Ahmad, A., Bilokapic, S., Schafer, I.B., Halic, M., and Sekulic, N. (2019). CENP-C unwraps the human CENP-A nucleosome through the H2A C-terminal tail. *EMBO Rep.* 20, e48913. <https://doi.org/10.15252/embr.201948913>.
- Allu, P.K., Dawicki-McKenna, J.M., Van Eeuwen, T., Slavin, M., Braitbard, M., Xu, C., Kalisman, N., Murakami, K., and Black, B.E. (2019). Structure of the human core centromeric nucleosome complex. *Curr. Biol.* 29, 2625–2639.e5. <https://doi.org/10.1016/j.cub.2019.06.062>.
- Ando, S., Yang, H., Nozaki, N., Okazaki, T., and Yoda, K. (2002). CENP-A, -B, and -C chromatin complex that contains the l-type alpha-satellite array constitutes the prekinetochore in HeLa cells. *Mol. Cell Biol.* 22, 2229–2241. <https://doi.org/10.1128/mcb.22.7.2229-2241.2002>.
- Ariyoshi, M., Makino, F., Watanabe, R., Nakagawa, R., Kato, T., Namba, K., Arimura, Y., Fujita, R., Kurumizaka, H., Okumura, E.I., et al. (2021). Cryo-EM structure of the CENP-A nucleosome in complex with phosphorylated CENP-C. *EMBO J.* 40, e105671. <https://doi.org/10.15252/embj.2020105671>.
- Basilico, F., Maffini, S., Weir, J.R., Prumbaum, D., Rojas, A.M., Zimniak, T., De Antoni, A., Jeganathan, S., Voss, B., van Gerwen, S., et al. (2014). The pseudo GTPase CENP-M drives human kinetochore assembly. *Elife* 3, e02978. <https://doi.org/10.7554/elife.02978>.
- Black, B.E., and Cleveland, D.W. (2011). Epigenetic centromere propagation and the nature of CENP-A nucleosomes. *Cell* 144, 471–479. <https://doi.org/10.1016/j.cell.2011.02.002>.
- Black, B.E., Foltz, D.R., Chakravarthy, S., Luger, K., Woods, V.L., Jr., and Cleveland, D.W. (2004). Structural determinants for generating centromeric chromatin. *Nature* 430, 578–582. <https://doi.org/10.1038/nature02766>.
- Black, B.E., Jansen, L.E., Maddox, P.S., Foltz, D.R., Desai, A.B., Shah, J.V., and Cleveland, D.W. (2007). Centromere identity maintained by nucleosomes assembled with histone H3 containing the CENP-A targeting domain. *Mol. Cell* 25, 309–322. <https://doi.org/10.1016/j.molcel.2006.12.018>.
- Bloom, K.S., and Carbon, J. (1982). Yeast centromere DNA is in a unique and highly ordered structure in chromosomes and small circular minichromosomes. *Cell* 29, 305–317. [https://doi.org/10.1016/0092-8674\(82\)90147-7](https://doi.org/10.1016/0092-8674(82)90147-7).
- Bodor, D.L., Rodriguez, M.G., Moreno, N., and Jansen, L.E. (2012). Analysis of protein turnover by quantitative SNAP-based pulse-chase imaging. *Curr. Protoc. Cell Biol Chapter 8. Unit8 8*. <https://doi.org/10.1002/0471143030.cb0808s55>.
- Brocker, C., Kuhlee, A., Gatsogiannis, C., kleine Balderhaar, H.J., Honscher, C., Engelbrecht-Vandre, S., Ungermann, C., and Raunser, S. (2012). Molecular architecture of the multisubunit homotypic fusion and vacuole protein sorting (HOPS) tethering complex. *Proc. Natl. Acad. Sci. U S A.* 109, 1991–1996. <https://doi.org/10.1073/pnas.1117797109>.
- Camahort, R., Shivaraju, M., Mattingly, M., Li, B., Nakanishi, S., Zhu, D., Shilatifard, A., Workman, J.L., and Gerton, J.L. (2009). Cse4 is part of an octameric nucleosome in budding yeast. *Mol. Cell* 35, 794–805. <https://doi.org/10.1016/j.molcel.2009.07.022>.
- Carroll, C.W., Milks, K.J., and Straight, A.F. (2010). Dual recognition of CENP-A nucleosomes is required for centromere assembly. *J. Cell Biol* 189, 1143–1155. <https://doi.org/10.1083/jcb.201001013>.
- Carroll, C.W., Silva, M.C., Godek, K.M., Jansen, L.E., and Straight, A.F. (2009). Centromere assembly requires the direct recognition of CENP-A nucleosomes by CENP-N. *Nat. Cell Biol* 11, 896–902. <https://doi.org/10.1038/ncb1899>.
- Chen, V.B., Arendall, W.B., 3rd, Headd, J.J., Keedy, D.A., Immormino, R.M., Kapral, G.J., Murray, L.W., Richardson, J.S., and Richardson, D.C. (2010). MolProbity: all-atom structure validation for macromolecular crystallography. *Acta Crystallogr. D Biol. Crystallogr.* 66, 12–21. <https://doi.org/10.1107/s0907444909042073>.
- Chik, J.K., Moiseeva, V., Goel, P.K., Meinen, B.A., Koldewey, P., An, S., Mellone, B.G., Subramanian, L., and Cho, U.S. (2019). Structures of CENP-C cupin domains at regional centromeres reveal unique patterns of dimerization and recruitment functions for the inner pocket. *J. Biol. Chem.* 294, 14119–14134. <https://doi.org/10.1074/jbc.ra119.008464>.
- Chittori, S., Hong, J., Saunders, H., Feng, H., Ghirlando, R., Kelly, A.E., Bai, Y., and Subramanian, S. (2018). Structural mechanisms of centromeric nucleosome recognition by the kinetochore protein CENP-N. *Science* 359, 339–343. <https://doi.org/10.1126/science.aar2781>.
- Cho, U.S., and Harrison, S.C. (2011). Recognition of the centromere-specific histone Cse4 by the chaperone Scm3. *Proc. Natl. Acad. Sci. U S A.* 108, 9367–9371. <https://doi.org/10.1073/pnas.1106389108>.
- Cohen, R.L., Espelin, C.W., De Wulf, P., Sorger, P.K., Harrison, S.C., and Simons, K.T. (2008). Structural and functional dissection of Mif2p, a conserved DNA-binding kinetochore protein. *Mol. Biol. Cell* 19, 4480–4491. <https://doi.org/10.1091/mbc.e08-03-0297>.
- Cole, H.A., Howard, B.H., and Clark, D.J. (2011). The centromeric nucleosome of budding yeast is perfectly positioned and covers the entire centromere. *Proc. Natl. Acad. Sci. U S A.* 108, 12687–12692. <https://doi.org/10.1073/pnas.1104978108>.
- Dalal, Y., Furuyama, T., Vermaak, D., and Henikoff, S. (2007). Structure, dynamics, and evolution of centromeric nucleosomes. *Proc. Natl. Acad. Sci. U S A.* 104, 15974–15981. <https://doi.org/10.1073/pnas.0707648104>.
- Dechassa, M.L., Wyns, K., Li, M., Hall, M.A., Wang, M.D., and Luger, K. (2011). Structure and Scm3-mediated assembly of budding yeast centromeric nucleosomes. *Nat. Commun.* 2, 313. <https://doi.org/10.1038/ncomms1320>.
- Diaz-Ingelmo, O., Martinez-Garcia, B., Segura, J., Valdes, A., and Roca, J. (2015). DNA Topology and global architecture of point centromeres. *Cell Rep* 13, 667–677. <https://doi.org/10.1016/j.celrep.2015.09.039>.
- Drinnenberg, I.A., and Akiyoshi, B. (2017). Evolutionary Lessons from species with unique kinetochores. *Prog. Mol. Subcell Biol.* 56, 111–138. https://doi.org/10.1007/978-3-319-58592-5_5.
- Dunleavy, E.M., Zhang, W., and Karpen, G.H. (2013). Solo or doppio: how many CENP-As make a centromeric nucleosome? *Nat. Struct. Mol. Biol.* 20, 648–650. <https://doi.org/10.1038/nsmb.2602>.
- Eickbush, T.H., Godfrey, J.E., Elia, M.C., and Moudrianakis, E.N. (1988). H2a-specific proteolysis as a unique probe in the analysis of the histone octamer. *J. Biol. Chem.* 263, 18972–18978. [https://doi.org/10.1016/s0021-9258\(18\)37377-0](https://doi.org/10.1016/s0021-9258(18)37377-0).
- Emsley, P., Lohkamp, B., Scott, W.G., and Cowtan, K. (2010). Features and development of Coot. *Acta Crystallogr. D Biol. Crystallogr.* 66, 486–501. <https://doi.org/10.1107/S0907444910007493>.
- Evans, R., O'Neill, M., Pritzel, A., Antropova, N., Senior, A., Green, T., Židek, A., Bates, R., Blackwell, S., Yim, J., et al. (2021). Protein Complex Prediction with AlphaFold-Multimer (BioRxiv).
- Fachinetti, D., Han, J.S., McMahon, M.A., Ly, P., Abdullah, A., Wong, A.J., and Cleveland, D.W. (2015). DNA sequence-specific binding of CENP-B enhances the fidelity of human centromere function. *Dev. Cell* 33, 314–327. <https://doi.org/10.1016/j.devcel.2015.03.020>.

- Fang, J., Liu, Y., Wei, Y., Deng, W., Yu, Z., Huang, L., Teng, Y., Yao, T., You, Q., Ruan, H., et al. (2015). Structural transitions of centromeric chromatin regulate the cell cycle-dependent recruitment of CENP-N. *Genes Dev.* 29, 1058–1073. <https://doi.org/10.1101/gad.259432.115>.
- Fernandez-Leiro, R., and Scheres, S.H.W. (2017). A pipeline approach to single-particle processing in RELION. *Acta Crystallogr. D Struct. Biol.* 73, 496–502. <https://doi.org/10.1107/S2059798316019276>.
- Fitzgerald-Hayes, M., Clarke, L., and Carbon, J. (1982). Nucleotide sequence comparisons and functional analysis of yeast centromere DNAs. *Cell* 29, 235–244. [https://doi.org/10.1016/0092-8674\(82\)90108-8](https://doi.org/10.1016/0092-8674(82)90108-8).
- Foltz, D.R., Jansen, L.E.T., Black, B.E., Bailey, A.O., Yates, J.R., 3rd, and Cleveland, D.W. (2006). The human CENP-A centromeric nucleosome-associated complex. *Nat. Cell Biol.* 8, 458–469. <https://doi.org/10.1038/ncb1397>.
- Furuyama, S., and Biggins, S. (2007). Centromere identity is specified by a single centromeric nucleosome in budding yeast. *Proc. Natl. Acad. Sci. U S A.* 104, 14706–14711. <https://doi.org/10.1073/pnas.0706985104>.
- Furuyama, T., Codomo, C.A., and Henikoff, S. (2013). Reconstitution of hemisomes on budding yeast centromeric DNA. *Nucleic Acids Res.* 41, 5769–5783. <https://doi.org/10.1093/nar/gkt314>.
- Furuyama, T., and Henikoff, S. (2009). Centromeric nucleosomes induce positive DNA supercoils. *Cell* 138, 104–113. <https://doi.org/10.1016/j.cell.2009.04.049>.
- Gambogi, C.W., and Black, B.E. (2019). The nucleosomes that mark centromere location on chromosomes old and new. *Essays Biochem.* 63, 15–27. <https://doi.org/10.1042/ebc20180060>.
- Gascoigne, K.E., Takeuchi, K., Suzuki, A., Hori, T., Fukagawa, T., and Cheeseman, I.M. (2011). Induced ectopic kinetochore assembly bypasses the requirement for CENP-A nucleosomes. *Cell* 145, 410–422. <https://doi.org/10.1016/j.cell.2011.03.031>.
- Guo, L.Y., Allu, P.K., Zandarashvili, L., McKinley, K.L., Sekulic, N., Dawicki-McKenna, J.M., Fachinetti, D., Logsdon, G.A., Jamiolkowski, R.M., Cleveland, D.W., et al. (2017). Centromeres are maintained by fastening CENP-A to DNA and directing an arginine anchor-dependent nucleosome transition. *Nat. Commun.* 8, 15775. <https://doi.org/10.1038/ncomms15775>.
- Guse, A., Fuller, C.J., and Straight, A.F. (2012). A cell-free system for functional centromere and kinetochore assembly. *Nat. Protoc.* 7, 1847–1869. <https://doi.org/10.1038/nprot.2012.112>.
- Ha, J.Y., Kim, H.K., Kim, D.J., Kim, K.H., Oh, S.J., Lee, H.H., Yoon, H.J., Song, H.K., and Suh, S.W. (2007). The recombination-associated protein RdcC adopts a novel toroidal architecture for DNA binding. *Nucleic Acids Res.* 35, 2671–2681. <https://doi.org/10.2210/pdb2owjy/pdb>.
- Hamilton, G., Dimitrova, Y., and Davis, T.N. (2019). Seeing is believing: our evolving view of kinetochore structure, composition, and assembly. *Curr. Opin. Cell Biol.* 60, 44–52. <https://doi.org/10.1016/j.cob.2019.03.016>.
- Hasson, D., Panchenko, T., Salimian, K.J., Salman, M.U., Sekulic, N., Alonso, A., Warburton, P.E., and Black, B.E. (2013). The octamer is the major form of CENP-A nucleosomes at human centromeres. *Nat. Struct. Mol. Biol.* 20, 687–695. <https://doi.org/10.1038/nsmb.2562>.
- Henikoff, S., Ramachandran, S., Krassovsky, K., Bryson, T.D., Codomo, C.A., Brogaard, K., Widom, J., Wang, J.P., and Henikoff, J.G. (2014). The budding yeast Centromere DNA Element II wraps a stable Cse4 hemisome in either orientation in vivo. *Elife* 3, e01861. <https://doi.org/10.7554/elife.01861>.
- Hinshaw, S.M., and Harrison, S.C. (2013). An Iml3-Chl4 heterodimer links the core centromere to factors required for accurate chromosome segregation. *Cell Rep* 5, 29–36. <https://doi.org/10.2210/pdb4je3/pdb>.
- Hinshaw, S.M., and Harrison, S.C. (2019). The structure of the Ctf19c/CCAN from budding yeast. *Elife* 8. <https://doi.org/10.7554/elife.44239>.
- Hinshaw, S.M., and Harrison, S.C. (2020). The structural basis for kinetochore stabilization by Cnn1/CENP-T. *Curr. Biol.* 30, 3425–3431.e3. <https://doi.org/10.1016/j.cub.2020.06.024>.
- Hoffmann, S., Izquierdo, H.M., Gamba, R., Chardon, F., Dumont, M., Keizer, V., Herve, S., McNulty, S.M., Sullivan, B.A., Manel, N., and Fachinetti, D. (2020). A genetic memory initiates the epigenetic loop necessary to preserve centromere position. *EMBO J.* 39, e105505. <https://doi.org/10.15252/embj.2020105505>.
- Hori, T., Amano, M., Suzuki, A., Backer, C.B., Welburn, J.P., Dong, Y., McEwen, B.F., Shang, W.H., Suzuki, E., Okawa, K., et al. (2008). CCAN makes multiple contacts with centromeric DNA to provide distinct pathways to the outer kinetochore. *Cell* 135, 1039–1052. <https://doi.org/10.1016/j.cell.2008.10.019>.
- Hornung, P., Troc, P., Malvezzi, F., Maier, M., Demianova, Z., Zimniak, T., Litos, G., Lampert, F., Schleiffer, A., Brunner, M., et al. (2014). A cooperative mechanism drives budding yeast kinetochore assembly downstream of CENP-A. *J. Cell Biol.* 206, 509–524. <https://doi.org/10.1083/jcb.201403081>.
- Huang, C.C., Chang, K.M., Cui, H., and Jayaram, M. (2011). Histone H3-variant Cse4-induced positive DNA supercoiling in the yeast plasmid has implications for a plasmid origin of a chromosome centromere. *Proc. Natl. Acad. Sci. U S A.* 108, 13671–13676. <https://doi.org/10.1073/pnas.1101944108>.
- Izuta, H., Ikeno, M., Suzuki, N., Tomonaga, T., Nozaki, N., Obuse, C., Kisu, Y., Goshima, N., Nomura, F., Nomura, N., and Yoda, K. (2006). Comprehensive analysis of the ICEN (Interphase Centromere Complex) components enriched in the CENP-A chromatin of human cells. *Genes Cells* 11, 673–684. <https://doi.org/10.1111/j.1365-2443.2006.00969.x>.
- Jansen, L.E., Black, B.E., Foltz, D.R., and Cleveland, D.W. (2007). Propagation of centromeric chromatin requires exit from mitosis. *J. Cell Biol.* 176, 795–805. <https://doi.org/10.1083/jcb.200701066>.
- Jumper, J., Evans, R., Pritzel, A., Green, T., Figurnov, M., Ronneberger, O., Tunyasuvunakool, K., Bates, R., Zidek, A., Potapenko, A., et al. (2021). Highly accurate protein structure prediction with AlphaFold. *Nature* 596, 583–589. <https://doi.org/10.1038/s41586-021-03819-2>.
- Kabsch, W., and Sander, C. (1983). Dictionary of protein secondary structure: pattern recognition of hydrogen-bonded and geometrical features. *Biopolymers* 22, 2577–2637. <https://doi.org/10.1002/bip.360221211>.
- Kastner, B., Fischer, N., Golas, M.M., Sander, B., Dube, P., Boehringer, D., Hartmuth, K., Deckert, J., Hauer, F., Wolf, E., et al. (2008). GraFix: sample preparation for single-particle electron cryomicroscopy. *Nat. Methods* 5, 535–539. <https://doi.org/10.1038/nmeth1139>.
- Kato, H., Jiang, J., Zhou, B.R., Rozendaal, M., Feng, H., Ghirlando, R., Xiao, T.S., Straight, A.F., and Bai, Y. (2013). A conserved mechanism for centromeric nucleosome recognition by centromere protein CENP-C. *Science* 340, 1110–1113. <https://doi.org/10.1126/science.1235532>.
- Keith, K.C., and Fitzgerald-Hayes, M. (2000). CSE4 genetically interacts with the *Saccharomyces cerevisiae* centromere DNA elements CDE I and CDE II but not CDE III. Implications for the centromere dna around a cse4p variant nucleosome. *Genetics* 156, 973–981. <https://doi.org/10.1093/genetics/156.3.973>.
- Kidmose, R.T., Juhl, J., Nissen, P., Boesen, T., Karlsen, J.L., and Pedersen, B.P. (2019). Namdinator - automatic molecular dynamics flexible fitting of structural models into cryo-EM and crystallography experimental maps. *IUCr* 6, 526–531. <https://doi.org/10.1107/s2052252519007619>.
- Kixmoeller, K., Allu, P.K., and Black, B.E. (2020). The centromere comes into focus: from CENP-A nucleosomes to kinetochore connections with the spindle. *Open Biol.* 10, 200051. <https://doi.org/10.1098/rsob.200051>.
- Klare, K., Weir, J.R., Basilico, F., Zimniak, T., Massimiliano, L., Ludwigs, N., Herzog, F., and Musacchio, A. (2015). CENP-C is a blueprint for constitutive centromere-associated network assembly within human kinetochores. *J. Cell Biol.* 210, 11–22. <https://doi.org/10.1083/jcb.201412028>.
- Krassovsky, K., Henikoff, J.G., and Henikoff, S. (2012). Tripartite organization of centromeric chromatin in budding yeast. *Proc. Natl. Acad. Sci. U S A.* 109, 243–248. <https://doi.org/10.1073/pnas.1118898109>.
- Li, X., Mooney, P., Zheng, S., et al. (2013). Electron counting and beam-induced motion correction enable near-atomic-resolution single-particle cryo-EM. *Nat Methods* 10, 584–590. <https://doi.org/10.1038/nmeth.2472>.
- McKinley, K.L., and Cheeseman, I.M. (2016). The molecular basis for centromere identity and function. *Nat. Rev. Mol. Cell Biol.* 17, 16–29. <https://doi.org/10.1038/nrm.2015.5>.

- McKinley, K.L., Sekulic, N., Guo, L.Y., Tsinman, T., Black, B.E., and Cheeseman, I.M. (2015). The CENP-L-N complex forms a Critical Node in an integrated Meshwork of interactions at the centromere-kinetochore interface. *Mol. Cell* 60, 886–898. <https://doi.org/10.1016/j.molcel.2015.10.027>.
- Medina-Pritchard, B., Lazou, V., Zou, J., Byron, O., Abad, M.A., Rappsilber, J., Heun, P., and Jeyaparakash, A.A. (2020). Structural basis for centromere maintenance by Drosophila CENP-A chaperone CAL1. *EMBO J.* 39. e103234. <https://doi.org/10.15252/embj.2019103234>.
- Mellone, B.G., and Fachinetti, D. (2021). Diverse mechanisms of centromere specification. *Curr. Biol.* 31, R1491–R1504. <https://doi.org/10.1016/j.cub.2021.09.083>.
- Meluh, P.B., Yang, P., Glowczewski, L., Koshland, D., and Smith, M.M. (1998). Cse4p is a component of the core centromere of *Saccharomyces cerevisiae*. *Cell* 94, 607–613. [https://doi.org/10.1016/s0092-8674\(00\)81602-5](https://doi.org/10.1016/s0092-8674(00)81602-5).
- Mirdita, M., Schütze, K., Moriawaki, L., Ovchinnikov, S., and Steinegger, M. (2021). ColabFold - making protein folding accessible to all. *BioRxiv*.
- Mizuguchi, G., Xiao, H., Wisniewski, J., Smith, M.M., and Wu, C. (2007). Nonhistone Scm3 and histones CenH3-H4 assemble the core of centromere-specific nucleosomes. *Cell* 129, 1153–1164. <https://doi.org/10.1016/j.cell.2007.04.026>.
- Moriya, T., Saur, M., Stabrin, M., Merino, F., Voicu, H., Huang, Z., Penczek, P.A., Raunser, S., and Gatsogiannis, C. (2017). High-resolution single particle analysis from electron cryo-microscopy images using SPHIRE. *J. Vis. Exp.* 55448. <https://doi.org/10.3791/55448>.
- Musacchio, A., and Desai, A. (2017). A molecular view of kinetochore assembly and function. *Biology (Basel)* 6, 5. <https://doi.org/10.3390/biology6010005>.
- Nagpal, H., Hori, T., Furukawa, A., Sugase, K., Osakabe, A., Kurumizaka, H., and Fukagawa, T. (2015a). Dynamic changes in CCAN organization through CENP-C during cell-cycle progression. *Mol. Biol. Cell* 26, 3768–3776. <https://doi.org/10.1091/mbc.e15-07-0531>.
- Nakane, T., Kimanius, D., Lindahl, E., and Scheres, S.H. (2018). Characterisation of molecular motions in cryo-EM single-particle data by multi-body refinement in RELION. *Elife* 7. <https://doi.org/10.7554/elife.36861>.
- Navarro-Mendoza, M.I., Perez-Arques, C., Panchal, S., Nicolas, F.E., Mondo, S.J., Ganguly, P., Pangilinan, J., Grigoriev, I.V., Heitman, J., Sanyal, K., and Garre, V. (2019). Early diverging Fungus *mucor circinelloides* lacks centromeric histone CENP-A and displays a Mosaic of point and regional centromeres. *Curr. Biol.* 29, 3791–3802.e6. <https://doi.org/10.1016/j.cub.2019.09.024>.
- Nechemia-Arbely, Y., Fachinetti, D., Miga, K.H., Sekulic, N., Soni, G.V., Kim, D.H., Wong, A.K., Lee, A.Y., Nguyen, K., Dekker, C., et al. (2017). Human centromeric CENP-A chromatin is a homotypic, octameric nucleosome at all cell cycle points. *J. Cell Biol* 216, 607–621. <https://doi.org/10.1083/jcb.201608083>.
- Nishino, T., Takeuchi, K., Gascoigne, K.E., Suzuki, A., Hori, T., Oyama, T., Morikawa, K., Cheeseman, I.M., and Fukagawa, T. (2012). CENP-T-W-S-X forms a unique centromeric chromatin structure with a histone-like fold. *Cell* 148, 487–501. <https://doi.org/10.1016/j.cell.2011.11.061>.
- Obuse, C., Yang, H., Nozaki, N., Goto, S., Okazaki, T., and Yoda, K. (2004). Proteomics analysis of the centromere complex from HeLa interphase cells: UV-damaged DNA binding protein 1 (DDB-1) is a component of the CEN-complex, while BMI-1 is transiently co-localized with the centromeric region in interphase. *Genes Cells* 9, 105–120. <https://doi.org/10.1111/j.1365-2443.2004.00705.x>.
- Okada, M., Cheeseman, I.M., Hori, T., Okawa, K., McLeod, I.X., Yates, J.R., 3rd, Desai, A., and Fukagawa, T. (2006). The CENP-H-I complex is required for the efficient incorporation of newly synthesized CENP-A into centromeres. *Nat. Cell Biol* 8, 446–457. <https://doi.org/10.1038/ncb1396>.
- Pan, D., Klare, K., Petrovic, A., Take, A., Walstein, K., Singh, P., Rondelet, A., Bird, A.W., and Musacchio, A. (2017). CDK-regulated dimerization of M18BP1 on a Mis18 hexamer is necessary for CENP-A loading. *Elife* 6. <https://doi.org/10.7554/elife.23352>.
- Pentakota, S., Zhou, K., Smith, C., Maffini, S., Petrovic, A., Morgan, G.P., Weir, J.R., Vetter, I.R., Musacchio, A., and Luger, K. (2017). Decoding the Centromeric Nucleosome through CENP-N. *Elife* 6. <https://doi.org/10.7554/elife.33442>.
- Pesenti, M.E., Prumbaum, D., Auckland, P., Smith, C.M., Faesen, A.C., Petrovic, A., Erent, M., Maffini, S., Pentakota, S., Weir, J.R., et al. (2018). Reconstitution of a 26-subunit human kinetochore reveals cooperative microtubule binding by CENP-OPQUR and NDC80. *Mol. Cell* 71, 923–939.e10. <https://doi.org/10.1016/j.molcel.2018.07.038>.
- Petterson, E.F., Goddard, T.D., Huang, C.C., Couch, G.S., Greenblatt, D.M., Meng, E.C., and Ferrin, T.E. (2004). UCSF Chimera—a visualization system for exploratory research and analysis. *J. Comput. Chem.* 25, 1605–1612. <https://doi.org/10.1002/jcc.20084>.
- Petterson, E.F., Goddard, T.D., Huang, C.C., Meng, E.C., Couch, G.S., Croll, T.I., Morris, J.H., and Ferrin, T.E. (2021). UCSF ChimeraX: structure visualization for researchers, educators, and developers. *Protein Sci.* 30, 70–82. <https://doi.org/10.1002/pro.3943>.
- Pintilie, G., and Chiu, W. (2012). Comparison of Segger and other methods for segmentation and rigid-body docking of molecular components in cryo-EM density maps. *Biopolymers* 97, 742–760. <https://doi.org/10.1002/bip.22074>.
- Pinto, I., and Winston, F. (2000). Histone H2A is required for normal centromere function in *Saccharomyces cerevisiae*. *EMBO J.* 19, 1598–1612. <https://doi.org/10.1093/emboj/19.7.1598>.
- Pluta, A.F., Mackay, A.M., Ainsztein, A.M., Goldberg, I.G., and Earnshaw, W.C. (1995). The centromere: hub of chromosomal activities. *Science* 270, 1591–1594. <https://doi.org/10.1126/science.270.5242.1591>.
- Rohou, A., and Grigorieff, N. (2015). CTFIND4: fast and accurate defocus estimation from electron micrographs. *J. Struct. Biol.* 192, 216–221. <https://doi.org/10.1016/j.jsb.2015.08.008>.
- Rossi, M.J., Kuntala, P.K., Lai, W.K.M., Yamada, N., Badjatia, N., Mittal, C., Kuzu, G., Bocklund, K., Farrell, N.P., Blanda, T.R., et al. (2021). A high-resolution protein architecture of the budding yeast genome. *Nature* 592, 309–314. <https://doi.org/10.1038/s41586-021-03314-8>.
- Sanchez-Garcia, R., Gomez-Blanco, J., Cuervo, A., Carazo, J.M., Sorzano, C.O.S., and Vargan, J. (2021). DeepEMhancer: a deep learning solution for cryo-EM volume post-processing. *Commun. Biol.* 4, 874. <https://doi.org/10.1038/s42003-021-02399-1>.
- Schindelin, J., Arganda-Carreras, I., Frise, E., et al. (2012). Fiji: an open-source platform for biological-image analysis. *Nat Methods* 9, 676–682. <https://doi.org/10.1038/nmeth.2019>.
- Schuh, M., Lehner, C.F., and Heidmann, S. (2007). Incorporation of *Drosophila* CID/CENP-A and CENP-C into centromeres during early embryonic anaphase. *Curr. Biol.* 17, 237–243. <https://doi.org/10.1016/j.cub.2006.11.051>.
- Screpanti, E., De Antoni, A., Alushin, G.M., Petrovic, A., Melis, T., Nogales, E., and Musacchio, A. (2011). Direct binding of Cenp-C to the Mis12 complex joins the inner and outer kinetochore. *Curr. Biol.* 21, 391–398. <https://doi.org/10.1016/j.cub.2010.12.039>.
- Shukla, M.S., Syed, S.H., Goutte-Gattat, D., Richard, J.L.C., Montel, F., Hamiche, A., Travers, A., Faivre-Moskalenko, C., Bednar, J., Hayes, J.J., et al. (2011). The docking domain of histone H2A is required for H1 binding and RSC-mediated nucleosome remodeling. *Nucleic Acids Res.* 39, 2559–2570. <https://doi.org/10.1093/nar/gkq1174>.
- Stabrin, M., Schoenfeld, F., Wagner, T., Pospich, S., Gatsogiannis, C., and Raunser, S. (2020). TransSPHIRE: automated and feedback-optimized on-the-fly processing for cryo-EM. *Nat. Commun.* 11, 5716. <https://doi.org/10.1038/s41467-020-19513-2>.
- Tachiwana, H., Kagawa, W., Shiga, T., Osakabe, A., Miya, Y., Saito, K., Hayashi-Takanaka, Y., Oda, T., Sato, M., Park, S.Y., et al. (2011). Crystal structure of the human centromeric nucleosome containing CENP-A. *Nature* 476, 232–235. <https://doi.org/10.1038/nature10258>.
- Takeuchi, K., Nishino, T., Mayanagi, K., Horikoshi, N., Osakabe, A., Tachiwana, H., Hori, T., Kurumizaka, H., and Fukagawa, T. (2014). The centromeric nucleosome-like CENP-T-W-S-X complex induces positive supercoils

- into DNA. *Nucleic Acids Res.* 42, 1644–1655. <https://doi.org/10.1093/nar/gkt1124>.
- Talbert, P.B., and Henikoff, S. (2020). What makes a centromere? *Exp. Cell Res* 389, 111895. <https://doi.org/10.1016/j.yexcr.2020.111895>.
- Tian, T., Li, X., Liu, Y., Wang, C., Liu, X., Bi, G., Zhang, X., Yao, X., Zhou, Z.H., and Zang, J. (2018). Molecular basis for CENP-N recognition of CENP-A nucleosome on the human kinetochore. *Cell Res* 28, 374–378. <https://doi.org/10.1038/cr.2018.13>.
- Tromer, E.C., van Hooff, J.J.E., Kops, G.J.P.L., and Snel, B. (2019). Mosaic origin of the eukaryotic kinetochore. *Proc. Natl. Acad. Sci. U S A.* 116, 12873–12882. <https://doi.org/10.1073/pnas.1821945116>.
- van Hooff, J.J., Tromer, E., van Wijk, L.M., Snel, B., and Kops, G.J. (2017). Evolutionary dynamics of the kinetochore network in eukaryotes as revealed by comparative genomics. *EMBO Rep.* 18, 1559–1571. <https://doi.org/10.15252/embr.201744102>.
- Veevers, R., and Hayward, S. (2019). Methodological improvements for the analysis of domain movements in large biomolecular complexes. *Biophys. Physicobiol* 16, 328–336. https://doi.org/10.2142/biophysico.16.0_328.
- Wagner, T., Merino, F., Stabrin, M., Moriya, T., Antoni, C., Apelbaum, A., Hagel, P., Sitsel, O., Raisch, T., Prumbaum, D., et al. (2019). SPHIRE-crYOLO is a fast and accurate fully automated particle picker for cryo-EM. *Commun. Biol.* 2, 218. <https://doi.org/10.1038/s42003-019-0437-z>.
- Walstein, K., Petrovic, A., Pan, D., Hagemeyer, B., Vogt, D., Vetter, I.R., and Musacchio, A. (2021). Assembly principles and stoichiometry of a complete human kinetochore module. *Sci. Adv.* 7, eabg1037. <https://doi.org/10.1126/sciadv.abg1037>.
- Watanabe, R., Hirano, Y., Hara, M., Hiraoka, Y., and Fukagawa, T. (2022). Mobility of kinetochore proteins measured by FRAP analysis in living cells. *Chromosome Res.* 30, 43–57. <https://doi.org/10.1007/s10577-021-09678-x>.
- Weir, J.R., Faesen, A.C., Klare, K., Petrovic, A., Basilico, F., Fischbock, J., Pentakota, S., Keller, J., Pesenti, M.E., Pan, D., et al. (2016). Insights from biochemical reconstitution into the architecture of human kinetochores. *Nature* 537, 249–253. <https://doi.org/10.1038/nature19333>.
- Weissmann, F., Petzold, G., VanderLinden, R., Huis in 't Veld, P.J., Brown, N.G., Lampert, F., Westermann, S., Stark, H., Schulman, B.A., and Peters, J.M. (2016). biGBac enables rapid gene assembly for the expression of large multisubunit protein complexes. *Proc. Natl. Acad. Sci. U S A.* 113, E2564–E2569.
- Westermann, S., Cheeseman, I.M., Anderson, S., Yates, J.R., 3rd, Drubin, D.G., and Barnes, G. (2003). Architecture of the budding yeast kinetochore reveals a conserved molecular core. *J. Cell Biol* 163, 215–222. <https://doi.org/10.1083/jcb.200305100>.
- Williams, J.S., Hayashi, T., Yanagida, M., and Russell, P. (2009). Fission yeast Scm3 mediates stable assembly of Cnp1/CENP-A into centromeric chromatin. *Mol. Cell* 33, 287–298. <https://doi.org/10.1016/j.molcel.2009.01.017>.
- Wisniewski, J., Hajj, B., Chen, J., Mizuguchi, G., Xiao, H., Wei, D., Dahan, M., and Wu, C. (2014). Imaging the fate of histone Cse4 reveals de novo replacement in S phase and subsequent stable residence at centromeres. *Elife* 3, e02203. <https://doi.org/10.7554/elife.02203>.
- Xiao, H., Mizuguchi, G., Wisniewski, J., Huang, Y., Wei, D., and Wu, C. (2011). Nonhistone Scm3 binds to AT-rich DNA to organize atypical centromeric nucleosome of budding yeast. *Mol. Cell* 43, 369–380. <https://doi.org/10.1016/j.molcel.2011.07.009>.
- Xiao, H., Wang, F., Wisniewski, J., Shaytan, A.K., Ghirlando, R., FitzGerald, P.C., Huang, Y., Wei, D., Li, S., Landsman, D., et al. (2017). Molecular basis of CENP-C association with the CENP-A nucleosome at yeast centromeres. *Genes Dev.* 31, 1958–1972. <https://doi.org/10.1101/gad.304782.117>.
- Yan, K., Yang, J., Zhang, Z., McLaughlin, S.H., Chang, L., Fasci, D., Ehrenhofer-Murray, A.E., Heck, A.J.R., and Barford, D. (2019). Structure of the inner kinetochore CCAN complex assembled onto a centromeric nucleosome. *Nature* 574, 278–282. <https://doi.org/10.1038/s41586-019-1609-1>.
- Yang, Z., Lasker, K., Schneidman-Duhovny, D., Webb, B., Huang, C.C., Pettersen, E.F., Goddard, T.D., Meng, E.C., Sali, A., and Ferrin, T.E. (2012). UCSF Chimera, MODELLER, and IMP: an integrated modeling system. *J. Struct. Biol.* 179, 269–278. <https://doi.org/10.1016/j.jsb.2011.09.006>.
- Yatskevich, S., Muir, K.W., Bellini, D., Zhang, Z., Yang, J., Tischer, T., Predin, M., Dendooven, T., McLaughlin, S.H., and Barford, D. (2022). Structure of the human inner kinetochore bound to a centromeric CENP-A nucleosome. *Science*. eabn3810. <https://doi.org/10.1126/science.abn3810>.
- Zhang, Z., Bellini, D., and Barford, D. (2020). Crystal structure of the Cenp-HIKHead-TW sub-module of the inner kinetochore CCAN complex. *Nucleic Acids Res.* 48, 11172–11184. <https://doi.org/10.1093/nar/gkaa772>.
- Zheng, S.Q., Palovcak, E., Armache, J.P., Verba, K.A., Cheng, Y., and Agard, D.A. (2017). MotionCor2: anisotropic correction of beam-induced motion for improved cryo-electron microscopy. *Nat. Methods* 14, 331–332. <https://doi.org/10.1038/nmeth.4193>.
- Zhou, K., Gebala, M., Woods, D., Sundararajan, K., Edwards, G., Krzizike, D., Wereszczynski, J., Straight, A.F., and Luger, K. (2021). CENP-N Promotes the Compaction of Centromeric Chromatin (BioRxiv). <https://doi.org/10.1038/s41594-022-00758-y>.

STAR★METHODS

KEY RESOURCES TABLE

REAGENT or RESOURCE	SOURCE	IDENTIFIER
Antibodies		
Human CREST sera/anti-centromere	Antibodies Inc.	#9101-02; RRID:AB_2687472
Mouse anti-CENP-A	GeneTex	#GTX13939; RRID:AB_369391
Rabbit anti-CENP-HK	Klare et al. (2015)	SI0930
Rabbit anti-CENP-TW	Klare et al. (2015)	SI0822
Donkey anti-human DyLight 405	Jackson Immuno Research	#709-475-149; RRID:AB_2340553
Goat anti-mouse Rhodamine Red	Jackson Immuno Research	#115-295-003; RRID:AB_2338756
Donkey anti-rabbit Alexa Fluor 647	Jackson Immuno Research	#711-605-152; RRID:AB_2492288
Rabbit anti-CyclinB1	Abcam	#ab32053; RRID:AB_731779
Mouse anti PCNA	Cell Signaling	#2586S; RRID:AB_2160343
Rat anti Tubulin	Abcam	#6160; RRID:AB_1140548
Donkey anti-mouse Alexa Fluor 647	Invitrogen	#6160; RRID:AB_1140548
Donkey anti-rabbit Rhodamine Red	Jackson Immuno Research	#711-295-152; RRID:AB_2340613
GFP-Booster Alexa Fluor 488	Chromotek	Gb2AF488; RRID:AB_2827573
Goat anti-human Alexa Fluor 647	Jackson Immuno Research	#109-605-003; RRID:AB_2337880
Bacterial and virus strains		
E.coli: BL21CodonPlus(DE3)-RIL strain	Agilent Technologies	Cat#230280
S.frugiperda:Sf9 cells	ThermoFisher	Cat#12659017
Trichoplusia ni:BTI-Tnao38	Garry W Blissard Lab	N/A
Chemicals, peptides, and recombinant proteins		
CENP-LN complex	Pentakota et al. (2017)	N/A
CENP-C(1-544)HKIM	This study	N/A
CENP-HKIM	This study	N/A
CENP-OPQUR complex	Pesenti et al. (2018)	N/A
CENP-TWSX complex	Walstein et al. (2021)	N/A
CENP-SX complex	Walstein et al. (2021)	N/A
CENP-TW complex	Walstein et al. (2021)	N/A
CENP-A nucleosomes (145 bp)	Walstein et al. (2021)	N/A
CENP-A nucleosomes (199 bp)	This study	N/A
Alexa Fluor 647C5 maleimide Protein labeling kit	ThermoFisher	Cat#A20347
Amylose resin	New England Biolabs	Cat#E8022
Streptavidin UltraLink Resin	Thermo Scientific	Cat#53114
400 mesh carbon-coated copper grids	Plano	G2400C
Uranyl Formate	SPI Supplies	Cas#16984-59-1
UltraAuFoil	QuantiFoil	N/A
Indole-3-acetic acid (IAA)	Merck	#I5148
DAPI	Sigma	Cat#D9542
Poly-D-Lysine	Sigma-Aldrich	Cat#A003E
Mowiol	Calbiochem	Cat#475904
Deposited data		
human CCAN EM map and structure	This study	PDB: 7QOO and EMBD-14098
human CCAN-TW EM map	This study	EMDB-14099
Mendeley Dataset including uncropped microscopy images, SDS-PAGE scans, and spreadsheets of their quantification	This study	https://doi.org/10.17632/9smdtm4msj.1

(Continued on next page)

REAGENT or RESOURCE	SOURCE	IDENTIFIER
Continued		
Experimental models: Cell lines		
Human DLD-1: CENP-C ^{AID-EYFP/AID-EYFP}	Fachinetti et al. (2015)	N/A
Human DLD-1: CENP-A ^{EA/-} CENP-C ^{AmC/A}	Hoffmann et al. (2020)	N/A
HeLa Flip-In T-Rex EGFP-CENP-M	Basilico et al. (2014)	N/A
Oligonucleotides		
Primer GTGGACACTCTAAGGATCCGG	This study	N/A
Primer: Biotin-TEG- CCGGATCCTTAG AGTGTCACCATC	This study	N/A
75bp-DNA: ATCCGTGGTAGAATAG 3GAAATATCTTCCTATAGAACTAG ACAGAATGATTCTCAGAAACTCCT TTGTGATGGAT	This study	N/A
165bp-DNA: GTGGTAGAATAGGAAATATCTTCC TATAGAACTAGACAGAATGATTC TCAGAACTCCTTTGTGATGTGTG CGTTCAACTCACAGAGTTAACCT TTCTTTTCATAGAGCAGTTAGGAA ACACTCTGTTTGTAAATGTCTGCAA GTGGATATTCAGACGCCCTTG	This study	N/A
199bp-DNA: ATCGCCCTTGAGGCCTTCGTTGGAA ACGGGATTTCTTCATATTCTGCTAGA CAGAAGAATTCTCAGTAACTTCCTTG TGTTGTGTGATTCAACTCACAGAGTT GAACGATCCTTTACACAGAGCAGACT TGAACACTCTTTTTGTGGAATTTGCA GGCCTAGATTTAGCCGCTTTGAGGT CAATCACCCCGTGGAT	This study	N/A
Recombinant DNA		
pLIB	Addgene	Cat#80610
pLIB_6His-CENP-I	This study	N/A
pLIB_CENP-I	This study	N/A
pBiga	Addgene	CAT#80611
pBIGa_6His-CENP-C(1-544)_H_K_I_M	This study	N/A
pBIGa_6His-CENP-I_H_K_M	This study	N/A
pETDuet-1	Novagen	Cat#71146
pETDuet-1_6xHis-CENP-W_MBP-CENP-T	This study	N/A
pETDuet-1_6xHis-CENP-W_mScarlet-CENP-T	This study	N/A
pUC18	Addgene	Cat#50004
pUC18_199bp-DNA	This study	N/A
pUC18_165bp-DNA	This study	N/A
pUC18_75bp-DNA	This study	N/A
Software and algorithms		
EPU	Thermo Fisher Scientific	N/A
TRanSHIRE	Stabrin et al. (2020)	https://transpire.readthedocs.io/en/latest/
MOTIONCORR 2.1	(Li et al., 2013)	http://cryoem.ucsf.edu/software/driftcorr.html
CTFFIND4	Rhou and Grigorieff (2015)	http://grigoriefflab.janelia.org/ctffind4
MOTIONCOR2	Zheng et al. (2017)	http://msg.ucsf.edu/em/software/motioncor2.html
SPHIRE	Moriya et al. (2017)	http://sphaire.mpg.de
crYOLO	Wagner et al. (2019)	https://cryolo.readthedocs.io/en/stable/

(Continued on next page)

Continued

REAGENT or RESOURCE	SOURCE	IDENTIFIER
RELION 3	Scheres Lab	https://www3.mrc-lmb.cam.ac.uk/relion/index.php?title=Main_PAGE
Chimera	Pettersen et al. (2004)	https://www.cgl.ucsf.edu/chimera/
ChimeraX	Pettersen et al. (2021)	https://www.cgl.ucsf.edu/chimerax/
Segger	Pintilie and Chiu (2012)	https://www.cgl.ucsf.edu/chimera/
Pymol	Schrödinger, LLC	https://pymol.org/2/
Namdinator	Kidmose et al., 2019	https://namdinator.au.dk/about/
COOT	Emsley et al. (2010)	https://www2.mrc-lmb.cam.ac.uk/personal/pemsley/coot/
PHENIX	Adams et al. (2010)	https://www.phenix-online.org
Molprobit	Chen et al. (2010)	https://www.phenix-online.org
DeepEMhancer	Sanchez-Garcia et al. (2021)	https://github.com/rsanchezgarc/deepEMhancer
DynDom6D	Veevers and Hayward (2019)	http://dyndom.cmp.uea.ac.uk/dyndom/dyndomDownload.jsp
GraphPad Prism Version 9.0.2 (134)	GraphPad Software Inc	http://www.graphpad.com
Fiji Version 2.0.0-rc-69/1.52n	(Schindelin et al., 2012)	http://ImageJ.nih.gov/ij/
softWoRx Version 7.0	GE Healthcare	N/A
CRaQ	Bodor et al. (2012)	N/A
Image Lab	Bio-rad	https://www.bio-rad.com/de-de/product/image-lab-software?ID=KRE6P5E8Z

RESOURCE AVAILABILITY

Lead Contact

Further information and requests for resources and reagents should be directed to Andrea Musacchio (andrea.musacchio@mpi-dortmund.mpg.de).

Materials availability

Expression vectors for production of CCAN or any other in-house-generated reagent described in this manuscript are available from the Lead Contact.

Data and code availability

- The coordinates and map of the high- and low-resolution CCAN models have been submitted to the PDB with ID 7QOO and to the EMDB with IDs EMD-14098 for the high-resolution dataset and EMD-14099 for the low-resolution dataset. Uncropped microscopy images, SDS-PAGE scans, and spreadsheets of their quantification have been collected in a Mendeley dataset (<https://doi.org/10.17632/9smdtm4msj.1>).
- This paper does not report original code.
- Any additional information required to reanalyze the data reported in this paper is available from the lead contact upon request.

EXPERIMENTAL MODEL AND SUBJECT DETAILS

Cell lines and culture

HeLa Flip-In T-REx EGFP-CENP-M (Basilico et al., 2014) were maintained in DMEM with 10% tetracycline-free FBS (Pan Biotech), supplemented 50 μg/mL Penicillin/Streptomycin (PAN Biotech), and 2 mM L-glutamine (PAN Biotech) at 37 °C in a 5% CO₂ atmosphere. Flip-In T-REx DLD-1-CENP-C-AID-EYFP cells and Flip-In T-REx DLD-1-EYFP-AID-CENP-A/CENP-C-RFP-AID cells (Fachinetti et al., 2015; Hoffmann et al., 2020) were a generous gift from D. Fachinetti (Institut Curie, Paris, France) and D. C. Cleveland (University of California, San Diego, USA). The cells were cultured in Dulbecco's modified Eagle's medium (DMEM; PAN-Biotech) supplemented with 10% tetracycline-free fetal bovine serum (Thermo Fisher Scientific), 2 mM penicillin/streptomycin (PAN-Biotech), and 2 mM L-glutamine (PAN-Biotech) at 37 °C in a 5% CO₂ atmosphere.

Bacterial and insect cell lines

E. coli BL21 (DH5a) (ThermoFisher Scientific, Waltham, Massachusetts, United States), BL21(DE3)-RIL and BL21CodonPlus(DE3)-RIL (Agilent Technologies, Santa Clara, California, United States) strains were cultured on LB agar or liquid media at 37 °C LB

supplemented with ampicillin (50 mg/mL) to maintain the pETDuet plasmids and with chloramphenicol (34 mg/mL) to maintain the extra copies of tRNA Genes in CodonPlus strain. SF9 (ThermoFisher Scientific, Waltham, Massachusetts, United States) and Tnao38 (gift from Gary W. Blissard) cells were maintained in Sf-900 II medium (ThermoFisher Scientific, Waltham, Massachusetts, United States) supplemented with 10% (v/v) fetal bovine serum, at 27°C and 110 rpm orbital rotation.

Plasmids and cloning

Plasmids to express recombinant CENP-LN, -OPQR, -TWSX, -TW, -SX complexes and CENP-A containing nucleosomes were generated as previously described (Pentakota et al., 2017; Pesenti et al., 2018; Walstein et al., 2021). To generate plasmids for expressing CENP-C¹⁻⁵⁴⁴HIKM, and CENP-HIKM in insect cells, plasmids to express N-terminally 6xHis tagged CENP-C¹⁻⁵⁴⁴ and 6xHis tagged CENP-I were generated by Gibson cloning method, codon optimized cDNA of CENP-C¹⁻⁵⁴⁴ (GeneArt, Life Technologies) and CENP-I were inserted in a modified pLIB vectors containing sequences for the 6xHis followed by TEV protease. The codon optimized cDNA of CENP-I, -H, -K- and -M were inserted by Gibson cloning method into unmodified pLIB plasmids. These pLIB plasmids generated so-forth were used to insert the CENP-H, -K, -I, -M and 6His-CENP-C¹⁻⁵⁴⁴ and the CENP-H, -K, -M and 6His-CENP-I sequences into two baculovirus-based multigene-expressing vectors, pBIGa (Weissmann et al., 2016) by Gibson assembly. To generate plasmids for expressing ^{MBP}CENP-TW and ^{mScarlet}CENP-TW in bacterial cells, codon optimized cDNA of CENP-T, and -W were inserted by Gibson in a pETDuet plasmid containing a ^{6xHis-TEV}CENP-W and a ^{Halo-TEV}CENP-T (Walstein et al., 2021) to generate plasmids co-expressing the following constructs: ^{6His-TEV}CENP-W/^{MBP}CENP-T and ^{6His-TEV}CENP-W/^{mScarlet}CENP-T. The plasmids pUC18 containing 199-bp, 165-bp and 75-bp CEN1 (centromere 1) like sequences ATCGCCCTTGAGCCTTCGTTGGAACGGGATTCTTCATATTCTGCTAGACAGAAGAATTCTCAGTAACCTTCCTTGTTGTGTGTATTCAACTCACAGAGTTGAACGATCCTTTACACAGAGCAGACTTGAAACACTCTTTTTGTGGAATTTGCAGGCCTAGATTTTCAGCCGCTTTGAGGTCAATCACCCCGTGAT, GTGGTAGAATAGGAAATATCTTCTATAGAACTAGACAGAATGATTCTCAGAACTCCTTTGTGATGTGTGCGTTCAACTCAGAGTTTAACTTTCTTTTCATAGAGCAGTTAGGAAACACTCTGTTTGTAAATGTCTGCAAGTGGATATTCAGACGCCCTTG and ATCGTGGTAGAATAGGAAATATCTTCTATAGAACTAGACAGAATGATTCTCAGAACTCCTTTGTGATGGAT were generated previously (Walstein et al., 2021).

METHOD DETAILS

Generation of biotinylated DNA

Primers GTGGACACTCTAAGGATCCGG and Biotin-TEG-CCGGATCCTTAGAGTGTCCACCATC (Sigma Aldrich, St. Louis, US-MO) were dissolved in water at 200 pmol/μL, mixed in equal amount, and incubated at 95 °C for 15 min for annealing. The 165 bp DNA and the previously annealed primers were incubated with MBP-T4-DNA-Ligase (purified in house) for 17 h at 4 °C. The reaction was then stopped by incubation at 65 °C for 10 min. After centrifugation, the reaction was loaded on Anion exchange Hi Trap QFF 5mL column (Cytiva, Marlborough, US-MA) equilibrated in 10 mM Tris pH 7.4, 1 mM EDTA pH 8.0, and eluted with two successive 10 column volumes gradients (0–35% then 35 to 100%) of the same buffer implemented with 2M NaCl. The elution was analyzed on agarose gel, and the fractions containing the Biotinylated DNA were pooled and precipitated with 1/10 vol NaOAc +0.7 vol 100% 2-propanol. The pellet was washed with 70% ethanol solution and finally dissolved in 10 mM Tris pH 7.4, 1 mM EDTA, 100 mM NaCl.

Protein expression and purification

CENP-LN, -OPQR, -TWSX and -SX complexes were expressed and purified according to previously published protocols (Pentakota et al., 2017; Pesenti et al., 2018; Walstein et al., 2021). Expression and purification of CENP-C¹⁻⁵⁴⁴HIKM and CENP-HIKM were performed following a protocol adapted from (Klare et al., 2015). Tnao38 cells were infected with a virus:culture ratio of 1:50 and incubated for 72 h at 27°C. Cell pellets were harvested, washed in 1 × PBS, and finally resuspended in a buffer containing 50 mM HEPES 7.0, 500 mM NaCl, 5 mM MgCl₂, 5% glycerol, 10 mM imidazole, 2 mM TCEP, 0.2 mM PMSF, and 10 μg/mL DNase. Cells were lysed by sonication, and cleared for 1 h at 100,000g. Cleared cell lysate was then applied over a 5 mL HisTrap FF column (Cytiva) and washed first with washing buffer (50 mM HEPES 7.0, 500 mM NaCl, 5 mM MgCl₂, 5% glycerol, 10 mM imidazole, and 2 mM TCEP), secondly with high salt washing buffer (50 mM HEPES 7.0, 1 M NaCl, 5 mM MgCl₂, 5% glycerol, 10 mM imidazole, and 2 mM TCEP) followed by washing buffer again and thirdly with Imidazole washing buffer (50 mM HEPES 7.0, 500 mM NaCl, 5 mM MgCl₂, 5% glycerol, 40 mM imidazole, and 2 mM TCEP). CENP-C¹⁻⁵⁴⁴HIKM complex was eluted with elution buffer (50 mM HEPES 7.0, 500 mM NaCl, 5 mM MgCl₂, 5% glycerol, 200 mM imidazole, and 2 mM TCEP). The fractions containing CENP-C¹⁻⁵⁴⁴HIKM or CENP-HIKM were pooled, and the His tag cleaved overnight at 4°C with TEV protease (in house production). CENP-C¹⁻⁵⁴⁴HIKM or CENP-HIKM in solution was then adjusted to a salt concentration of 300 mM, before loading on a 5 mL HiTrap Heparin HP column (Cytiva), equilibrated in 20 mM HEPES pH 7.0, 300 mM NaCl, 5% glycerol, 2 mM TCEP. Bound proteins were eluted with a gradient of 300–1000 mM NaCl over 30 column volumes, and peak fractions corresponding to CENP-C¹⁻⁵⁴⁴HIKM or CENP-HIKM were pooled and concentrated in a 50 kDa MW Amicon concentrator (Millipore). CENP-C¹⁻⁵⁴⁴HIKM or CENP-HIKM were then loaded onto a Superose 6 16/600 (Cytiva) in 20 mM HEPES 7.0, 500 mM NaCl, 5% glycerol, 3 mM TCEP. The sample was concentrated and flash frozen in liquid nitrogen before use. ^{MBP}CENP-TW and ^{mScarlet}TW complexes were purified using the previously described protocol for CENP-TW wild type (Walstein et al., 2021). Preparations of CENP-A-containing nucleosomes were carried out as described (Walstein et al., 2021) modified from the previously published protocol (Guse et al., 2012).

Fluorescence labeling of recombinant proteins

CENP-SX was labeled using Alexa Fluor 647 Protein Labeling Kit (ThermoFisher Scientific, Waltham, US-MA) according to the manufacturer instructions.

Analytical SEC

Analytical size exclusion chromatography was carried out on a Superose 6 5/150 (Cytiva, Marlborough, US-MA) in a buffer containing 20 mM HEPES pH 6.8, 300 mM NaCl, 2.5% (v/v) glycerol and 1 mM TCEP on an ÄKTA micro system (Cytiva). All samples were eluted under isocratic conditions at 4 °C in SEC buffer (20 mM HEPES pH 6.8, 300 mM NaCl, 2.5% (v/v) glycerol and 1 mM TCEP) at a flow rate of 0.15 mL/min. Elution of proteins was monitored at 280, 555 and 647 nm in case of mScarlet⁺CENP-TW and CENP-SX^{Alexa647}. From 1 mL to 2.3 mL elution volume, 100 μ L fractions were collected and analyzed by SDS-PAGE and Coomassie blue staining. In experiments where fluorescently labeled proteins were used, the in-gel detection of the fluorescence was detected using a BioRAD chemiDoc MP Imaging System (BioRAD, Hercules, US-CA). To detect the formation of a complex, proteins were mixed at the concentrations of 5 μ M in 50 μ L, incubated for at least 1 h on ice, subjected to SEC then analyzed by SDS-PAGE.

Pull-down assays

The proteins were diluted with binding buffer (20 mM HEPES pH 6.8, 300 mM NaCl, 2.5% glycerol, 1 mM TCEP, and 0.01% Tween) to 3 μ M concentration in a total volume of 50 μ L, incubated at 4 °C for 1 h, and mixed with 25 μ L of amylose beads (New England Biolabs, Ipswich, US-MA) or Streptavidin Ultralink beads (ThermoFisher Scientific, Waltham, US-MA) depending of the experiment. After mixing the proteins and the beads, 20 μ L were taken as input. The rest of the solution was incubated at 4 °C for an additional 1 h on a thermomixer (Eppendorf, Hamburg, Germany) set to 1000 rpm. To separate the proteins bound to the beads from the unbound proteins, the samples were centrifuged, at 800g or 3000g for the amylose beads and the streptavidin beads respectively, for 3 min at 4 °C. The supernatant was removed, and the beads were washed four times with 500 μ L of binding buffer. After the last washing step, 20 μ L of 2 \times SDS-PAGE sample loading buffer was added to the dry beads. The samples were boiled for 5 min at 95 °C and analyzed by SDS-PAGE and Coomassie staining. Gel densitometry was carried out with Image Lab (BioRAD, Hercules, US-CA).

In vitro assembly of CCAN

Reconstitution of human recombinant CCAN particles was performed as previously published in [Pesenti et al. \(2018\)](#). In brief, a stoichiometric amount of purified CENP-LN, CENP-CHIKM, CENP-OPQUR and CENP-TWSX complexes were incubated at around 15 μ M at 4 °C for minimum 1 h and purified by SEC on S6 10/300 column (Cytiva) using a buffer containing 20 mM HEPES pH 6.8, 300 mM NaCl, 2.5% (v/v) glycerol and 1 mM TCEP.

Sample preparation for electron microscopy

The reconstituted CCAN particles were stabilized via the GraFix method ([Kastner et al., 2008](#)). Two 4-mL gradients ranging from 20 to 50% glycerol in 20 mM HEPES pH 6.8, 300 mM NaCl and 1mM TCEP were set up, in one of which the 50% glycerol solution also contained 0.125% glutaraldehyde. Around 100 μ L of sample at 15 μ M was applied to each gradient and centrifuged by ultracentrifugation at 45,000 rpm at 4 °C in SW 60 Ti Swinging-bucket rotor (Beckman Coulter, Palo Alto, US-CA) for 16 h. The samples from both gradients were fractionated in 150 μ L fractions, and cross-linker containing fractions were quenched by addition of 100 mM Tris pH 6.8. All fractions were analyzed by SDS-PAGE and Coomassie blue staining. The fractions of interest were dialyzed two times against 2 L of 20 mM HEPES pH 6.8, 300 mM NaCl, and 1mM TCEP buffer for 16 and 2 h, and concentrated to around 2 mg/mL using Amicon Ultra 0.5 mL-100 kDa cutoff (Millipore, Burlington, US-MA).

Negative stain electron microscopy

Negative stain specimens were prepared as described previously ([Brocker et al., 2012](#)): The cross-linked CCAN samples were diluted in 20 mM HEPES pH 6.8, 300 mM NaCl, and 1mM TCEP buffer to adjust the particle density. 4 μ L of the sample were absorbed at 25 °C for 1 min onto freshly glow-discharged 400 mesh carbon-coated copper grids (G2400C, Plano GmbH, Wetzlar, Germany). Excess sample was blotted by touching a Whatman filter paper and washed with three droplets of water and exposed to freshly prepared 0.75% uranyl formate solution (SPI Supplies/Structure Probe, West Chester, PA) for about 1 min. Excess negative stain solution was blotted and the specimen air-dried. Specimens were inspected with a JEM1400 microscope (Jeol, Tokyo, Japan) equipped with a LaB₆ cathode and operated at an acceleration voltage of 120 kV. Digital micrographs were recorded using a 4k x 4k CMOS camera F416 (TVIPS, Gauting, Germany).

Cryo-EM grid preparation and data acquisition

Grids were prepared using a Vitrobot Mark IV (Thermo Fisher Scientific) at 13 °C and 100% humidity. 4 μ L of CENP-16 supplemented with 0.0025% Triton were applied to glow-discharged UltrAuFoil R1.2/1.3 grids and excess liquid removed by blotting (3.5 s at blot force -3) before vitrification in liquid ethane. For dataset I, CENP-16 was used at a concentration of 1.5 mg/mL. For dataset II, CENP-14 (without CENP-SX) was used at 0.9 mg/mL. The CCAN sample used for dataset II also contained a 145-bp DNA and CENP-A:H4. Elongated DNA was visible in the micrographs, but no density for DNA or CENP-A:H4 was identifiable in any of the reconstructions. Dataset I was acquired on a Titan Krios electron microscope (Thermo Fisher Scientific) equipped with a field emission gun. For this

first dataset, 1540 movies were recorded on a K3 camera (Gatan) operated in super-resolution mode at a nominal magnification of 130,000, resulting in a super-resolution pixel size of 0.35 Å. A Bioquantum post-column energy filter (Gatan) was used for zero-loss filtration with an energy width of 20 eV. Total electron exposure of $76.8 \text{ e}^-/\text{Å}^2$ was distributed over 80 frames. Data were collected using the automated data collection software EPU (Thermo Fisher Scientific), with two exposures per hole and a set defocus range of -0.6 to $-1.2 \text{ }\mu\text{m}$. The second dataset was recorded on a Cs-corrected Titan Krios microscope equipped with a K3 camera (Gatan) and a Bioquantum post-column energy filter with a slit width of 14 eV operated in super-resolution mode at a nominal magnification of 105,000, corresponding to a super-resolution pixel size of 0.34 Å. A total exposure of $55.8 \text{ e}^-/\text{Å}^2$ was distributed over 60 frames. 2678 movies were collected using EPU (Thermo Fisher Scientific), with two exposures per hole and a set defocus range of -0.6 to $-1.2 \text{ }\mu\text{m}$. For both datasets, phase contrast was induced by using a volta phase plate in the back focal plane. Details of data acquisition parameters can be found in [Table S1](#).

Cryo-EM data processing

On-the-fly data pre-processing, including correction of beam-induced motion and dose-weighting by MotionCor2 (Zheng et al., 2017), CTF parameter estimation using CTFFIND4 in movie mode (Rohou and Grigorieff, 2015), and particle picking using a custom neural network in SPHIRE-crYOLO (Wagner et al., 2019), was performed within TranSPHIRE (Stabrin et al., 2020). For the high-resolution dataset (dataset I in [Figure S3](#)), template-free particle picking by crYOLO (Wagner et al., 2019) in the 1540 micrographs greatly improved after re-training with 1354 manually picked particles, resulting in 140,910 particle coordinates. 2-fold binned particles were extracted in SPHIRE (Moriya et al., 2017) using a box size of 220x220 pixels. 2D classification was performed in ISAC with a class size limit of 500 particles, a particle radius of 105 pixels and using the VPP option. 45 beautified 2D class averages which had been filtered to 8 Å were used to generate an initial 3D model in RVIPER. In parallel, the dataset was processed in RELION 3.1.2 (Fernandez-Leiro and Scheres, 2017; Nakane et al., 2018) using a box size of 384x384 pixels for extraction and 200 classes for 2D classification and initial model generation. The 95,522 selected particles and the resulting initial model could be refined both in MERIDIEN and RELION, yielding a 7 Å reconstruction. The centered particles were then re-extracted without binning and using a box size of 384 pixels, and all further processing steps were performed in RELION. 3D classification with four classes yielded one class with 25,206 particles which showed high-resolution features in the center of the particle. The quality of the reconstruction was improved by Bayesian polishing, resulting in an increased global resolution of 5 Å.

This reconstruction was further improved by multi-body refinement in RELION using two masks covering the majority of the HIKMLN or OPQR subcomplexes, i.e. omitting the more flexible QU- and HIK head and TW, resulting in focused reconstructions with resolutions of 4.6 Å for HIKMLN and 6.9 Å for OPQR. Segmenting the volumes further (including e.g. additional maps for the "heads") did not improve the quality of the reconstructions. The multi-body refinement was especially important for improvement of the resolution of the OPQR part. As evident from local resolution estimation with RELION, the quality of the reconstruction varies greatly between the well-ordered CENP-M/L/N interface with local resolution of 3.7 Å, and more peripheral parts which are more flexible and less well resolved. The angular distribution showed that the particles had a moderate fraction of preferred orientations along the shortest axis of the particles ([Figure S3B](#)). DeepEMhancer (Sanchez-Garcia et al., 2021) was used to further enhance the maps for model building.

The second dataset (dataset II in [Figure S4](#)) had lower resolution although the initial 2678 micrographs yielded more particles compared to the first dataset (233,598 vs 140,910) when picked with the re-trained crYOLO model. DNA strands were visible in the micrographs, but no nucleosomes (no H2A:H2B was present). For extraction, a larger box size of 512 pixels (corresponding to 358.4 Å) was chosen to potentially detect more different conformations compared to the first dataset. Particles were subjected to 2D classification in RELION, and an initial model was calculated, also in RELION, using 117,473 particles assigned to good 2D classes. Subsequent 3D classification into four classes yielded one class (with 44,216 assigned particles) suitable for 3D refinement. The quality of the refined model could not be improved by further 2D classification, Bayesian polishing, or CTF refinement. Although the overall resolution was lower, this dataset showed much clearer density for the HIK and QU heads, including a tentative density for the CENP-TW complex that fits very well to the position of TW in the X-ray structure of the HIK-TW complex (PDB: 6WUC). This assignment is corroborated by AlphaFold2 predictions that indicate a strong interaction between the HIK head and TW as compared to the CENPA/H4 dimer (I.R.V, unpublished data). RELION multi-body refinement with three masks covering HIKTW, MLN, and OPQR, respectively, resulted in resolutions of 10.2 Å, 10.2 Å and 10.6 Å for the three maps. Local resolution estimated with RELION ranged between 8 and 25 Å ([Figure S4D](#)). The angular distribution showed no pronounced preferred orientations ([Figure S4B](#)). Since crYOLO picked practically all particles and the 2D/3D classes did not show any evidence for the presence of DNA or nucleosomes, any stable association of DNA or CENP-A/H4 with the CCAN can be excluded.

Model building and structure refinement

Crystal structures of human CENP-M (PDB: 4WAU), human CENP-N (PDB: 6EQT) as well as *ab initio* models for human CENP-H, K, I, L, N, O, P, Q, U, R, T, and W predicted by the Tencent tFold server (<https://drug.ai.tencent.com>) were initially docked as rigid bodies into the reconstruction of dataset I sharpened by DeepEMhancer and then locally adjusted using Coot (Emsley et al., 2010), Chimera (Pettersen et al., 2004, 2021; Pintilie and Chiu, 2012; Yang et al., 2012), and Namdinator (Kidmose et al., 2019). The cryo-EM structures of the yeast CCAN (PDB:s 6QLD and 6QLE) and the yeast CTF3 complex with CNN1-WIP1 (PDB: 6WUC) were also used to guide the modeling. Secondary structures for the yeast proteins were assigned by DSSP (Kabsch and Sander, 1983) and structural

alignments generated (Figures S6–S9). Subsequently, *ab initio* models predicted using AlphaFold2 were used to further improve the structure model. These Alpha-fold models ("Colab-fold", AF2, and AF2-multimer (Evans et al., 2021; Jumper et al., 2021; Mirdita et al., 2021) greatly facilitated the sequence assignment in regions with lower local resolution. Density for a short helix at the interface of CENP-I and CENP-K was built as a polyalanine model since the sequence could not be assigned reliably. Possible assignments include CENP-C, the N terminus of CENP-H, CENP-P or CENP-O, the latter slightly more likely since AF2-multimer predicted this interaction with medium confidence (Figure S5E). In contrast, the extension of the CENP-N β -sheet by the CENP-C region 303-FIID-306 was reliably predicted by AF2-multimer (Figure S5D) and allowed unambiguous interpretation of the corresponding short stretch of electron density for CENP-C. The position of the CENP-TW complex was derived by superposing an AF2-prediction of the CENP-HIK head in complex with CENP-TW (which had exactly the same arrangement as the model of the yeast CTF3-CNN1-WIP1 complex (PDB: 6WUC)) and subsequently docking it into the reconstruction of dataset II. The final model was optimized by geometry minimization and real-space refinement with PHENIX (Adams et al., 2010) and evaluated with COOT, PHENIX and MolProbity (Chen et al., 2010). Figures were prepared using Chimera and PyMOL (Molecular Graphics System, 2.0.3, Schrodinger). Structural sequence alignments were performed with Chimera.

Cell culture and immunofluorescence

For immunofluorescence experiments with HeLa Flip-In T-Rex EGFP-CENP-M (Basilico et al., 2014), cells were grown on coverslips pre-coated with 0.01% poly-D-lysine (Sigma-Aldrich). Exogenous gene expression was induced by adding 50 ng/mL doxycycline (Sigma, St. Louis, Missouri, United States) to the media for 24h before fixation. Cells were fixed with ice-cold Methanol for 1 min, then washed 3 times for 5 min with one X PBS +0.1% Tween 20 (PBST). Cells were blocked for 20 min at room temperature in PBST +5% BSA, and then were incubated in primary antibodies diluted in PBST +1% BSA overnight at 4C. The following morning, coverslips were washed 3 times for 5 min with PBST and then incubated for 30 min at room temperature with secondary antibodies diluted in PBST +1% BSA. Finally, coverslips were washed 3 times for 5 min in PBST and quickly rinsed in distilled water before mounting. The following primary antibodies were used: anti-CyclinB1 (rabbit monoclonal antibody, Abcam, #ab32053, 1:1000), CREST/anti-centromere antibody (human autoimmune serum, Antibodies Inc., #15–234, 1:1000), anti-PCNA (mouse monoclonal antibody, Cell Signaling, #2586S, 1:1000), anti-Tubulin (rat monoclonal antibody, Abcam, #6160, 1:500). The following secondary antibodies were used: donkey anti-human DyLight 405 (Jackson ImmunoResearch, 1:000), donkey anti-mouse Alexa Fluor 647 (Invitrogen, 1:1000), donkey anti-rabbit Rhodamine Red (Jackson ImmunoResearch, 1:000), donkey anti-rat Rhodamine Red (Jackson ImmunoResearch, 1:000), GFP-Booster Alexa Fluor 488 (Chromotek, gb2AF488-50, 1:1000), goat anti-human Alexa Fluor 647 (Jackson ImmunoResearch, 1:000). DNA was stained with 0.5 μ g/mL DAPI (Serva) and Mowiol (Calbiochem) was used as mounting media.

To induce rapid depletion of the endogenous CENP-C and CENP-A in AI-tagged lines, 500 μ M of the synthetic auxin indole acetic acid (IAA, Merck #I5148-2G) was added to the cells for 8 h. The engineered DLD-1 cells were cultured in Dulbecco's modified Eagle's medium (DMEM; PAN-Biotech) supplemented with 10% tetracycline-free fetal bovine serum (Thermo Fisher Scientific), 2 mM penicillin/streptomycin (PAN-Biotech), and 2 mM L-glutamine (PAN-Biotech) at 37 °C in a 5% CO₂ atmosphere. Paraformaldehyde (PFA)-fixed cells (10 min) were permeabilized with PBS-T [PBS (PBS) buffer containing 0.1% Triton X-100] for 10 min and incubated with PBS-T containing 4% BSA for 40 min. Cells were incubated for 90 min at room temperature with CREST/anti-centromere antibody (Antibodies Inc. # #9101-02; dilution 1:200), CENP-A antibody (GeneTex #GTX13939; dilution 1:1000), CENP-HK antibody (SI0930, produced in-house; dilution 1:500) and CENP-T antibody (SI0822, produced in-house; dilution 1:500), washed three times with PBS-T, and were subsequently treated for 30 min with anti-human DyLight 405-conjugated secondary antibody (Jackson ImmunoResearch # 709-475-149; dilution 1:200), anti-mouse Rhodamine Red-conjugated secondary antibody (Jackson ImmunoResearch # 115-295-003; dilution 1:200) and anti-rabbit Alexa Fluor 647-conjugated secondary antibody (Jackson ImmunoResearch; dilution 1:200). Unbound secondary antibody was removed by washing three times with PBS-T and one time with double-distilled water. After drying, the coverslips were mounted with Mowiol mounting media (EMD Millipore) on glass slides and imaged using a 60x oil immersion objective lens on a DeltaVision deconvolution microscope. The DeltaVision Elite System (GE Healthcare, UK) is equipped with an IX71 inverted microscope (Olympus, Japan), a PLAPON \times 60/1.42 numerical aperture objective (Olympus) and a pco.edge sCMOS camera (PCO-TECH Inc., USA).

QUANTIFICATION AND STATISTICAL ANALYSIS

Quantification of centromere signals

Quantification of centromere signals was performed using the software Fiji with a script for semiautomated processing (Bodor et al., 2012; Pan et al., 2017). Briefly, average projections were made from z-stacks (16 layers, 3.2 μ m in total thickness) of recorded images. Centromere spots were chosen on the basis of the parameters of shape, size, and intensity using the images of the reference channel obtained with CREST staining, and their positions were recorded. In the images of the data channels (CENP-C, CENP-A, CENP-HK, CENP-T), the mean intensity value of adjacent pixels of a centromere spot was subtracted as background intensity from the mean intensity value of the centromere spot. Negative fluorescence intensities were set to 0, and the top and bottom 5% of fluorescence intensities of each data channel were excluded to remove outliers. The individual centromere intensity values were plotted using GraphPad software. Quantifications in Figure 6 and Figure S15 indicate fluorescence intensities for the indicated number of individual kinetochores and cells, and SD of quantified centromere foci (see legends for these figures).

Quantification of SDS-PAGEs

After Coomassie staining, SDS-PAGE gels were imaged with Biorad ChemiDoc MP (Bio-Rad). Band intensities of the indicated subunits or group of subunits (when co-migrating) were quantified using ImageLab software (Bio-Rad) and normalized to their intensity in absence of DNA (Figure 3A) or CCAN only sample (Figure 5H). The quantification reflects three technical replicates (included in Mendeleev dataset). Error bars indicate SD as indicated in the corresponding figure legends. Calculations were performed using Microsoft Excel (Microsoft Corporation) and illustrated using GraphPad Prism (GraphPad Software Inc).

Molecular Cell, Volume 82

Supplemental information

Structure of the human inner kinetochore

CCAN complex and its significance

for human centromere organization

Marion E. Pesenti, Tobias Raisch, Duccio Conti, Kai Walstein, Ingrid Hoffmann, Dorothee Vogt, Daniel Prumbaum, Ingrid R. Vetter, Stefan Raunser, and Andrea Musacchio

Molecular Cell, Volume

Supplemental information

Structure of the human inner kinetochore CCAN complex and its significance for human centromere organization

Marion E. Pesenti, Tobias Raisch, Duccio Conti, Kai Walstein, Ingrid Hoffmann, Dorothee Vogt, Daniel Prumbaum, Ingrid R. Vetter, Stefan Raunser & Andrea Musacchio

Table S1 (related to Figure 1)**Cryo-EM data collection, refinement and validation statistics**

	CCAN Krios2 EMDB-14098 PDB 7QOO ("dataset I")	CCAN Krios1 EMDB-14099 ("dataset II")
Data collection and processing		
Magnification	130000x	105000x
Voltage (kV)	300	300
Electron exposure (e-/Å ²)	76.8	55.8
Defocus range (µm)	-0.6 to -1.2	-0.6 to -1.2
Pixel size (native/super-resolution) (Å)	0.7/0.35	0.68/0.34
Symmetry imposed	C1	C1
Initial particle images (no.)	140910	233598
Final particle images (no.)	22853	44216
Map resolution (Å)	4.6	10
FSC threshold	0.143	0.143
Refinement		
Initial model used:	AlphaFold,6EQT,4WAU,6WUC, 6QLD, 6QLE	
Model resolution (Å)	3.8	
FSC threshold	0.143	
Model composition		
Non-hydrogen atoms	24952	
Protein residues	3086	
B-factors (Å ²)		
Protein	47.8	
R.m.s. deviations		
Bond length (Å)	0.0035	
Bond angles (°)	0.84	
Validation		
MolProbity score	1.61	
Clashscore	5.14	
Poor rotamers (%)	1.53	
Ramachandran plot		
Favored (%)	96.8	
Allowed (%)	3.13	
Disallowed (%)	0.07	

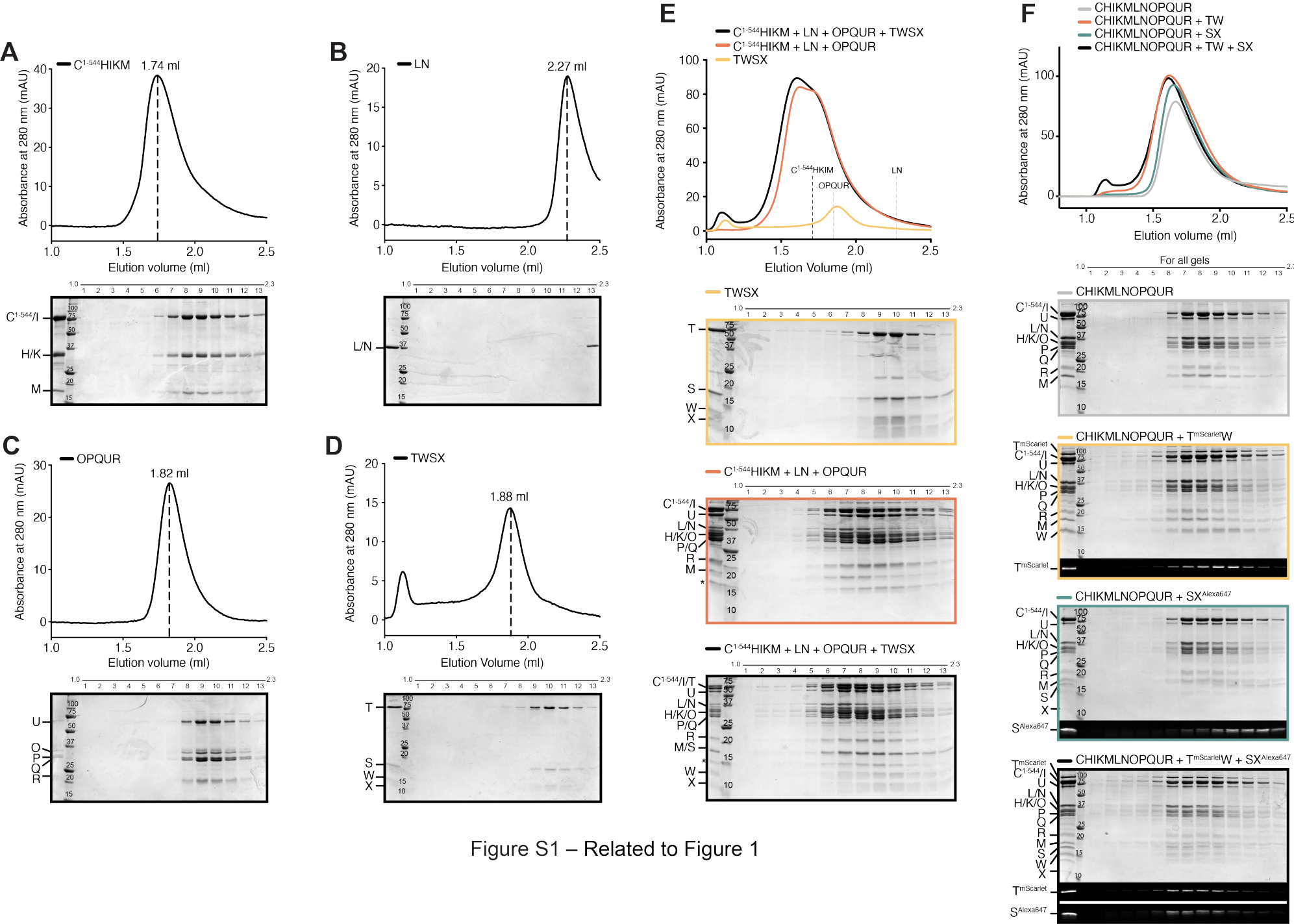


Figure S1 – Related to Figure 1

Figure S1 (related to Figure 1). Biochemical reconstitution of human CCAN

Size-exclusion chromatography on a Superose 6 5/150 column of the indicated CCAN complexes and subcomplexes. **A)** CENP-C¹⁻⁵⁴⁴HIKM. **B)** CENP-LN. **C)** CENP-OPQUR. **D)** CENP-TWSX. **E)** Comparison of elution profiles of CENP-TWSX, CENP-12, and CENP-16. **F)** CENP-TW binds CENP-12, but CENP-SX requires CENP-TW to interact with CENP-12. Gels and chromatograms in panels A-D also appear in Figure S2 (representative gels). Gels and chromatograms in panels A-C also appear as controls in [Figure S12B-D](#).

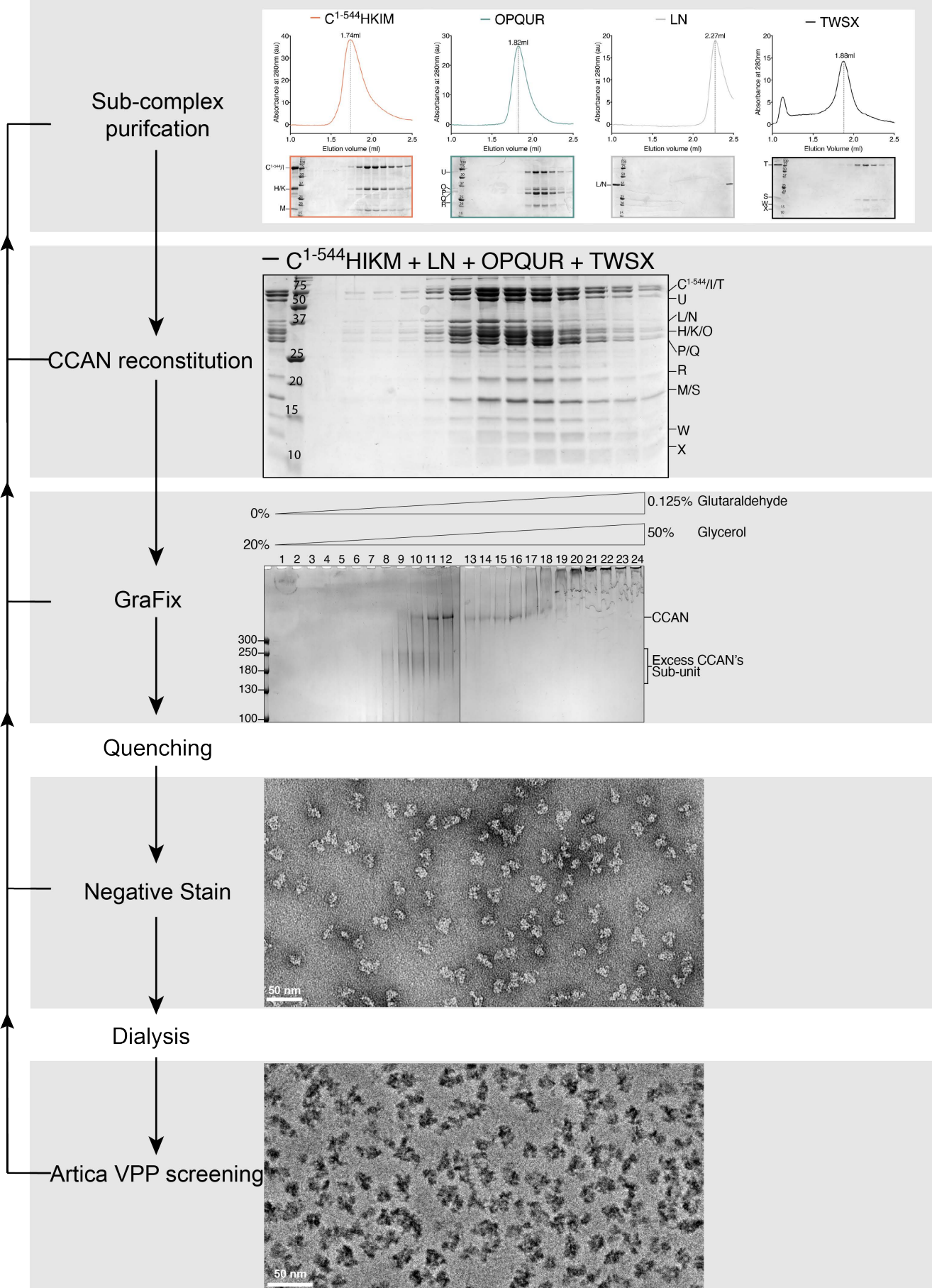


Figure S2 – Related to Figure 1

Figure S2 (related to Figure 1). Pipeline of sample preparation

The figure presents an outline of the various steps of sample preparation preceding high-resolution cryo-EM data collection. Chromatograms and gels in the upper panel are also displayed in [Figure S1](#).

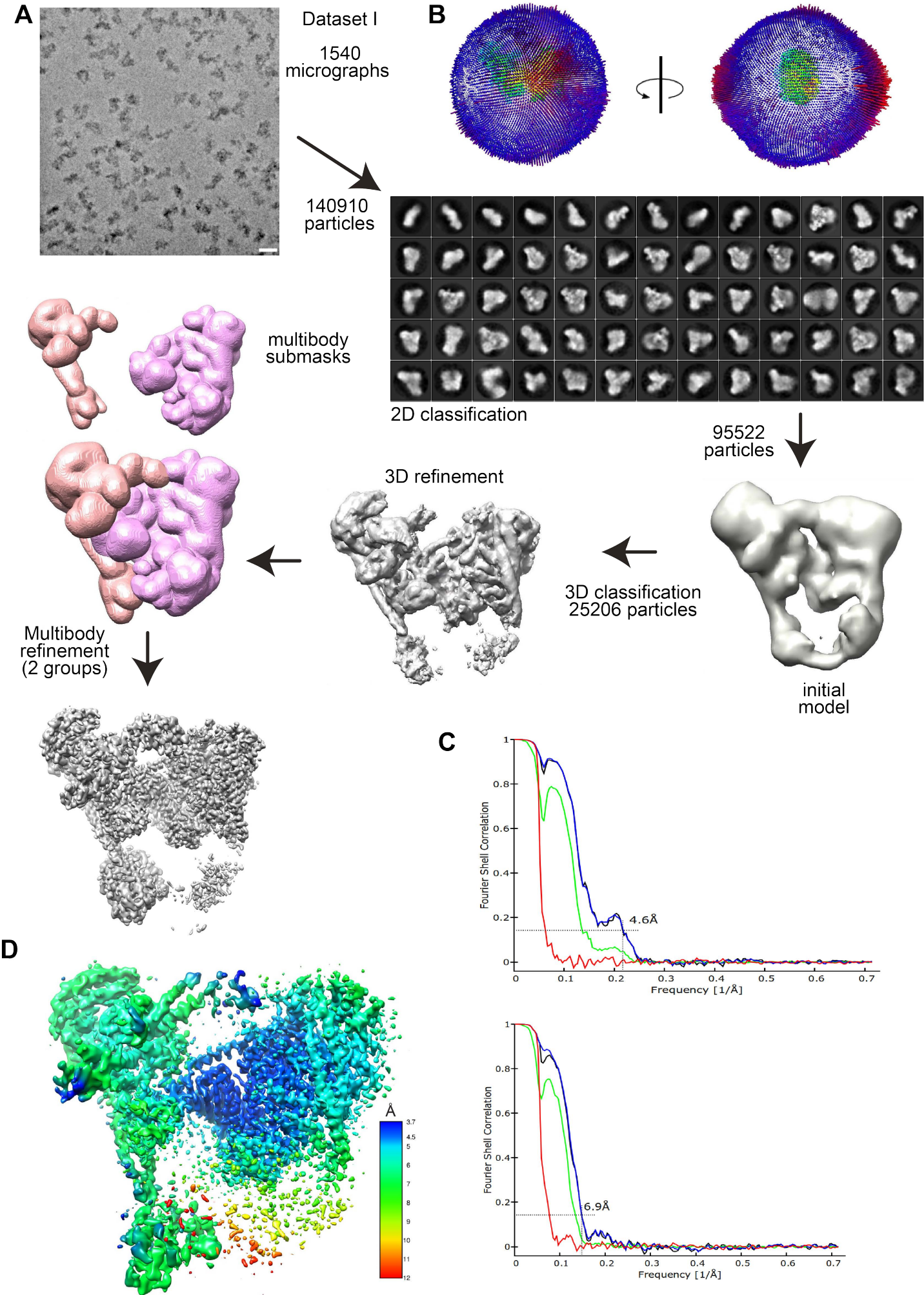


Figure S3 – Related to Figure 1

Figure S3 (related to Figure 1). Data processing flowchart for Dataset I

A) Processing flowchart for the high-resolution dataset I including an exemplary micrograph (scale bar = 20 nm) and a subset of selected 2D classes of CENP-16. The last (grey) map shows the final reconstruction and was obtained by combining the two focused maps from multibody refinement (using the 'vop maximum' command in UCSF Chimera).

B) Angular distribution of the particles shown in two positions rotated 90° to each other.

C) Fourier shell correlation (FSC) plots between two independent half-maps for each of the two bodies used in the multibody refinement procedure, according to the FSC=0.143 criterion. The dashed line indicates the 0.143 FSC criterion. red: phase-randomized map, green: unmasked map, blue: masked map, black: corrected map.

D) Local resolution estimates by RELION for dataset I plotted on the two multibody reconstructions in a rainbow-colored gradient from blue (3.7 Å) to red (12 Å). The map differs from the final reconstruction depicted in panel A since the latter shows the combined sub-maps, further modified by DeepEMhancer.

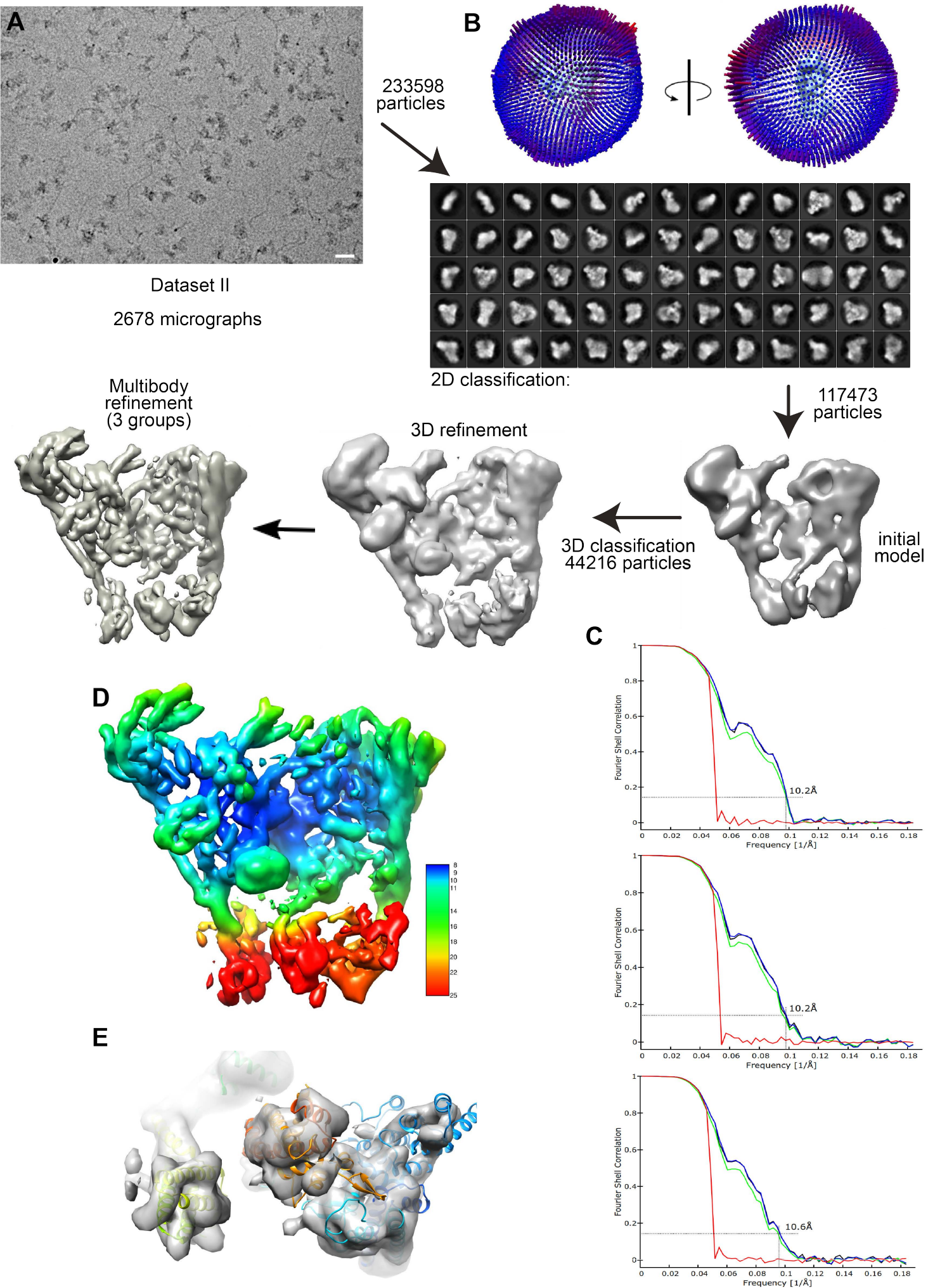


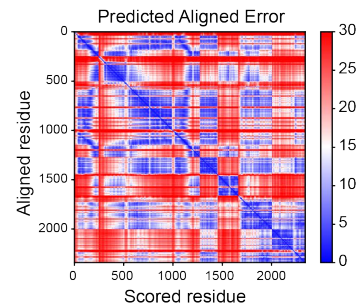
Figure S4 – Related to Figure 1

Figure S4 (related to Figure 1). Data processing flowchart for Dataset II

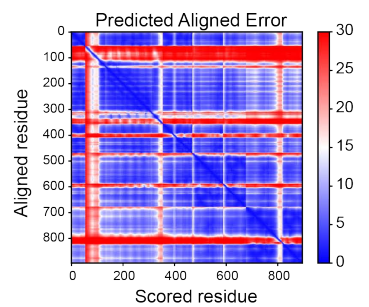
A) Processing flowchart for the low-resolution dataset II including an exemplary micrograph and a subset of selected 2D classes of CENP-14. **B)** Angular distribution of the particles shown in two positions rotated 90° to each other. **C)** Fourier shell correlation (FSC) plots between two independent half-maps for each of the three bodies used in the last multibody-refinement, indicating the resolution of the three groups in the multibody refinement according to the FSC=0.143 criterion. The dashed line indicates the 0.143 FSC criterion. red: phase-randomized map, green: unmasked map, blue: masked map, black: corrected map. **D)** Local resolution estimates by RELION plotted on the multibody reconstructions in a rainbow-colored gradient from blue (8 Å) to red (25 Å). **E)** Representative density of CENP-QU head (left), the CENP-TW complex (middle) and the HIK head (right), as seen from the "bottom" towards the top of the CCAN complex in D).

A

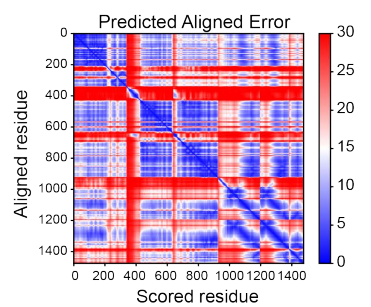
HIKM + TW + LN			
Chain	Residue	Cumulative	
H	1 247	1 247	
I	1 756	248 1003	
K	1 269	1004 1272	
M	1 180	1273 1452	
T	443 561	1453 1571	
W	1 88	1572 1659	
L	1 344	1660 2003	
N	1 339	2004 2342	

**B**

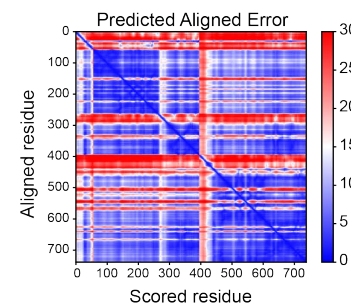
HIK head + TWSX			
Chain	Residue	Cumulative	
H	193 247	1 55	
I	1 300	56 355	
K	155 269	356 470	
T	443 561	471 589	
W	1 88	590 677	
S	1 138	678 815	
X	1 81	816 896	

**C**

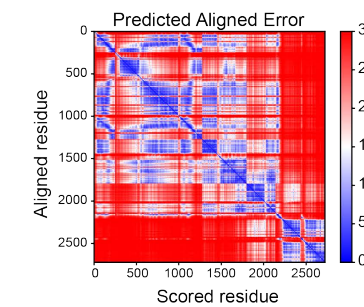
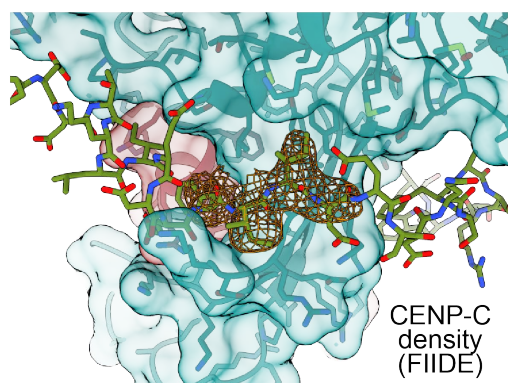
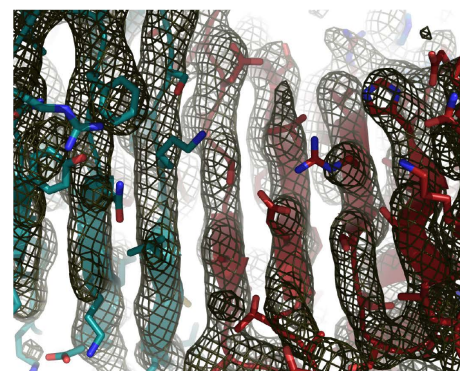
N + OPQU			
Chain	Residue	Cumulative	
N	1 339	1 339	
O	1 300	340 639	
P	1 288	640 927	
Q	1 268	928 1195	
U	232 418	1196 1382	
R	66 159	1383 1476	

**D**

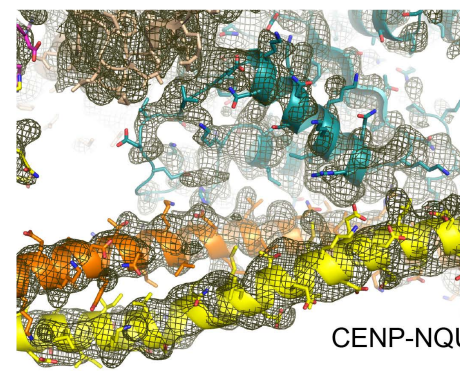
C ²⁷⁵⁻³³⁰ + NL			
Chain	Residue	Cumulative	
C	275 330	1 55	
N	1 339	56 394	
L	1 344	395 739	

**E**

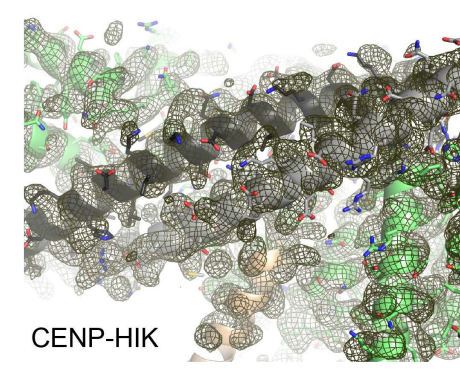
HIKM + LN + OP			
Chain	Residue	Cumulative	
H	1 247	1 247	
I	1 756	248 1003	
K	1 269	1004 1272	
M	1 180	1273 1452	
L	1 344	1453 1796	
N	1 339	1797 2135	
O	1 300	2136 2435	
P	1 288	2436 2723	

**F****G**

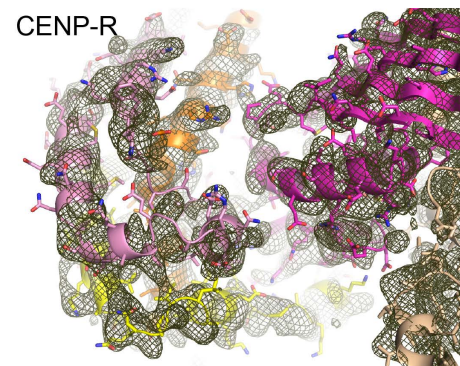
CENP-LN



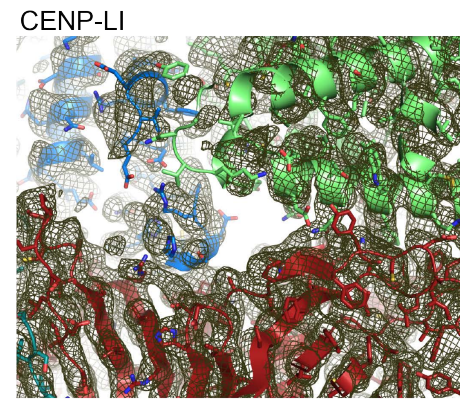
CENP-NQU



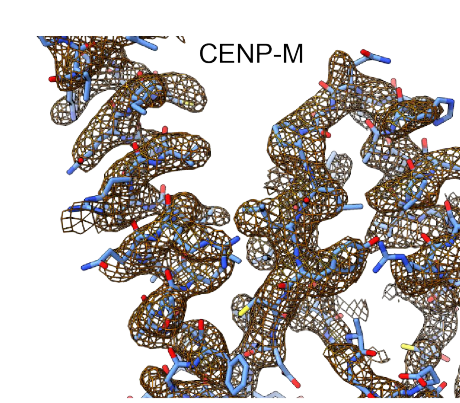
CENP-HIK



CENP-R



CENP-LI



CENP-M

Figure S5 – Related to Figure 1

Figure S5 (related to Figure 1). AlphaFold2 model quality and close-ups of density maps

A-E) Predicted aligned error (PAE) plots for AF2 models of the indicated CCAN sub-complexes. Blue color indicates low error and high confidence of the relative positioning of the subdomains, red low confidence. **F)** Density for CENP-C 303-FIID-306 bound to CENP-N. The sequence assignment of CENP-C into this short stretch of density was based on a highly significant AF2 prediction for this interaction. **G)** Representative ap densities at the indicated subunits.

CENP-H

CENP-H yeast secstruc
CENP-H human secstruc
CENP-H human
CENP-H yeast
consensus
conservation score

```
1  - - - - - DRMTL L R L R A O T K Q L L E Y K S M Y D A S E E K T P E Q I M Q E K Q I E A K I E D L P N E I E E V K V A F E I K K L A L D R M L S T A L K K N L E K I S R Q S S V L M D N M K H L L E N K L I M K S Q Q E S W D E 114  
1  M T N S S E K O W E R I L Q L L E K E H V E V Y R L L I T D R L Y L I R K H N - - - - H A V I L S H T O R L L E I R H O L Q I N L E K T A L L I R L L E K P D N T N V - - - L F K L Q N L L E E S N S L D Y E L L Q S L G A Q S S L H 111  
mt n s s e d R m t l l r l r l r a o t k q l l e y k s m y d a s e e k t p e q i m q e k q i e a k i e d l e n e i e e v k v a f e i k k l a l d r m l s t a i k k n l e k i s r q s s v l m d n m k h l l e n k l i m k s q q e s w d l e  
- - 5.4 4.6 6.8 8.8 6.5 - 7.8 * 8.5 8.6 5.8 6.7 5 * 7.6 5 8.9 * 4.5 6.5 6.6 4.6 9 - - - - 6.7 4.7 6.5 6.7 7.7 8.5 + * 5.4 9.6 7.7 5.6 6.7 6.8 7.4 5.9 * * 5.6 5.6 6.6 9.6 4 - - - - 7.5 8.5 * 8.8 6.9 7.6 5.6 6 * 8.7 5 + 9.7 * 7.6 4.8 6.7 * 6
```

CENP-H yeast secstruc
CENP-H human secstruc
CENP-H human
CENP-H yeast
consensus
conservation score

```
115 E K L L D I R K K R I Q L K g a s e s k l l E i g t e k n k q k i d l d s m e n s e r i k i i r q n l q m e i k i t t v i q h v f g n l i l g s k v n w a e d p a l k e i v l q l e k n v d m m 210  
112 K O L T I E S R A E D E L M S K L I E L S S E F P K P T I P P D - - - - - D S D T A G K Q V E V E K E N E T I C E L M I A L O T H S G Y T N I S Y T I - - - - - 181  
E K L L D I r k k r i q l k g a s e s k l l e i g t e k n k q k i d l d s m e n s e r i k i i r q n l q m e i k i t t v i q h v f g n l i l g s k v n w a e d p a l k e i v l q l e k n v d m m  
7.7 * + 9.5 * 5.7 * 4.8 * 7.8 5 5 5 6 6 5 5 7.8 * 7.7 5 7.6 4.7 6 - - - - - 4.5 4.7 4.6 6.7 6.6 4.5 * 5.9 6.8 * * 6.9 9.7 7 * 7 * 4 * 5.6 9.7 7.6 5.7 - - - - -
```

CENP-I

CENP-I yeast secstruc
CENP-I human secstruc
CENP-I human
CENP-I yeast
consensus
conservation score

```
1  V G D Y E H A D D Q A E E D A L Q M A V G Y F E K G P I X A S Q N K D K T L E K H L K T V E N V A W K N G L A S E E D I L L N I A L S G K F G N A V N T R I L K C M I P A T V I S L S V V K A V S W L C V G K C - - - - - S G S T 110  
1  - - - - - M S L I L D D I L S L T N A N E - - - - T P Q A L K T T L S L Y E K S Q Y K G L S P L Q A L V R L L C E T S I D T V T K V Y I L E N C I P A D G Y L T S K E L L E I N H L G P T V F S R Y R I Q T P S V L 106  
v g d y e h a d d q a e e d a l q m a v g y f e k g p i x a s q n k d k t l e k h l k t v e n v a w k n g l a s e e d i l l n i a l s g k f g n a v n t r i l k c m i p a t v i s l s v v k a v s w l c v g k c f s r y r i q t p s v l  
- - - - - 6.6 4.7 * 7.5 7.9 7.6 8.8 6.6 * 8.5 9 - - - - 9.4 6.7 8 * 7.7 6 * 5.7 9.6 7.5 8.7 7.7 * * 8 * 5.8 + 7.7 * 9.7 + 7.8 6.8 5.5 8.5 9.8 8.8 6.6 * 9.7 8.9 8.6 7.5 8.6 + 8.7 9.5 9.9 7.7 9.9 8 * 9.8 7.7 9.7 4.8 8.8 5.6 6.7 7.6 7
```

CENP-I yeast secstruc
CENP-I human secstruc
CENP-I human
CENP-I yeast
consensus
conservation score

```
111 K V L F Y R W L V A M F D F I D - - R K E G I N L Y G F F F A S L Q D D A L C P Y V C H L L Y I L T K K E N - V P F R Y R K L D L Q A K M G M - - - O P H L O A L I S L Y K F F A P A L I S V S L P V R K K I Y F N E N L W K R T A L L 224  
107 Q S A L C R W L V H V Y L F P V H S E R E H N I S S S I W L H L W G F S F L Q K W I T P L V I W Q A T T P V D - - - S I Y P L R L Q S L P E Y V P S D S T V S L W D V S I Q L A Q N W P Q L H T P N D V D Y M M K P S L N S N V L L P R K V M S R D S L K H L Y S S 226  
K v l f y r w l v a m f d f i d - - r k e g i n l y g f f f a s l q d d a l c p y v c h l l y i l t k k e n v p f r y r k l d l q a k m g m - - - o p h l o a l i s l y k f f a p a l i s v s l p v r k k i y f n e n l w k r t a l l  
7.6 7.8 7.9 * * 4.8 9.4 8.8 6.4 + 6.7 8.8 5 * + 5.6 6.8 9.8 4.5 7 * 4.7 7 * 7.4 + 9.9 8 * 9.7 7.8 7.7 5.7 5 * * 9.9 9.6 6 + 6.7 8.6 8.9 7 * 8.8 5.4 7.7 4.7 8 * 7 * 8.5 9.7 8.8 8.7 * 5.5 8.9 8.5 7.9 5.7 6.6 7.6 9.6 8.5 6.5 8.9 9.7 6 *
```

CENP-I yeast secstruc
CENP-I human secstruc
CENP-I human
CENP-I yeast
consensus
conservation score

```
225 A V K Q R N R G P S P E P L K L M L G P A N V R P L R K R W N S L S V I P V L N S S S Y T K E C G K K E M S L S D C L N R S G S F P L E Q L Q S F P Q L L Q N I H C L E I P S Q M G S V L N N - - - - - S L L L H 324  
227 D A H F L S I L K R L S R A H P A N F P A D T V Q N T I D M Y L S E I H Q L G A D - - - S I Y P L R L Q S L P E Y V P S D S T V S L W D V S I Q L A Q N W P Q L H T P N D V D Y M M K P S L N S N V L L P R K V M S R D S L K H L Y S S 342  
a v k q r n r g p s p e p l k l m l g p a n v r p l r k r w n s l s v i p v l n s s s y t k e c g k k e m s l s d c l n r s g s f p l e q l q s f p q l l q n i h c l e i p s q m g s v l n n - - - - - s l l l h  
a v k q r n r g p s p e p l k l m l g p a n v r p l r k r w n s l s v i p v l n s s s y t k e c g k k e m s l s d c l n r s g s f p l e q l q s f p q l l q n i h c l e i p s q m g s v l n n s n v l l p r k v m s r d s l k h l y s s  
6.8 9.7 5.9 5.7 4.6 6.5 7.5 5.5 7.7 7.5 7.5 6.7 7.6 6.6 6.5 7.8 * * 4 * 3.6 * 7.8 7 - - - - 6.8 6.4 6.8 9.8 5.5 6.5 7.5 * 5.1 * 7.7 5.5 4.8 8.5 6.8 7.1 * 6.9 6.8 8.7 5.5 6.7 9.5 8.7 6.9 7.8
```

CENP-I yeast secstruc
CENP-I human secstruc
CENP-I human
CENP-I yeast
consensus
conservation score

```
325 Y I N C V R D E P V L L R P Y W L S Q T I Q E E C I W Y K V N N Y E H G K E F T N F L D T I I R A E C F L Q E G F Y S C E A F L Y K S L P L W D G L U C O R S Q F L Q L V S W I P P S S F S E V K P L L F D H L A Q L F F T - - - - - T I Y 438  
343 I L L I K N S R D E S S P Y W L S Q T I Q E E C I W Y K V N N Y E H G K E F T N F L D T I I R A E C F L Q E G F Y S C E A F L Y K S L P L W D G L U C O R S Q F L Q L V S W I P P S S F S E V K P L L F D H L A Q L F F T - - - - - T I Y 456  
y i n c v r d e p v l l r p y w l s q t i q e e c i w y k v n n y e h g k e f t n f l d t i i r a e c f l q e g f y s c e a f l y k s l p l w d g l u c o r s q f l q l v s w i p p s s f s e v k p l l f d h l a q l f f t - - - - - t i y  
7.1 6.8 5.7 7.8 6.4 5.5 6.6 * 6 * 8.5 8.8 * 7.8 5.6 7.8 8 - - - 6.6 6.3 6.7 4.8 7.6 8 + 7.8 5.5 6.6 7.6 - - - 5.8 5.6 3.8 8.8 * 8.7 6.5 7.6 6.7 * 4 * 9.8 9.5 6.8 7.6 + 9.7 7.4 6.6 6.5 8 * 4.8 9.5 8.8 7.6 7.9 * 8 * + 9.8 * 6.8 5.4 + 5.9 6.7
```

CENP-I yeast secstruc
CENP-I human secstruc
CENP-I human
CENP-I yeast
consensus
conservation score

```
439 F K C S V I Q S K E L L Q N W L W L S M D I H M K P V T N S P L E T T L G G S M N S V K L I H Y V G W L S T A M R I E - - S N T F L L H F I L D F Y E K V C D I Y I N Y - - N L P L V L F P P G I F Y S A L S L D T S I L N Q I 553  
457 T F S E T C F Y L A M I T N W L D D K - - - - - L I A L G L L H D M Q S L L L D K I F E N A I S N R E S T M A E I L S S L I I T Q S K Q T K S D Y A I Q Y L I V G P D I M N K V F S S D P L L L S A I 557  
f k c s v i q s k e l l q n w l w l s m d i h m k p v t n s p l e t t l g g s m n s v k l i h y v g w l s t a m r i e - - s n t f l l h f i l d f y e k v c d i y i n y - - n l p l v l f p p g i f y s a l s l d t s i l n q i  
7.6 7.6 8.8 8.7 6.9 6.8 9 + 8 * * 9 * 5.4 5 - - - - - 5.9 7.5 8.5 7 * + * 5.8 6.6 * 5 * 7.5 7.5 8.7 5.4 8.9 * 6 * 5.7 6.7 8 + 7.5 7.9 6.9 9.7 - 6.9 7.9 7.4 5.7 7.6 7.6 9 - 7.7 * 5 * 9.7 5.8 8.8 * 4 * 7.5 + * 9.6 7
```

CENP-I yeast secstruc
CENP-I human secstruc
CENP-I human
CENP-I yeast
consensus
conservation score

```
554 C F I M H R Y R K N L T A A K K N E L V Q K T K S E F N F S S I T Y Q E F N H Y L T S M V G C L W T S K P F G K G - - - - - I Y I D P E I L E K T G V A E Y K - - - - - N S I N V V H H P S F L S Y A V S F L L Q E S P - - - - - E E R I V N 657  
558 C R Y L V A T R N K L M Q P A S T - - - - - N F V R M Q N Q Y I M D L T N Y L R N K V L S S K S L F G V S P D F F K O I N L Y I P T A D F K N A K F T I T G I P A L S Y I C I I L R R L E T A E N T K I K F T S G I 664  
c f i m h r y r k n l t a a k k n e l v q k t k s e f n f s s i t y q e f n h y l t s m v g c l w t s k p f g k g - - - - - i y i d p e i l e k t g v a e y k - - - - - n s i n v v h h p s f l s y a v s f l l q e s p - - - - - e e r i v n  
c f i m h r y r k n l t a a k k n e l v q k t k s e f n f s s i t y q e f n h y l t s m v g c l w t s k p f g k g l w t s k p f g k g s i f g v s i y d p e i l e k t g v a e y k f n k n s i n v v h h p s f l s y a v s f l l q e s p a e n t k i e e r t v n  
5.7 9.4 4.8 9.6 6 * 8.6 6.4 5.9 - - - - - 9 * 7.8 8.6 7 * 6 * + 8.7 9.8 7.7 * + 6.9 * 7.8 8.5 5.4 5.7 4.4 4.6 5.8 4.4 8 * * * 6.7 6.9 7.6 6.6 7.9 5.4 6.5 8.9 9.8 4.5 * 8.8 5.6 7.9 9.5 8 * 5.8 5.6 7.4 6.5 6.9 5.7 5.6 8.8 6
```

CENP-I yeast secstruc
CENP-I human secstruc
CENP-I human
CENP-I yeast
consensus
conservation score

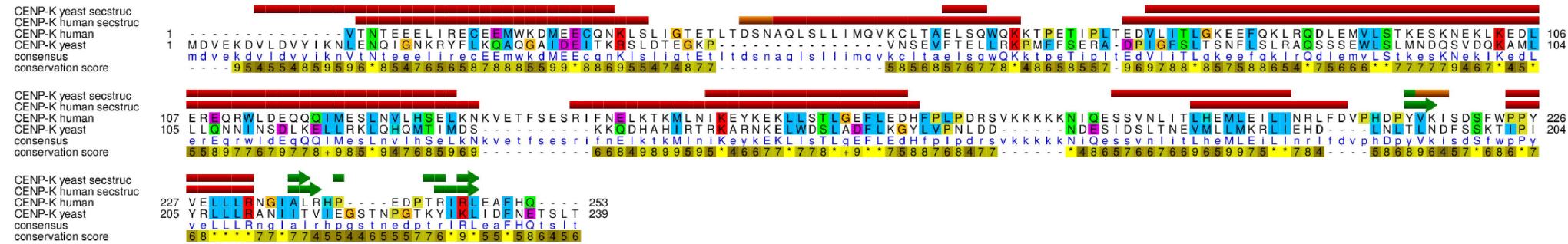
```
658 V S S - - - - - I R G K K W S W Y L D Y L F S Q - - G L Q G I K L F I R S S - - - - - 688  
665 I N E E T F N N F R V H H D E I G Q H G W I K G V N N I H D L R V K I L M H L S N T A N P Y R D I A A P L F I S Y L K S L S K Y S V Q N S 733  
V S s e t f n n f r v h h d e i g q h g w i k g v n n i h d l r v k i l m h l s n t a n p y r d i a a p l f i s y l k s l s k y s v q n s  
9.9 6.6 6.7 5.5 7.7 8.4 + + 5.6 5.4 6 + 4.8 5.9 4.4 5.6 5.4 6.6 6.6 7.7 * 5.8 * 5.9 8.4 5.7 7.8 5.5 + 5.7 * + 5.8 6.5 9.4 5.4 9.8 - - - - -
```

Figure S6 – Related to Figure 1

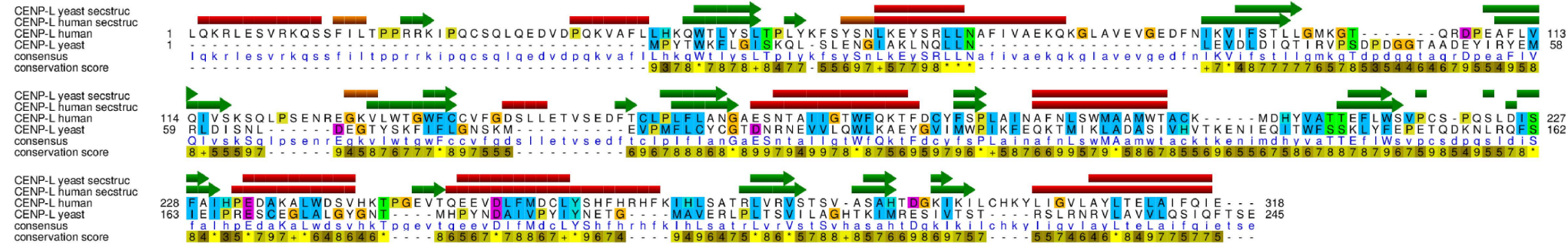
Figure S6 (related to Figure 1). Sequence alignments of human and yeast CENP-H and CENP-I

Secondary structure elements of yeast CCAN (PDB ID 6QLE) were aligned to the human CCAN structure by keeping the molecular shapes and relative orientations as similar as possible. Structure-based alignments were computed by Chimera. The secondary structures for the yeast proteins were assigned by DSSP (Kabsch and Sander, 1983) from the original yeast structures with PDB ID 6QLE and 6WUC. α -helices are shown in red, 3_{10} helices in orange, and β -sheets in green. Sequences are colored according to the ClustalX coloring scheme.

CENP-K



CENP-L



CENP-N

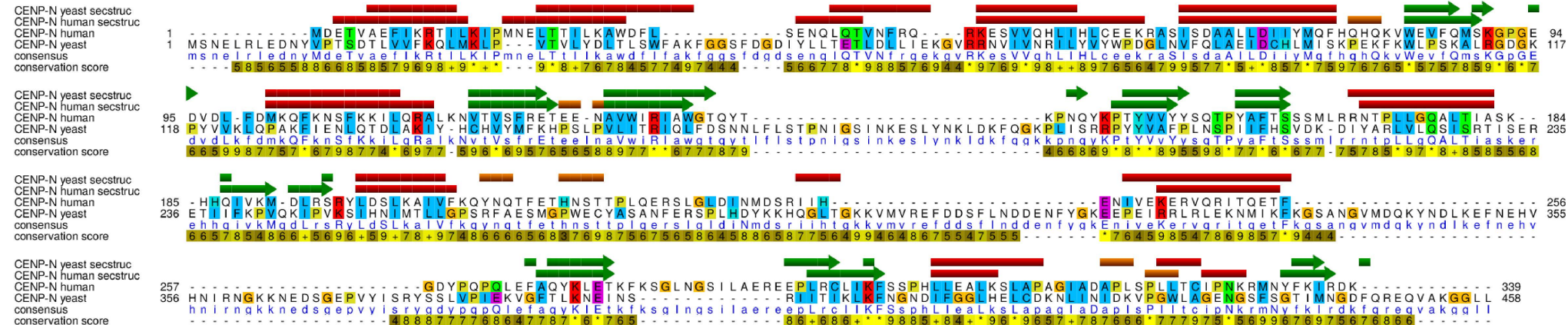
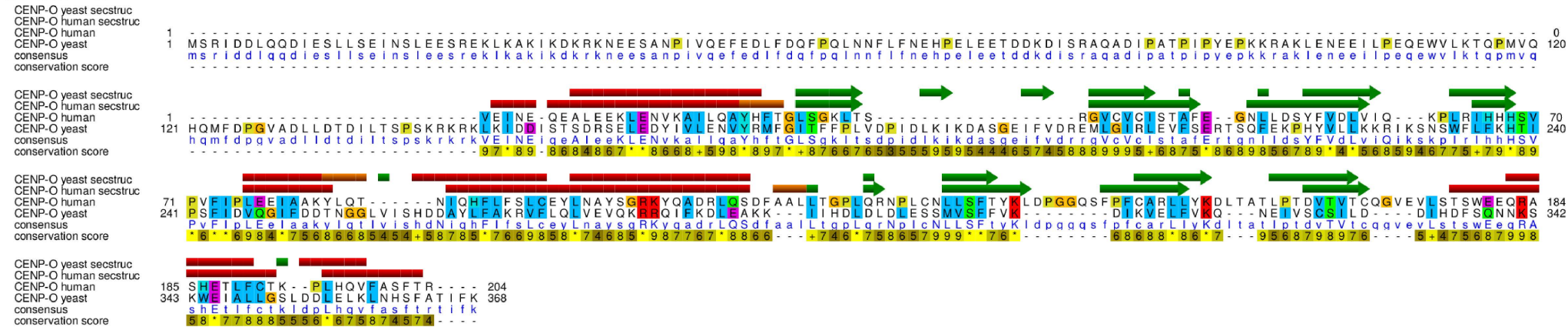


Figure S7 – Related to Figure 1

Figure S7 (related to Figure 1). Sequence alignments of human and yeast CENP-K, CENP-L, and CENP-N

For details, please refer to legend of [Figure S6](#).

CENP-O



CENP-P

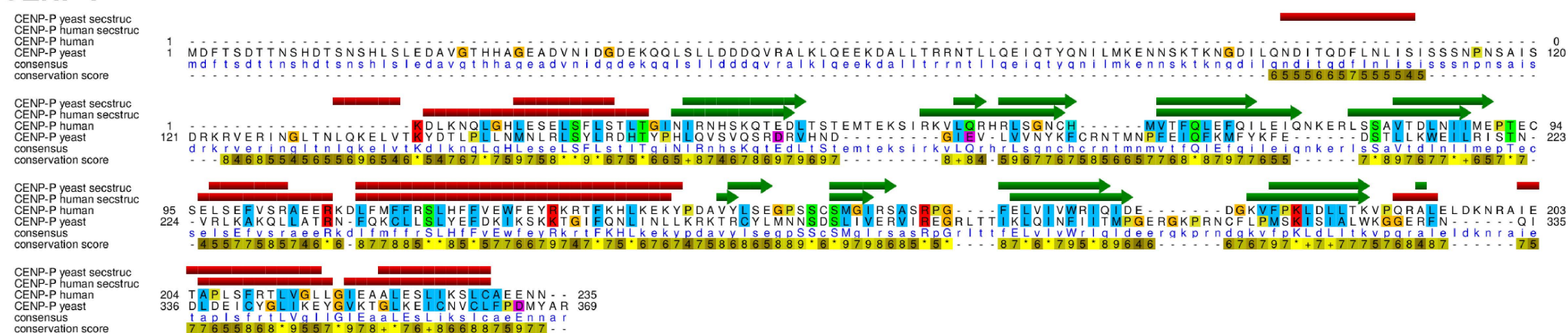
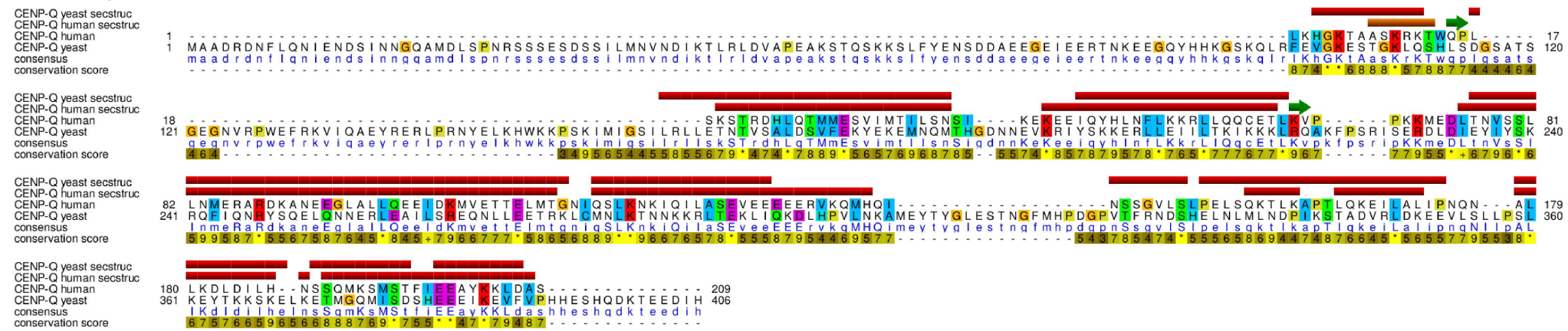


Figure S8 – Related to Figure 1

Figure S8 (related to Figure 1). Sequence alignments of human and yeast CENP-O and CENP-P

For details, please refer to legend of [Figure S6](#).

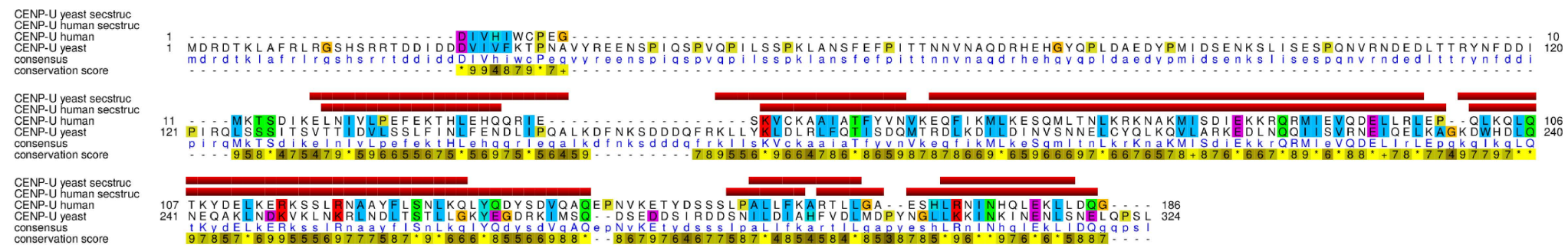
CENP-Q



CENP-T



CENP-U



CENP-W

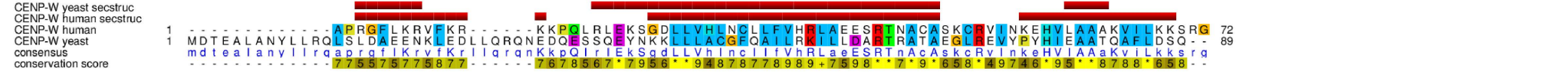


Figure S9 – Related to Figure 1

Figure S9 (related to Figure 1). Sequence alignments of human and yeast CENP-Q, CENP-U, CENP-T, and CENP-W

For details, please refer to legend of [Figure S6](#).

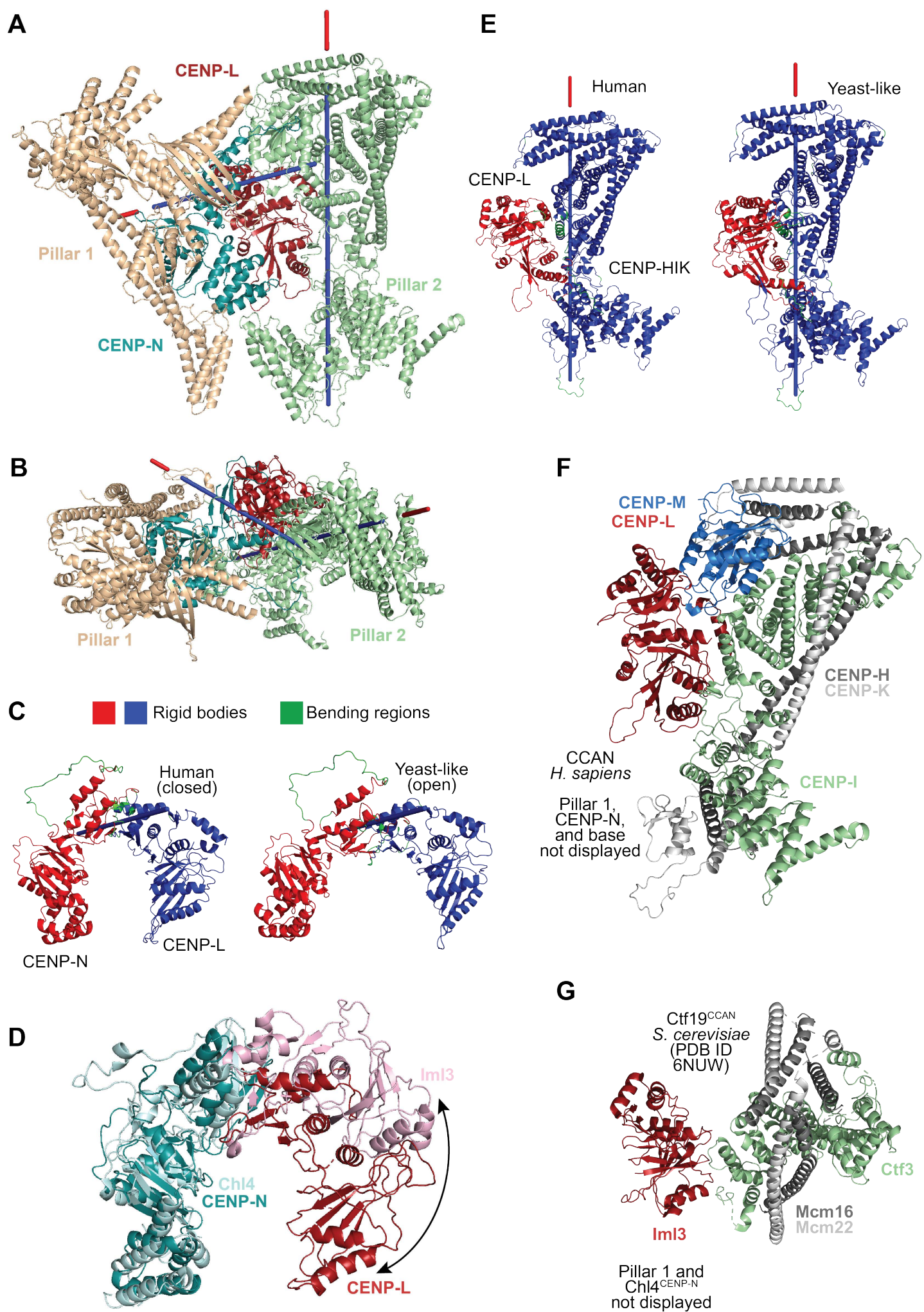


Figure S10 – Related to Figure 1

Figure S10 (related to Figure 1). Structural differences between yeast and human CCAN^{Ctf19}

A-B) The main structural differences between the yeast and human complexes are described by two screw axes, shown from two rotated views $\approx 90^\circ$ apart, as identified by program DynDom6D (Veevers and Hayward, 2019). **C)** Output of DynDom6D for the first main rotation axis, which crosses the CENP-LN dimerization interface. The program's input for comparison were human CCAN subcomplexes and models of the same subcomplexes obtained by optimal subunit superposition on the yeast complex (and therefore identified as "yeast-like"). As shown, the program identifies two rigid bodies (shown in red and blue) in the comparison of open and closed CENP-LN (roughly corresponding to CENP-L and CENP-N). Bending regions are shown in green and cluster at the dimerization interface near the displayed screw axis. The operation is a rotation close to 45° with minimal translation. **D)** Superposition of CENP-N and Chl4 in human CENP-LN (respectively in deepteal and firebrick) and Iml3^{CENP-L}:Chl4^{CENP-N} (respectively in cyan and pink). The curved arrow emphasizes the relative rotation of CENP-L about an axis running through the dimerization domain. **E)** Output of DynDom6D for the second main screw axis, which runs through the interface between CENP-L and CENP-HIK. The two rigid bodies in the comparison correspond to CENP-L and CENP-HIK. The rotation angle is again close to 45° with minimal translation. **F)** Cartoon model of pillar 1 and CENP-L in the vault for human CCAN demonstrates extensive interactions. **G)** The equivalent region in the *S. cerevisiae* complex shows a much more modest interface that is limited to the Iml3^{CENP-L}:Ctf3^{CENP-I} pair, further emphasizing the role of CENP-M as stabilizer of the human complex.

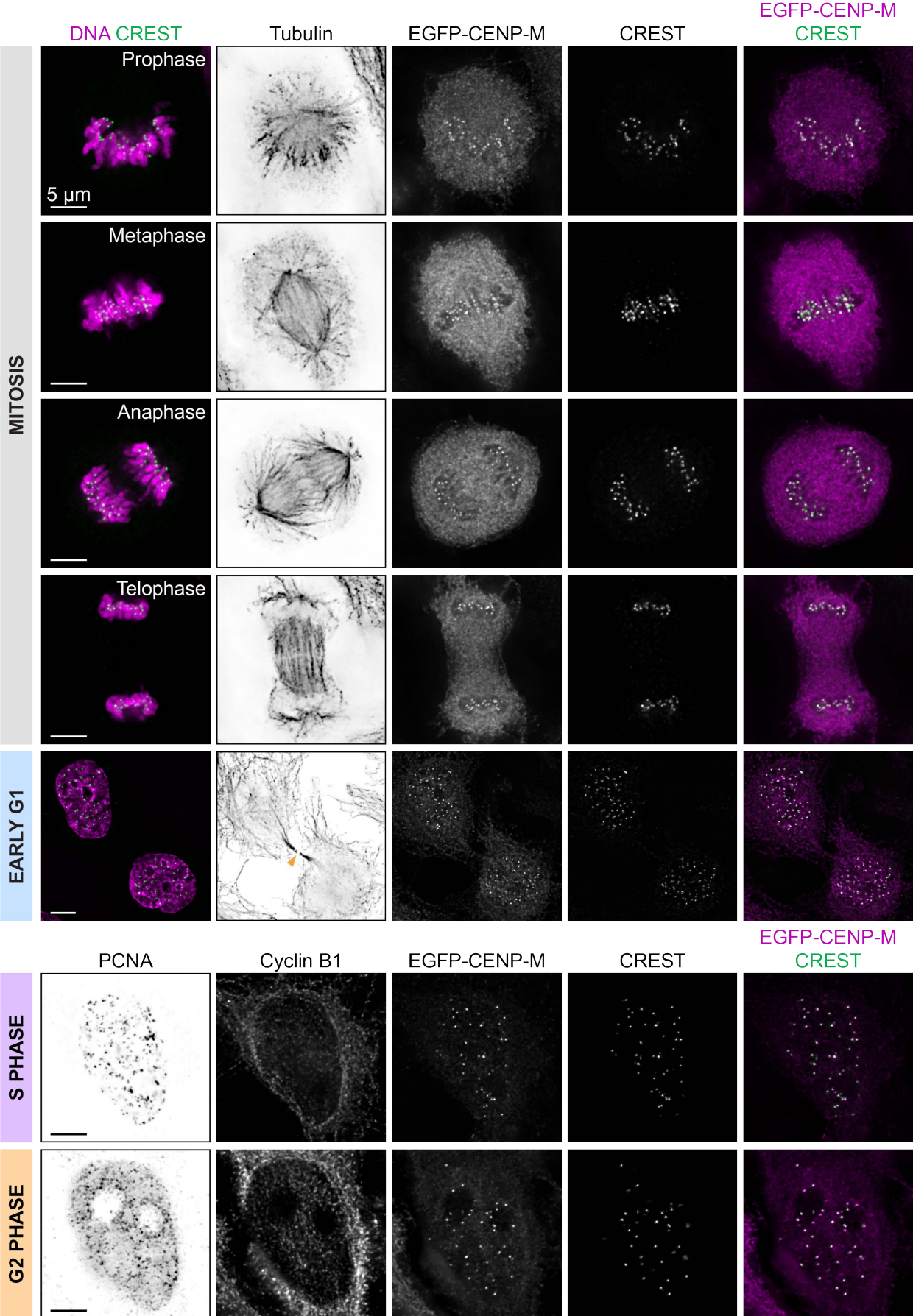


Figure S11 – Related to Figure 2

Figure S11 (related to Figure 2). Gallery of EGFP-CENP-M cell cycle localization

Maximum intensity projections of 5 x 0.2 μm Z-stacks. For Early G1 cells, the orange arrowhead indicates the spindle midbody remnant. Tubulin and DNA were the chosen markers to illustrate mitotic figures. PCNA and cytosolic Cyclin B1 were the chosen markers to illustrate S-phase and G2 phase. The displayed cells are also displayed in [Figure 2H](#). Scale bars = 5 μm .

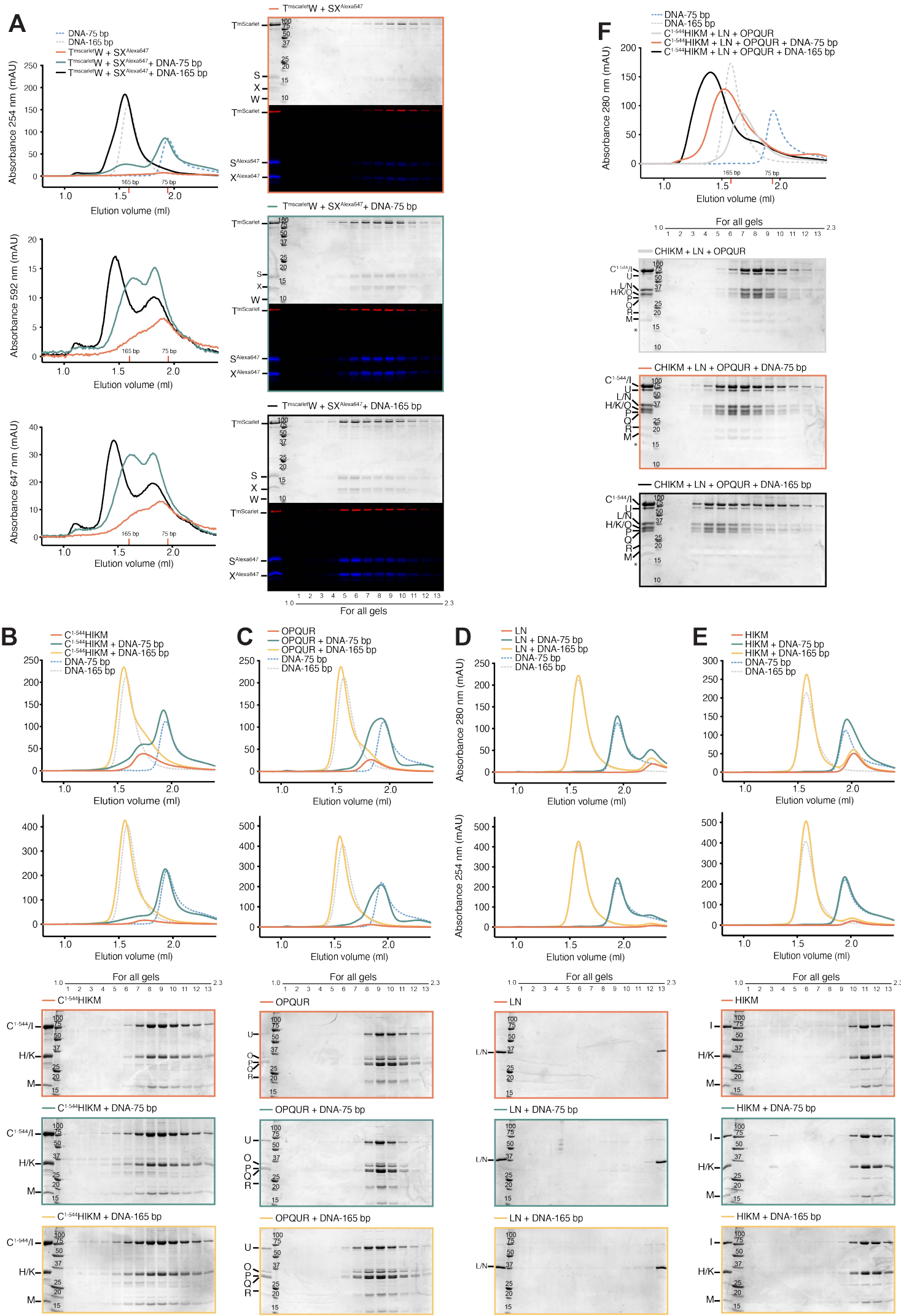


Figure S12 – Related to Figure 3

Figure S12 (related to Figure 3). DNA binding by CCAN subunits

Size-exclusion chromatography on a Superose 6 5/150 column of the indicated samples to monitor protein:DNA binding using 75-bps and 165-bps DNA. **A)** Binding of 75- and 165-bp DNA to fluorescently labelled CENP-TWSX complex. Elution profiles showing absorbance at the indicated wavelengths are shown on the left. Coomassie stained SDS-PAGE of the indicated fractions (100 μ l fractions collected between 1.0 and 2.3 ml) are shown on the right together with fluorescence readout from CENP-T^{tmScarlet} and Alexa647-labelled CENP-SX complex. **B)** Weak CENP-C¹⁻⁵⁴⁴HIKM binding to DNA is demonstrated by a modest left shift upon incubation of protein complex with DNA. The control chromatograms and gels in panels B-D are also shown in [Figure 1A-C](#). **C)** CENP-OPQUR also binds weakly to DNA. **D)** CENP-LN does not bind to DNA. **E)** CENP-HIKM does not bind to DNA. **F)** The combined CCAN subunits in CENP-12 bound DNA with substantial binding affinity.

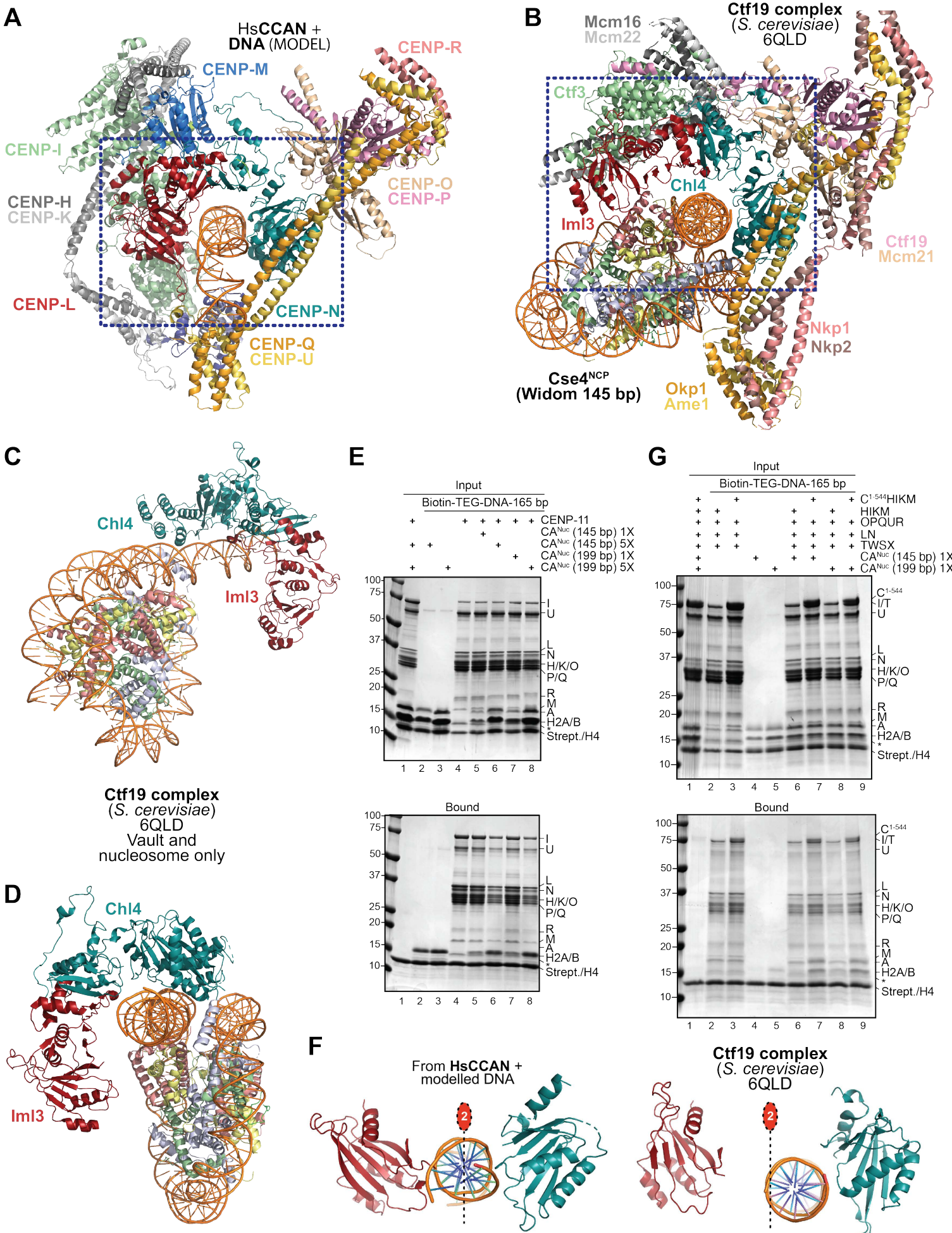
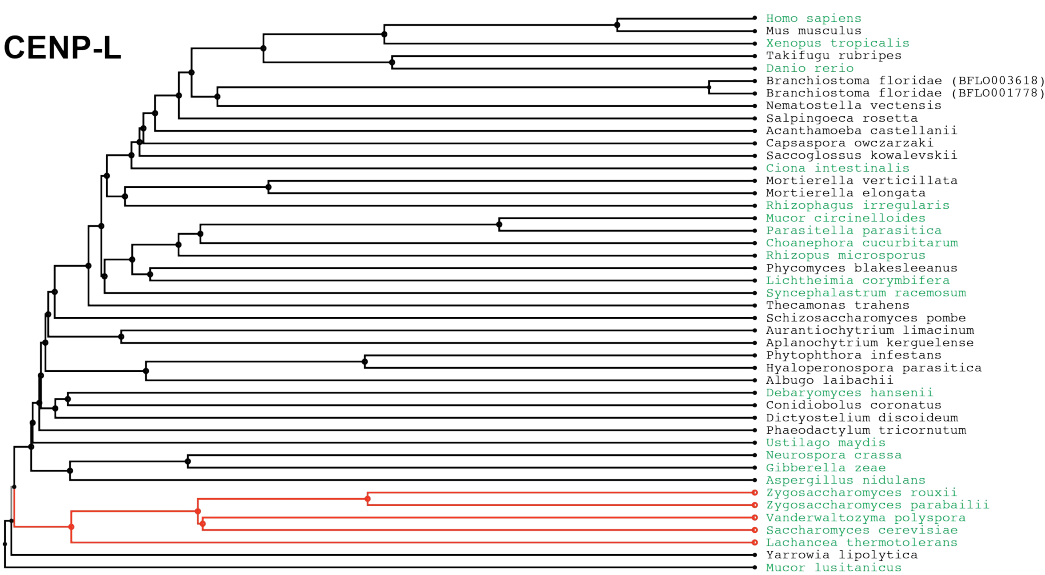
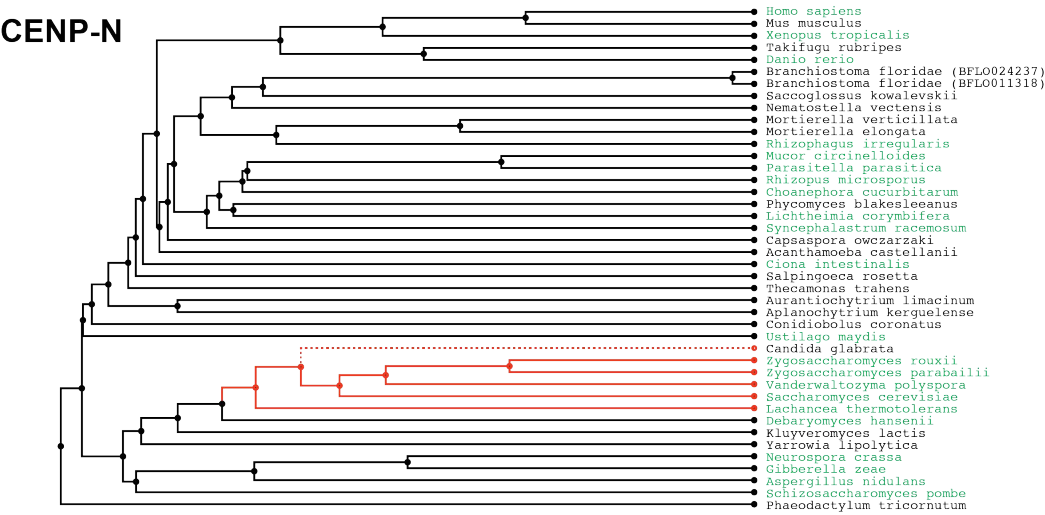


Figure S13 – Related to Figure 4

Figure S13 (related to Figure 4). 2-fold pseudosymmetry and DNA binding mode of the human vault

A) Cartoon model of human CCAN bound to DNA. The DNA fragment was extracted from 6C0W (CENP-N N-terminal region bound to CENP-A nucleosome (Pentakota et al., 2017)) using the DNA gyre facing CENP-N after superposition of CENP-N. **B)** View of the *S. cerevisiae*'s Ctf19^{CCAN}-Cse4^{CENP-A} nucleosome complex (6QLD (Yan et al., 2019)) with the same orientation as the human complex in panel A. **C)** View of 6QLD where only the vault and the nucleosome are displayed. **D)** As in panel C, but from a different orientation to emphasize lack of contacts of Im13^{CENP-L} with the DNA and nucleosome. **E)** Biotin-TEG DNA immobilized on Straptavidin beads was incubated with preys as indicated. Octameric CENP-A nucleosomes created with 145- or 199-bps of DNA did not bind CENP-11 (CENP-HIKM, CENP-LN, CENP-OPQUR), and only caused modest release of the complex when used at 5x concentration. Samples were visualized by SDS-PAGE and Coomassie staining. Three technical repeats were performed. Note that the preparation of nucleosome had an excess of H2A:H2B that bound DNA also in absence of CENP-11. Lack of nucleosome binding is testified by absence of CENP-A in bound fractions. **F)** The 2-fold pseudosymmetry axis linking the two LNHDs of CENP-L and CENP-N and the modelled DNA in human CCAN is offset in the yeast structure (6QLD). The LNHD of Chl4^{CENP-N} is displayed with the same orientation used for the human complex. **G)** Addition of CENP-C¹⁻⁵⁴⁴ to HIKM allows direct comparison of CENP-A nucleosome binding by CENP-15 and CENP-16. CENP-A bound only in presence of CENP-C¹⁻⁵⁴⁴. Three technical repeats were performed.

A**CENP-L****CENP-N****B**

Deep closed vaults

Shallow open vaults

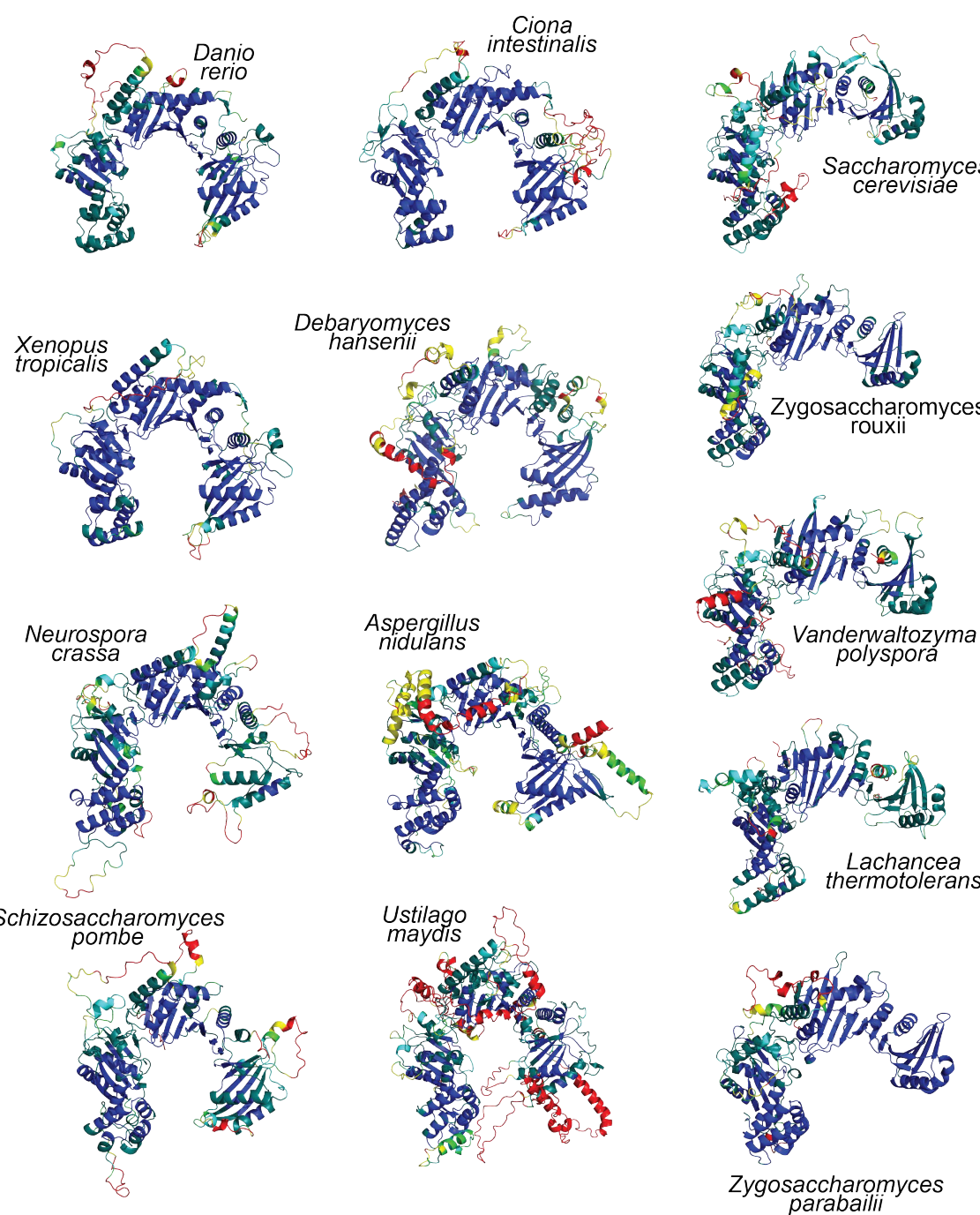


Figure S14 – Related to Figure 5

Figure S14 (related to Figure 5). Phylogenetic analysis of open and closed vaults

A) Cladograms of the indicated CENP-L and CENP-N species were calculated from sequence alignments with <https://mafft.cbrc.jp/alignment/server/phylogeny.html>. Structures of CENP-LN dimers predicted by AF2 are indicated by green species names. The part of the branch indicated with red lines reflects presence of open vaults (either experimentally ascertained, like *Saccharomyces cerevisiae*'s or predicted by AF2. No CENP-L homolog was found in *C. glabrata* (dashed line). **B)** Gallery of a representative subset of AF2 predictions (from those indicated in green in panel A) of vertebrate and yeast CENP-LN orthologs from the indicated species, represented in pLDDT score (blue, high confidence prediction; red, low confidence prediction).

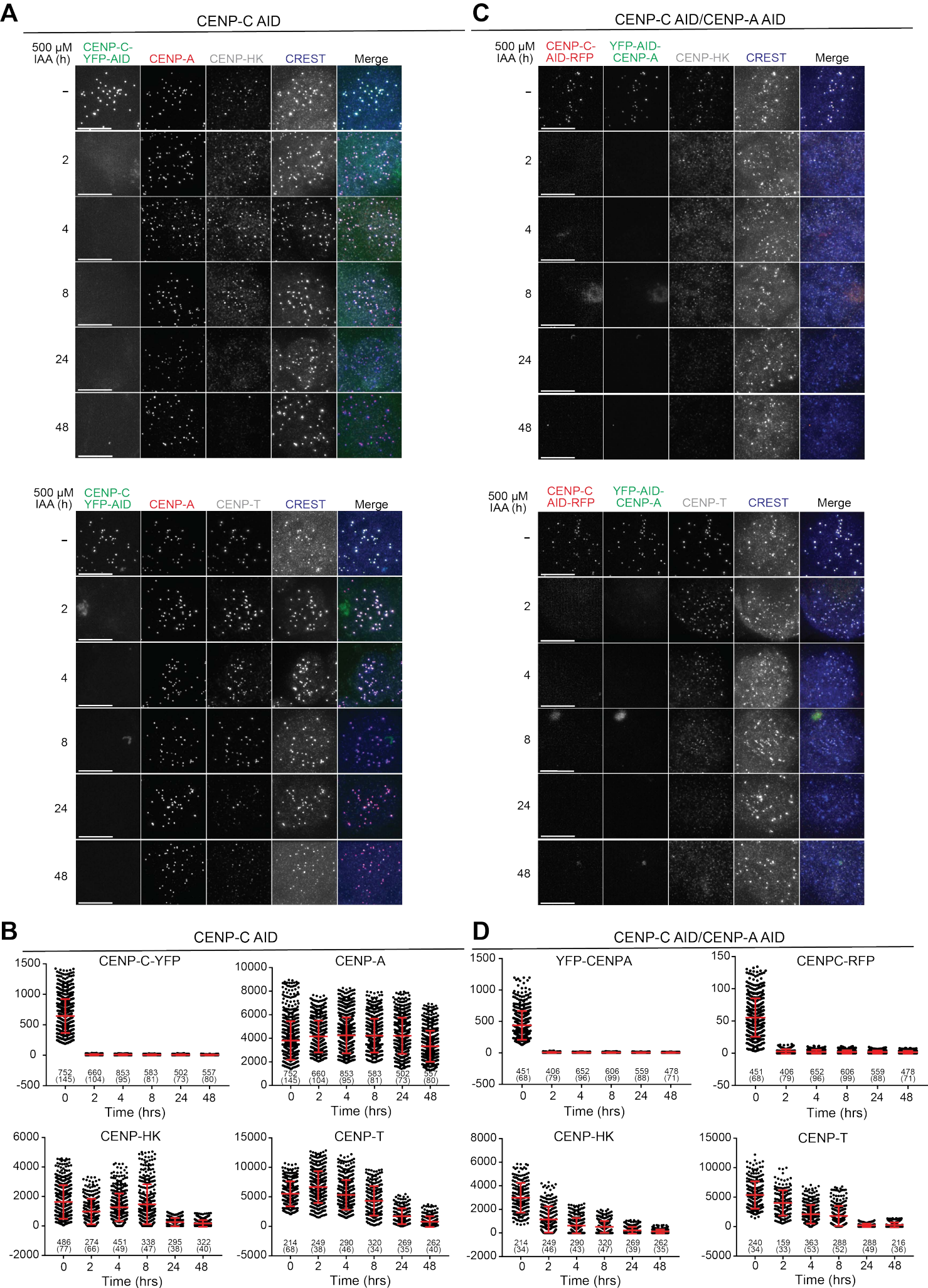


Figure S15 (related to Figure 6). Time course of CENP-C and CENP-A depletion

A) Degradation of CENP-C endogenously tagged with a EYFP-AID cassette (Fachinetti et al., 2015) was induced by addition of indole acetic acid (IAA, Auxin). The full time-course is shown here. Levels of CENP-A, CENP-HK, CENP-T, and CREST were also monitored. Scale bar (here and in panel C) = 10 μm . **B)** Quantification of the experiments in panels A. Number of kinetochores and number of cells (in parentheses) are indicated. Levels of CENP-A and CENP-C^{YFP-AID} from both experiments were quantified together. Levels of CENP-T and CENP-HK were quantified from the individual experiments in panel A. Red bars represent average fluorescence intensities and standard deviation of quantified centromere foci. **C)** Degradation of CENP-A endogenously tagged with a EYFP-AID cassette and of CENP-C endogenously tagged with an RFP-AID cassette (Hoffmann et al., 2020) at the indicated time points after addition of IAA. Levels of CENP-HK, CENP-T, and CREST were also monitored. **D)** Quantification of the experiments in panel C was performed and displayed precisely as described for panel A.